

# Hot –Wire Sensing of Micro-Jet Flow

By

**Yanxia Sun**

**B.S., Precision Instruments and Mechnology**

**Tsinghua University, China, 1999**

**Submitted to the Department of Mechanical Engineering  
in Partial Fulfillment of the Requirement for the Degree of  
Master of Science**

**at the**

**Massachusetts Institute of Technology**


**February 2002**

**© Massachusetts Institute of Technology 2001. All rights reserved.**


Signature of Author.....

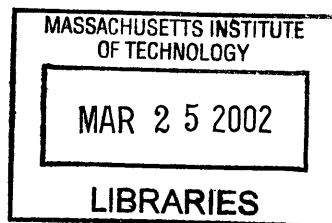
Department of Mechanical Engineering  
June 12,2001

Certified by.....

  
Associate Professor of Mechanical Engineering  
Thesis Supervisor

Accepted by.....

  
Ain A. Sonin  
Professor of Mechanical Engineering  
Chairman, Department Committee on Graduate Students



**BARKER**

# **Hot –Wire Sensing of Micro-Jet Flow**

By

Yanxia Sun

Submitted to the Department of Mechanical Engineering

On January 16, 2001, in partial fulfillment of the

requirements for the Degree of

Master of Science

## **ABSTRACT**

Uniformity of chemical vapor deposition (CVD) depends greatly on gas delivery systems. A typical CVD machine uses metering tubes with a linear array of micro-orifices to deliver gas-phase reactants. This work developed a measurement technique to characterize sub-millimeter scale jet flow produced by a metering tube. It utilizes a hot-wire probe as the sensing element, and the probe is scanned across a flow field narrower than the probe width.

A general heat transfer model was established to describe the probe response to a highly non-uniform jet flow. Both hot-film and hot-wire probes were tested for jet sensing experimentally. Hot-film sensors were found to be more robust and easier to handle. The effect of different sensor operation modes was studied experimentally. Results show that a probe operated under constant current provides a higher sensitivity of detecting small variation of jet velocity than that under constant temperature mode. On the other hand,

constant-temperature probes are more suitable for detecting flow directions. Scanning profiles of micro-jet reveal non-uniform flow distribution along a typical metering tube. Optical imaging of the tube shows that manufacturing defects of the orifices contribute significantly to the non-uniformity of jet flow. This work lays a solid foundation for building flow-testing systems in the semiconductor industry.

Thesis supervisor: Taiqing Qiu

Title: Associate Professor of Mechanical Engineering

# TABLE OF CONTENTS

|  |    |
|--|----|
| ABSTRACT .....   | 2  |
| TABLE OF CONTENTS .....                                      | 4  |
| LIST OF FIGURES.....   | 6  |
| LIST OF TABLES .....   | 10 |
| CHAPTER 1 INTRODUCTION .....                                 | 11 |
| CHAPTER 2 NUMERICAL SIMULATION OF JET FLOW .....             | 14 |
| 2.1 Exit jet velocity .....                                  | 15 |
| 2.2 Laminar jet flow .....                                   | 17 |
| 2.3 Incompressible turbulent jet flow.....                   | 21 |
| CHAPTER 3 HOT-WIRE SENSING OF MICOR-JET .....                | 25 |
| 3.1 Introduction .....                                       | 25 |
| 3.2 Structure of hot-wire probes.....                        | 26 |
| 3.3 Heat transfer model .....                                | 28 |
| 3.4 Results and discussion.....                              | 34 |
| 3.4.1 Hot-wire sensing in still air .....                    | 34 |
| 3.4.2 Hot-wire sensing in uniform flow .....                 | 37 |
| 3.4.3 Hot-wire sensing profiles for micro-jet flow.....      | 40 |
| Chapter 4 EXPERIMENTAL SETUP .....                           | 46 |
| 4.1 Air supply.....  | 46 |
| 4-2 Hot-wire probes and signal conditioning.....             | 47 |
| 4.3 Probe scanning system .....                              | 50 |
| Chapter 5 HOT-WIRE SCANNING OF MICRO-JETS .....              | 53 |
| 5.1 Effect of sensor types sensing results.....              | 53 |
| 5.2 Sensitivity to axial position .....                      | 55 |
| 5.3 Sensitivity to backpressure.....                         | 57 |
| 5.4 Reliability of hot-wire sensing for micro-jet flow ..... | 59 |
| 5.5 Jet direction .....                                      | 61 |



|  |    |
|--|----|
| 5.6 Sensing profiles at different backpressures..... | 64 |
| 5.7 Uniformity of micro-jets .....                   | 70 |
| <br>   |    |
| Chapter 6 CONCLUSION AND FURTHER WORK .....          | 85 |
| REFECENCES.....                                      | 87 |

## LIST OF FIGURES

|  |    |
|--|----|
| Figure 1-1. Schematic diagram of CVD deposition.....   | 12 |
| Figure 1-2. Schematic diagram of flow metering tube.....                                       | 12 |
| Figure 2-1. Schematic diagram of gas flow in a metering tube .....                             | 14 |
| Figure 2-2. Enlarged view of flow near an orifice .....  | 15 |
| Figure 2-3. Exit jet velocity.....   | 17 |
| Figure 2-4. Jet flow from an orifice .....   | 18 |
| Figure 2-5. Axial velocity profile for laminar flow ( $z=3\text{mm}$ ) .....                   | 20 |
| Figure 2-6. Radial velocity profile for laminar flow ( $z=3\text{mm}$ ).....                   | 20 |
| Figure 2-7. Axial velocity profile for turbulent flow ( $z=1.0\text{mm}$ ) .....               | 23 |
| Figure 2-8. Radial velocity profile for turbulent flow ( $z=1.0\text{mm}$ ).....               | 23 |
| Figure 2-9. Axial velocity profile for turbulent flow ( $z=2.5\text{mm}$ ) .....               | 24 |
| Figure 2-10. Radial velocity profile for turbulent flow ( $z=2.5\text{mm}$ ).....              | 24 |
| Figure 3-1. Hot-wire operation.....  | 25 |
| Figure 3-2. Optical images of hot-wire and hot-film probes.....                                | 26 |
| Figure 3-3. Structure of hot-wire and hot-film probes .....                                    | 27 |
| Figure 3-4. Schematic model of hot-wire and hot-film probes .....                              | 29 |
| Figure 3-5. The heat transfer model for wire support .....                                     | 32 |
| Figure 3-6. The temperature distribution along the wire (TSI1210-60, CC, $I=100\text{ mA}$ ) . | 35 |
| Figure 3-7. Electrical resistance of hot-film probe in still air .....                         | 36 |
| Figure 3-8. Average wire temperature in still air .....  | 37 |
| Figure 3-9. Effect of convection on wire temperature ( $I=100\text{mA}$ ) .....                | 39 |

|   |    |
|---|----|
| Figure 3-10. Correlation of probe resistance ( $I=100\text{mA}$ ) .....                 | 40 |
| Figure 3-11. Horizontal wire in mixed convection and conduction.....                    | 41 |
| Figure 3-12. Temperature distribution along the wire when HFA sits at the jet's center. | 42 |
| Figure 3-13. Probe temperature during scanning ( $I=100\text{mA}$ ).....                | 43 |
| Figure 3-14. Effect of jet velocity on scanning profiles.....                           | 44 |
| Figure 3-15. Effect of axial position on scanning profiles.....                         | 45 |
| Figure 4-1. Schematic diagram of air supply system .....                                | 46 |
| Figure 4-2. Calibration of pressure transducer.....                                     | 47 |
| Figure 4-3. Schematic diagram of TSI1210 general purpose probe (-T1.5, -20, -60) .....  | 48 |
| Figure 4-4. Constant-current circuit.....   | 49 |
| Figure 4-5. Constant-temperature circuit .....  | 50 |
| Figure 4-6. Experimental setup .....  | 51 |
| Figure 5-1. Hot-wire probe sensing of micro-jet flow .....                              | 54 |
| Figure 5-2. Hot-film probe sensing of micro-jet flow.....                               | 55 |
| Figure 5-3. Scanning along jet centerline.....  | 56 |
| Figure 5-4. Hot-film sensing of micro-jet flow near orifice .....                       | 57 |
| Figure 5-5. Hot-film scanning of orifice #23 .....                                      | 58 |
| Figure 5-6. Hot-film scanning of orifice #24 .....                                      | 59 |
| Figure 5-7. Optical image of orifice #35.....   | 60 |
| Figure 5-8. Repeatability of hot-wire scanning.....                                     | 60 |
| Figure 5-9. Hot-film profiling of jet at relatively low velocity.....                   | 62 |
| Figure 5-10. Hot-film profiling of jet at relatively high velocity.....                 | 63 |
| Figure 5-11. Hot-film profiling of jet at relatively high velocity (CC mode).....       | 64 |

|   |    |
|---|----|
| Figure 5-12. Three working backpressures when four orifices open..... | 65 |
| Figure 5-13. Scanning profiles of jet #22 (CC mode).....              | 66 |
| Figure 5-14. Scanning profiles of jet #23 (CC mode).....              | 66 |
| Figure 5-15. Scanning profiles of jet #24 (CC mode).....              | 67 |
| Figure 5-16. Scanning profiles of jet #25 (CC mode).....              | 67 |
| Figure 5-17. Scanning profiles of jet #22 (CT mode).....              | 68 |
| Figure 5-18. Scanning profiles of jet #23 (CT mode).....              | 69 |
| Figure 5-19. Scanning profiles of jet #24 (CT mode).....              | 69 |
| Figure 5-20. Scanning profiles of jet #25 (CT mode).....              | 70 |
| Figure 5-21. Scanning profiles of four orifices.....                  | 71 |
| Figure 5-22. Optical images for four neighboring orifices.....        | 72 |
| Figure 5-23. Scanning profiles at low backpressure (CC mode).....     | 73 |
| Figure 5-24. Scanning profiles at medium backpressure (CC mode).....  | 73 |
| Figure 5-25. Scanning profiles at high backpressure (CC mode).....    | 74 |
| Figure 5-26. Scanning profiles at low backpressure (CT mode).....     | 74 |
| Figure 5-27. Scanning profiles at medium backpressure (CT mode).....  | 75 |
| Figure 5-28. Scanning profiles at high backpressure (CT mode).....    | 75 |
| Figure 5-29. Scanning profiles of jet #22.....                        | 76 |
| Figure 5-30. Scanning profiles of jet #23.....                        | 77 |
| Figure 5-31. Scanning profiles of jet #24.....                        | 78 |
| Figure 5-32. Scanning profiles of jet #25.....                        | 79 |
| Figure5-33. Scanning profiles along the metering tube.....            | 81 |
| Figure5-34. Scanning profiles of jets near metering tube inlet.....   | 82 |

Figure5-35. Scanning profiles of jets near the dead end of metering tube..... 83  
Figure5-36. Optical images of orifice #3 and #35 ..... 84

# LIST OF TABLES

Table 3-1. Dimensions of hot-wire probes..... 28

Table 3-2. Physical properties used in simulations ..... 33

Table 4-1. Characteristics of TSI hot-wire probes ..... 48

# CHAPTER 1 INTRODUCTION

Chemical vapor deposition (CVD) of thin films is widely used in the semiconductor industry to produce integrated circuits, liquid-crystal displays and solar cells. Figure 1-1 shows a schematic diagram of a typical CVD deposition process (Dobkin et al., 1995). Gas-phase reactants are first introduced into an injector head through separate metering tubes and then directed into a straight channel. As the reactants leave the channel, they form a sheet of one-dimensional jet, impinging on a heated silicon wafer. As the chemicals approach the wafer, the gas temperature increases, initiating chemical reactions and thin-film deposition. The depleted reactants are pumped away from the wafer through the exhaust channels of the injector.

The uniformity of CVD deposited films depends greatly on the uniformity of flow along the long and narrow sheet of jet exiting the injector head. As the wafer diameter increases from 200mm to 300 mm, the requirement for flow uniformity is significantly increased.

Metering tubes play an important role in controlling flow uniformity. A typical metering tube consists of a lineal array of 30 to 50 sub-millimeter orifices. Figure 1-2 is a schematic diagram of a metering tube. There exit two fundamental factors affecting flow uniformity: manufacturing defects and fluid mechanics. The fine orifices on a metering tube are typically produced through electrical-discharge machining (EDM). During EDM the fine discharge wire wears and deforms, resulting in variations in orifice diameters and

pointing directions. Furthermore, the molten metal may not be removed completely during EDM, forming solid debris around the orifices.

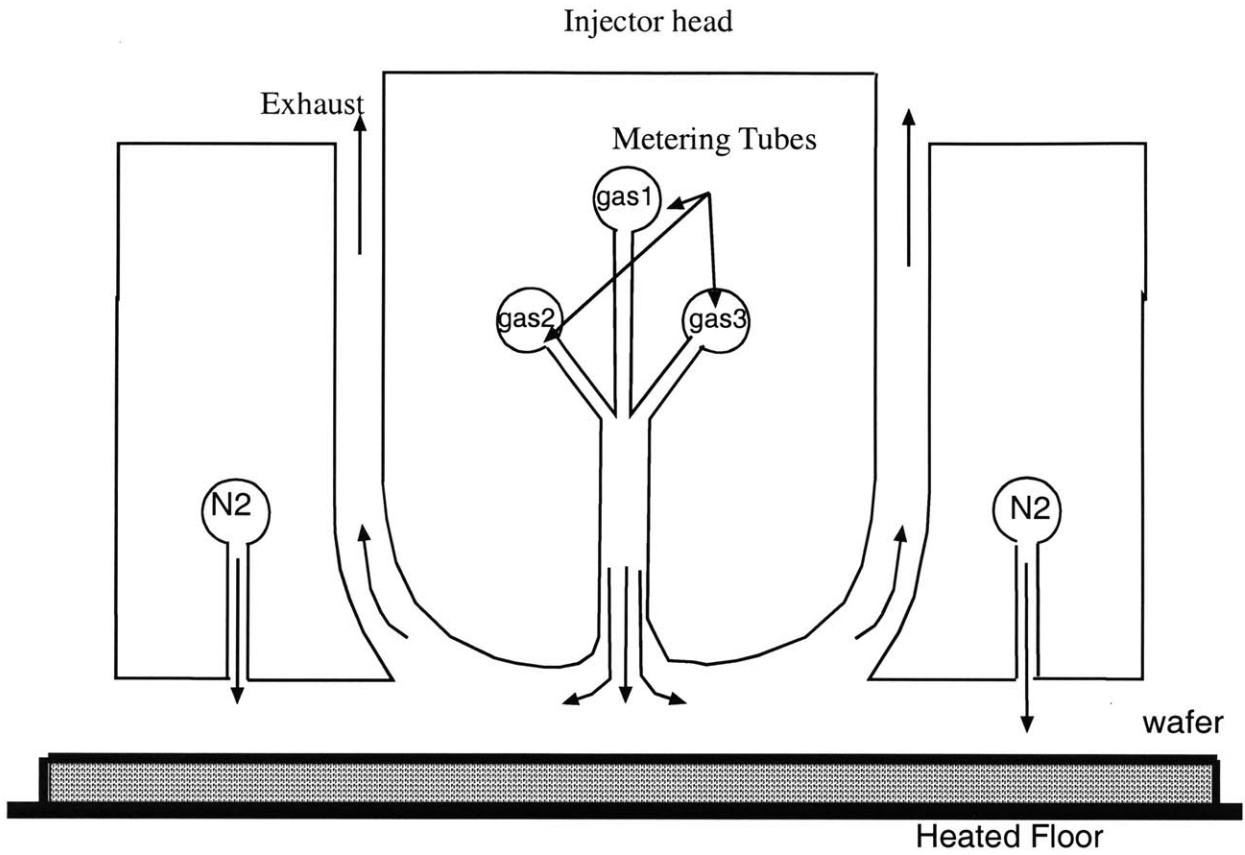


Figure 1-1. Schematic diagram of CVD deposition

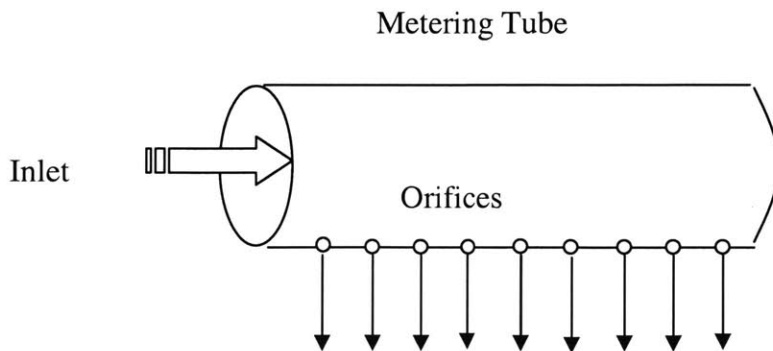


Figure 1-2. Schematic diagram of flow metering tube



The second factor causing flow non-uniformity is due to two competing physical processes. As chemicals flow within a metering tube, friction at the wall results in a gradual decrease of the gas pressure. On the other hand, as the gases exit the tube through the orifices, the mean velocity of the gases drops along the tube, which in turn leads to an increase of gas pressure. Numerical simulations show that these two competing processes produce a non-uniform pressure distribution and thus a non-uniform jet velocity distribution along the tube (Mokhtari et al., 1997). They found that this intrinsic flow distribution depends significantly on the orifice diameter and total inflow rate.

The objective of this work is to develop a sensing technique capable of measuring both the magnitude and direction of sub-millimeter jet flows. It will provide a better understanding of jet flows from a linear metering tube. It will also be used in the semiconductor industry for quantitative evaluation of metering tubes.

A hot-wire probe is used in this work as the sensing element. Chapter 2 simulates velocity distributions of ideal laminar and turbulent jets. Since the characteristic jet width is much smaller than the sensing length of a typical hot-wire probe, chapter 3 develops a heat transfer model to describe responses of hot-wire probes in a highly non-uniform jet flow. It establishes the physical foundation for this unique hot-wire sensing technique. Chapter 4 describes details of the experimental system, and chapter 5 presents the experimental data and discusses the results. This work is summarized in chapter 6.

## CHAPTER 2 NUMERICAL SIMULATION OF JET FLOW

Figure 2-1 shows a schematic diagram of gas flow in a metering tube. For typical CVD applications, the flow is laminar, single-phase and non-reacting within the tube. The tube temperature is about  $20^{\circ}\text{C}$  higher than the inlet gas temperature, which is around  $22^{\circ}\text{C}$ . The inlet gauge pressure,  $P$ , controls the total flow rate through the tube. The objective of this chapter is to estimate the exit jet velocity and velocity distribution of the jets. The numerical simulations are conducted under the following assumptions.

1. Both the pressure variation and slight heating along the metering tube are neglected.
2. The orifice diameter is  $0.2\text{ mm}$ , and the orifices are circular and smooth. The inside diameter of the tube is  $5.10\text{ mm}$  and the wall thickness is  $0.28\text{ mm}$ .

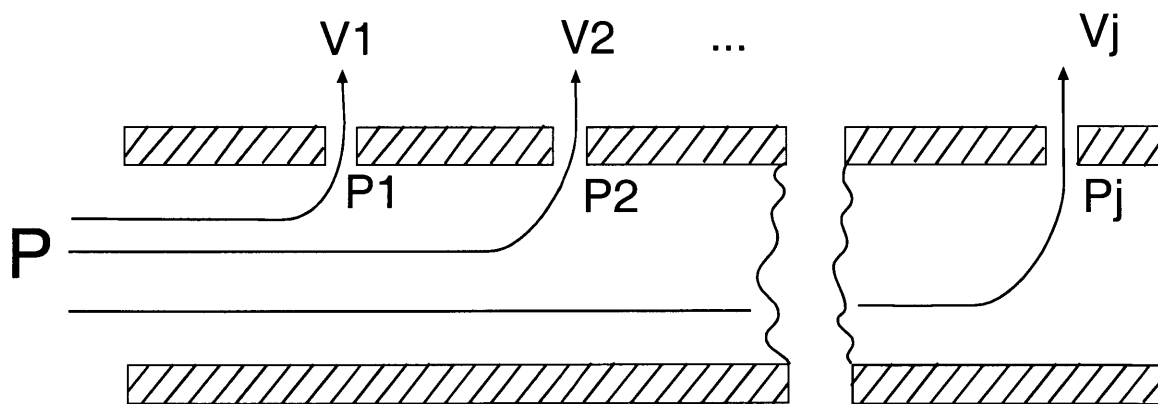


Figure 2-1. Schematic diagram of gas flow in a metering tube

## 2.1 Exit jet velocity

This section estimates the exit velocity of jets. Applying the Bernolli's equation along a streamline (figure 2-2), the exit jet velocity,  $V_e$ , is related to the inlet gas pressure,  $P$ , as

$$P + \frac{1}{2}\rho V_1^2 = \frac{1}{2}\rho V_e^2 + \Delta P_0 + \Delta P_1 + \Delta P_2 + \Delta P_3 \quad (2.1)$$

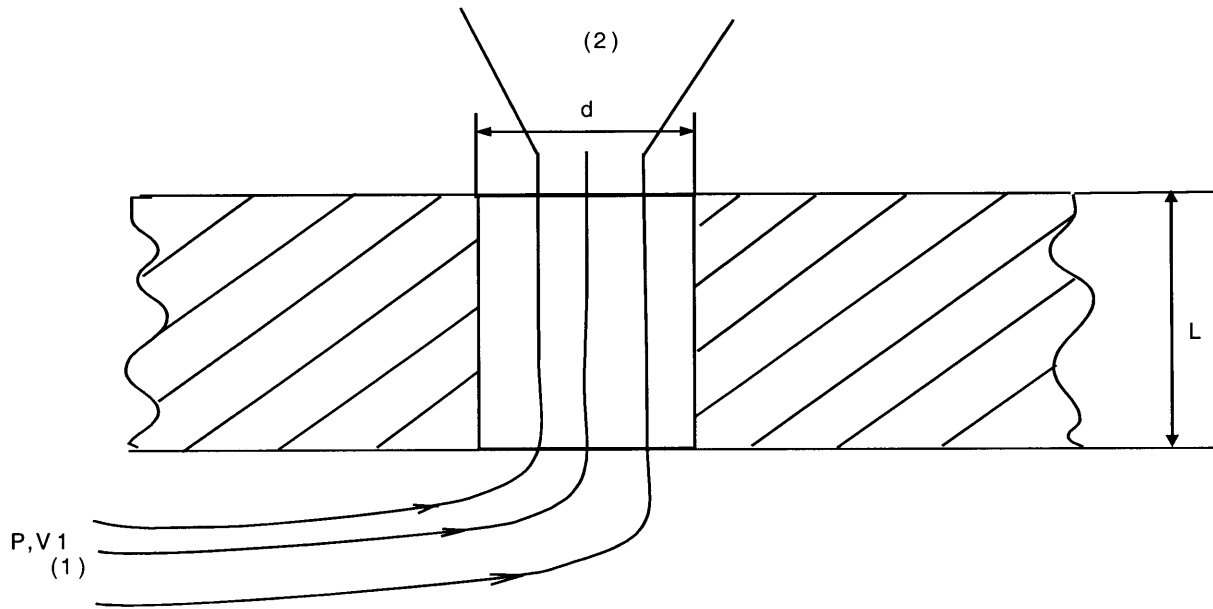


Figure 2-2. Enlarged view of flow near an orifice

where  $V_1$  is the inlet gas velocity. The pressure change along the tube,  $\Delta P_0$ , is

$$\Delta P_0 = \frac{1}{2}\rho K_0 V_e^2 \quad (2.2)$$

where the pressure coefficient,  $K_0$  can be positive or negative (Mokhtari, et al., 19997).

The pressure loss near the orifice entrance,  $\Delta P_1$ , is

$$\Delta P_1 = \frac{1}{2}\rho K_1 V_e^2 \quad (2.3)$$

where the loss coefficient due to sudden contraction is  $K_1=0.42$  (White, 1994). Since the wall thickness of the metering tube,  $L$ , is larger than the orifice diameter,  $d$ , pressure loss due to friction at the orifice wall,  $\Delta P_2$ , is

$$\Delta P_2 = \frac{1}{2} f \frac{L}{d} \rho V_e^2 = \frac{1}{2} \rho K_2 V_e^2 \quad (2.4)$$

At a typical Reynolds number of  $Re=1000$ , the friction coefficient,  $f$ , is 0.064. The pressure loss at the orifice exit,  $\Delta P_3$ , is

$$\Delta P_3 = \frac{1}{2} \rho K_3 V_e^2 \quad (2.5)$$

The value of  $K_3 = 1$  for sudden expansion is used here. Since the exit jet velocity,  $V_e$ , is much larger than the inlet gas velocity  $V_1$ , jet velocity can be found from equation 2.1 as

$$V_e = \sqrt{\frac{2P}{\rho(1 + K_0 + K_1 + K_2 + K_3)}} = \sqrt{\frac{2P}{\rho K}} \quad (2.6)$$

Figure 2-3 presents jet velocity as a function of the inlet pressure at different value of total pressure loss coefficient,  $K$ .

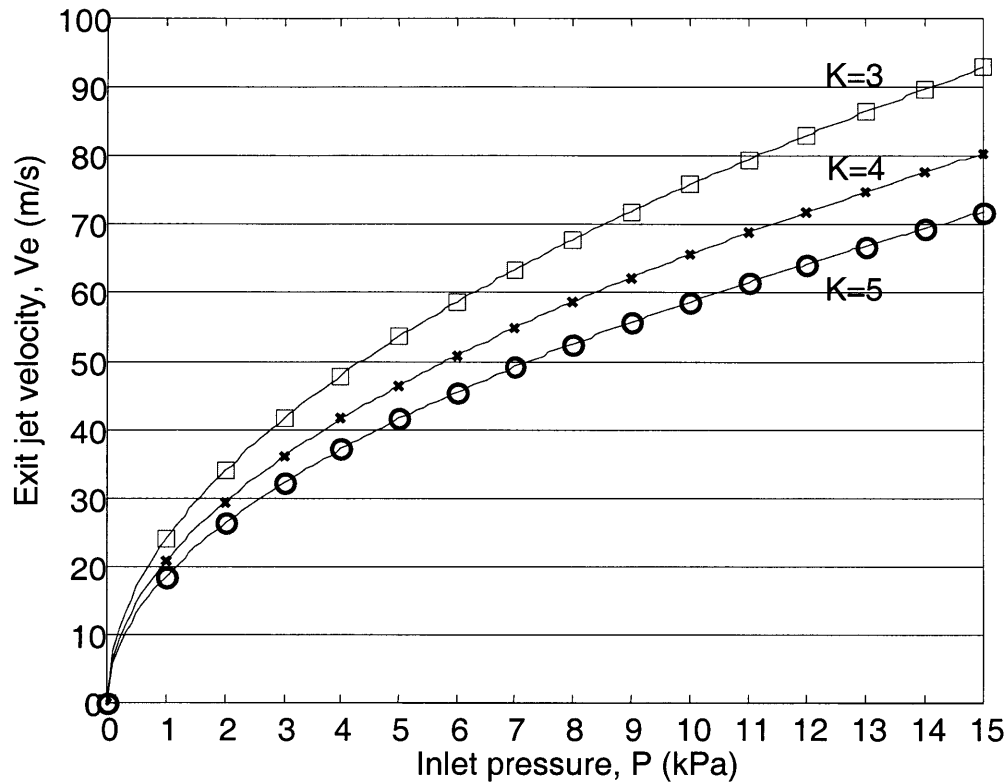


Figure 2-3. Exit jet velocity

## 2.2 Laminar jet flow

Figure 2-4 illustrates the essential features of a jet issued from an orifice into still air. The velocity profile is assumed to be uniform at the orifice exit here. There exists a region called the potential core of the jet ( $0 \leq z < Z_c$ ). Within the potential core, the jet velocity is not affected. Outside this region, significant fluid mixing exists, resulting a monotonic decrease of the jet velocity.

The potential region is generally within 5-7 orifice diameters. Beyond the potential core ( $Z > Z_c$ ), the effects of viscous shear are active across the whole width of the jet, and the jet flow becomes self-similar.

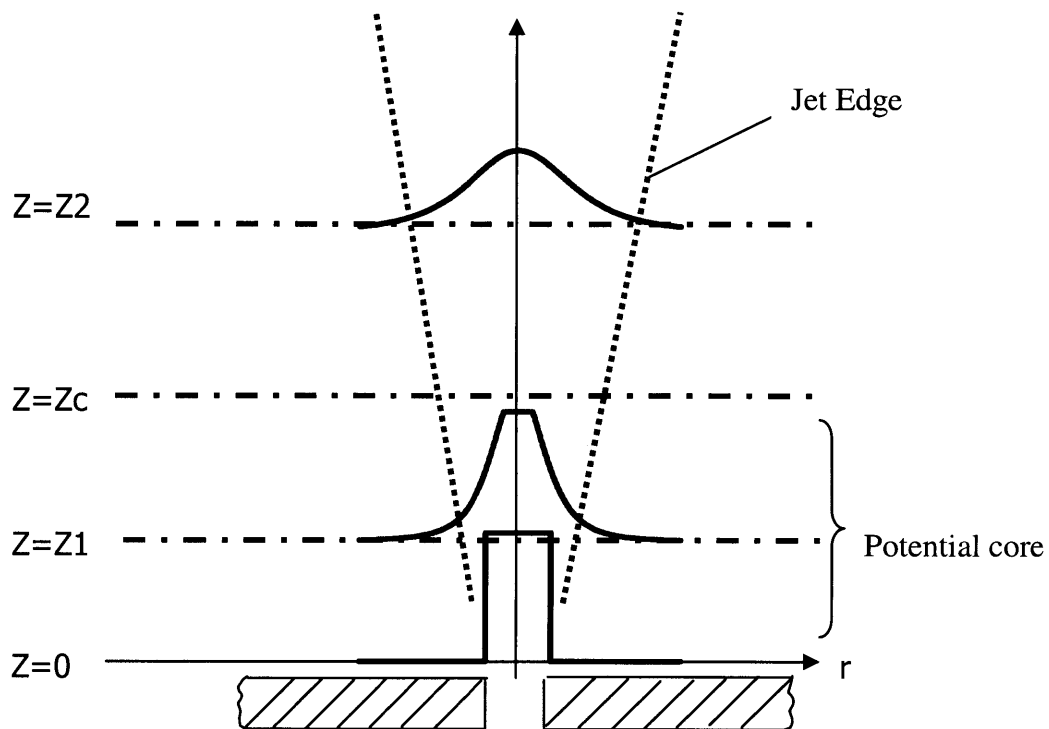


Figure 2-4. Jet flow from an orifice

Jet flow can be characterized by the Reynolds number based on the exit velocity,  $V_e$ , and the orifice diameter,  $d$ ,

$$\text{Re} = \frac{dV_e}{\nu} \quad (2.7)$$

At a small Reynolds number, e.g.,  $\text{Re} < 30$ , the jet flow is laminar. Far away from the orifice, the axial velocity,  $V_z$  and radial velocity  $V_r$ , have been reported in the literature (Schlichting, 1979; Turns, 2000),

$$V_z = \frac{V_c}{[1 + \eta^2]^2} \quad (2.8)$$

$$V_r = \frac{8V_c}{\sqrt{3} \text{Re}} \frac{\eta(1 - \eta^2)}{(1 + \eta^2)^2} \quad (2.9)$$

where  $V_c$  is the axial velocity at the jet center,

$$V_c = \frac{3}{32} \text{Re} \frac{d}{z} V_e \quad (2.10)$$

the similarity parameter,  $\eta$ , is

$$\eta = \frac{\sqrt{3}}{16} \text{Re} \frac{r}{z} \quad (2.11)$$

and  $z$  and  $r$  are the axial and radial positions measured from the orifice, respectively.

The radial position at which the axial velocity is half of the center velocity is

$$r_{0.5} = \frac{1.49}{\text{Re}} \times z \quad (2.12)$$

the jet width at half center velocity is

$$d_{0.5} = \frac{2.98}{\text{Re}} \times z \quad (2.13)$$

It increases with the axial position and decreases with the increase of the Reynolds number.

Figures 2-5 and 2-6 present simulated velocity profiles at  $z=3\text{mm}$  at different exit jet velocities. The results show that the radial jet velocity is significantly smaller than the axial velocity.

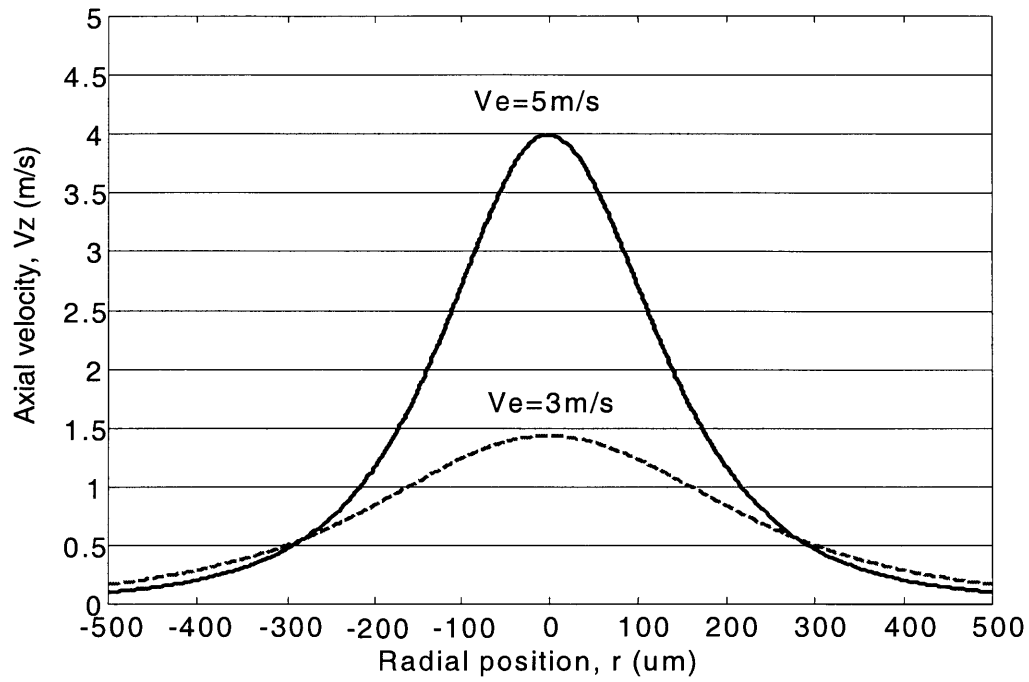


Figure 2-5. Axial velocity profile for laminar flow ( $z=3\text{mm}$ )

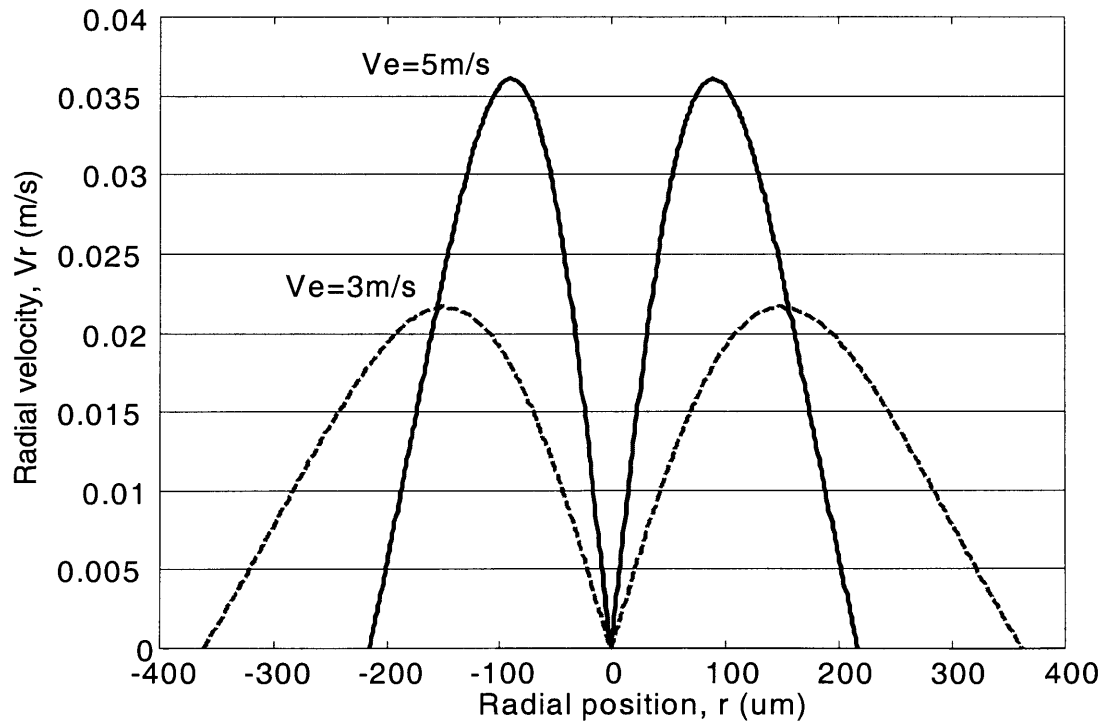


Figure 2-6. Radial velocity profile for laminar flow ( $z=3\text{mm}$ )



### 2.3 Incompressible turbulent jet flow

At relatively high Reynolds number, jet becomes turbulent. Turbulence greatly enhances fluid mixing, which in turn increases internal friction of fluid. This effect can be modeled by replacing the kinetics viscosity  $\nu$  in laminar flow case by eddy viscosity  $\varepsilon$  (Schlichting, 1979),

$$\varepsilon = 0.0143 \text{Re } \nu \quad (2.14)$$

Far away from the orifice and assuming that the jet momentum is conserved, the similarity solution of jet velocity are given by Schlichting (1979),

$$V_z = \frac{V_c}{[1 + \eta^2]^2} \quad (2.15)$$

$$V_r = \frac{8V_c}{\sqrt{3} \text{Re}} \frac{\eta(1 - \eta^2)}{(1 + \eta^2)^2} \quad (2.16)$$

$$V_c = \frac{6.6dVe}{z} \quad (2.17)$$

where the similarity parameter,  $\eta$ , is

$$\eta = 7.59 \frac{r}{z} \quad (2.18)$$

Figures 2-7 to 2-10 present velocity profiles at locations  $z=1\text{mm}$  and  $z=2.5\text{mm}$ . The radial velocity is found to be less than 2% of the axial velocity.

The location at which the axial velocity is half of the center velocity is

$$\eta_{0.5}=0.64 \quad \text{or} \quad r_{0.5} = 0.084z . \quad (2.19)$$

The full width of the jet at half center velocity is

$$d_{0.5} = 0.17z \quad (2.20)$$

The jet width is independent of the Reynolds number. The center jet velocity decreases with  $z$ . It drops to half of the exit jet velocity at location  $z_{0.5}$ ,

$$z_{0.5} = 13.2d \quad (2.21)$$

For the orifice used in this work,  $d=0.2\text{mm}$ ,  $z_{0.5}$  is 2.6mm. The width of the jet at this location is about 0.5mm. The results suggest that sensing of the jet flow should be conducted within a few millimeters of the orifice, and the jet velocity is highly non-uniform within a radial range of 0.5mm.

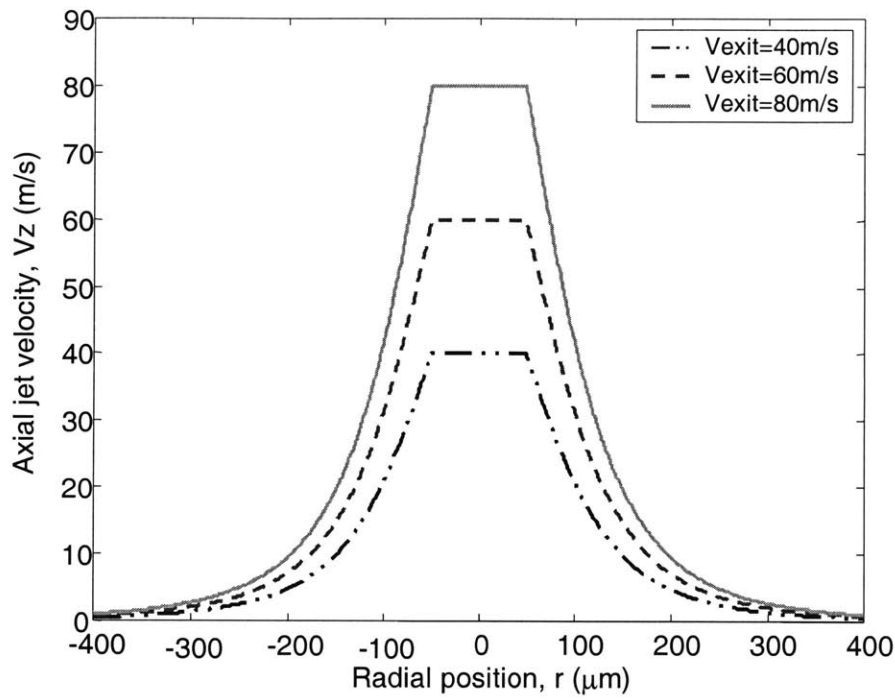


Figure 2-7. Axial velocity profile for turbulent flow ( $z=1.0\text{mm}$ )

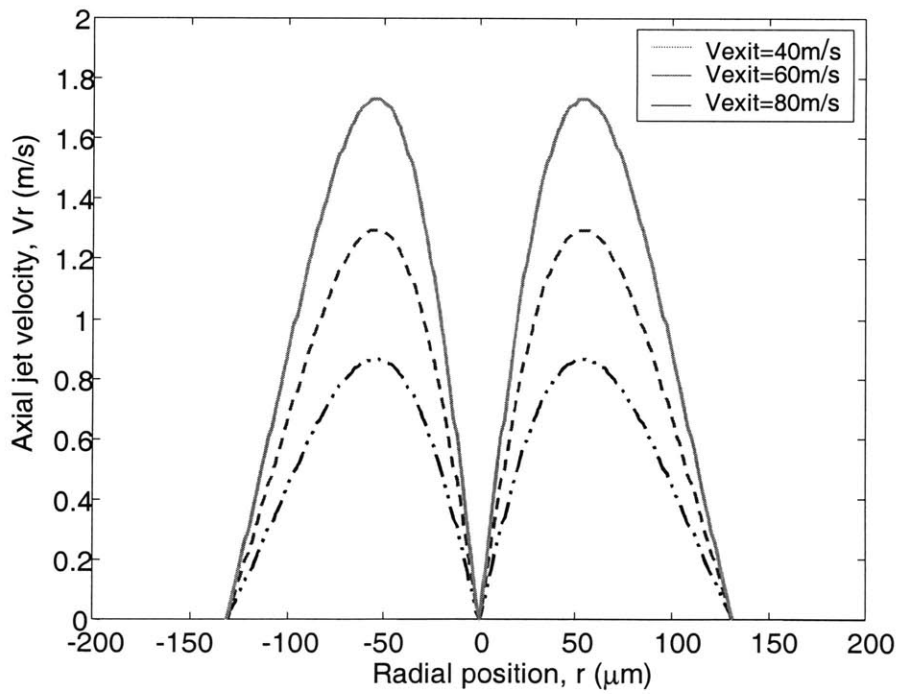


Figure 2-8. Radial velocity profile for turbulent flow ( $z=1.0\text{mm}$ )

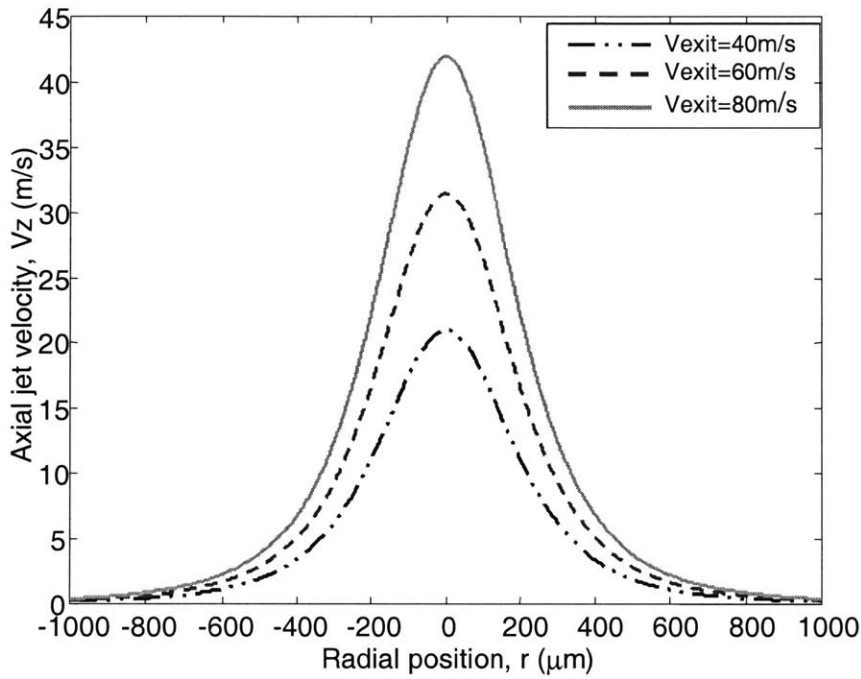


Figure 2-9. Axial velocity profile for turbulent flow ( $z=2.5\text{mm}$ )

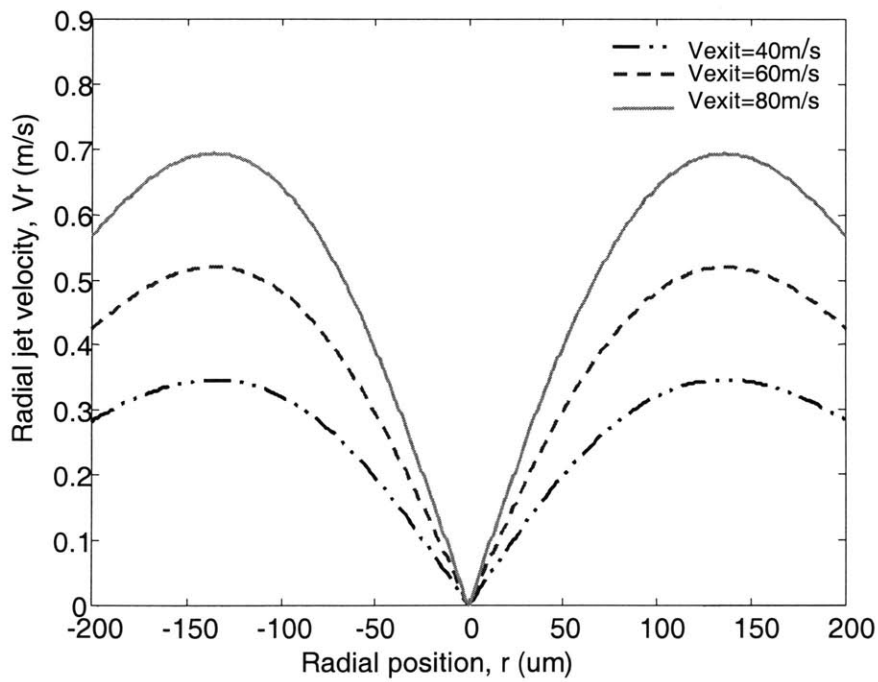


Figure 2-10. Radial velocity profile for turbulent flow ( $z=2.5\text{mm}$ )

# CHAPTER 3 HOT-WIRE SENSING OF MICOR-JET

## 3.1 Introduction

A hot-wire probe is a thermal transducer based on the convective heat transfer from a heated wire to fluid flow. Consequently any change in the flow, which affects heat transfer from the heated element, can be detected with hot-wire probe system.

Figure3-1 shows a schematic diagram of hot-wire operation. An electric current is passed through a fine wire, heating the wire to about 200°C. As the flow velocity varies, heat transfer from the wire varies. This in turn causes a variation in the heat balance of the wire and wire temperature. The wire is made from a material possessing a relative large temperature coefficient of resistance, e.g., tungsten and platinum. The wire temperature is monitored by measuring the wire resistance. A hot-wire probe can be operated either at constant temperature or constant current mode.

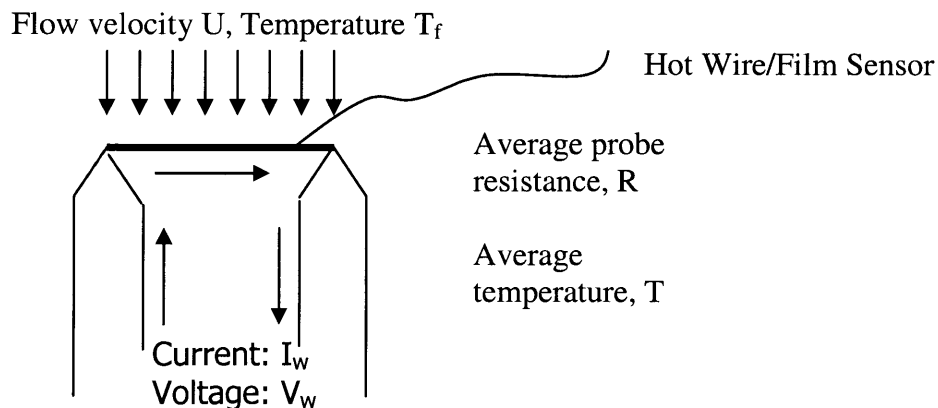


Figure 3-1. Hot-wire operation

Conventional applications of hot-wire anemometry require that the flow velocity along the wire is uniform. In this work the jet flow is confined in a sub-millimeter width. Existing models for hot-wire operation are not valid. The objective of this chapter is to develop a general heat transfer model to describe hot-wire responses to highly non-uniform flow.

### 3.2 Structure of hot-wire probes

Two types of probes are used in this work. Figure 3-2 shows the optical images of the hot-wire probe and hot-film probe. The hot-wire probe uses a fine tungsten wire as the sensing element. The sensing element for the hot-film probe is a quartz rod coated with a thin layer of platinum. The ends of the rod are coated with gold and welded to the supporting structure. The hot-film probe has a much thicker sensing element than the hot-wire probe.

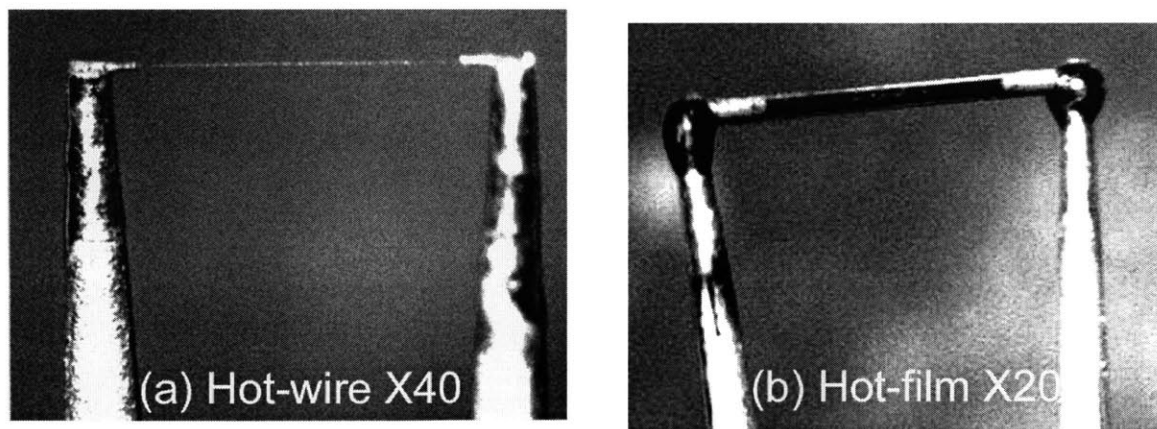
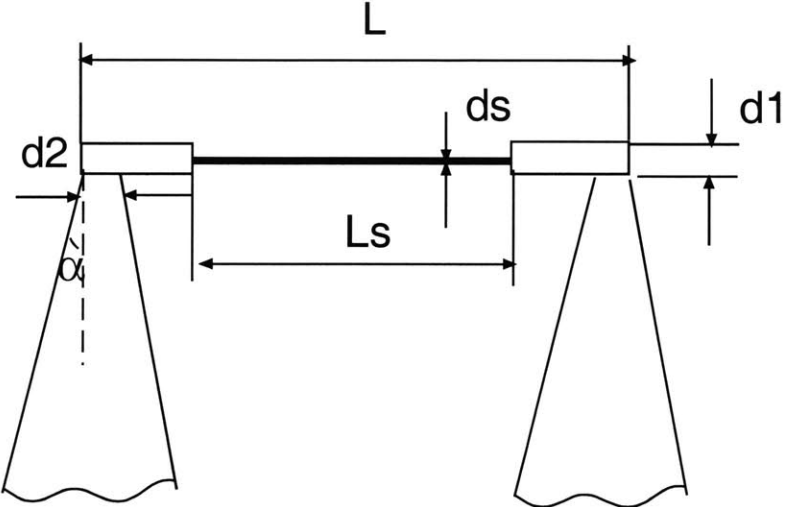
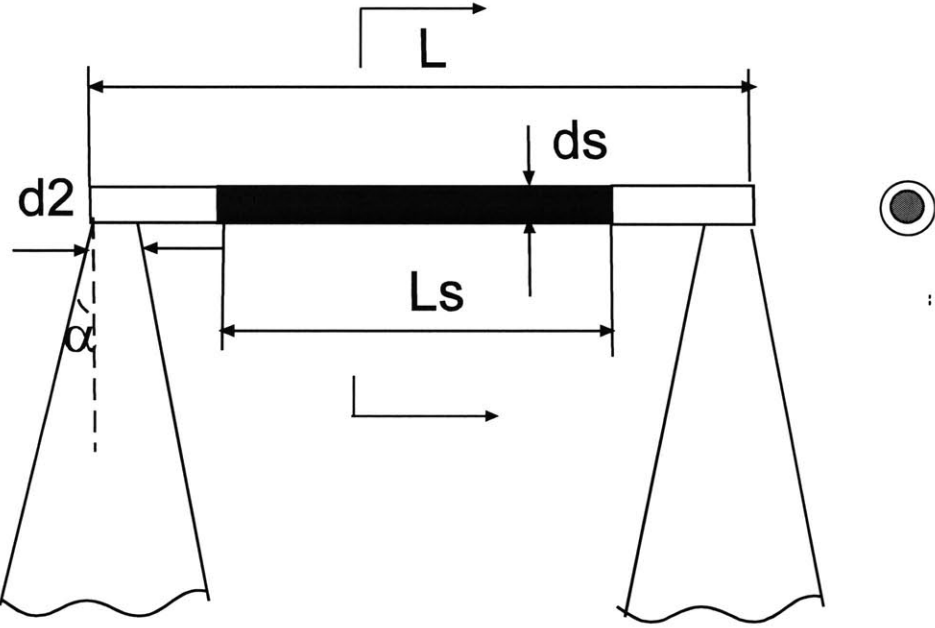


Figure 3-2. Optical images of hot-wire and hot-film probes

Figure 3-3 presents dimensional parameters used in this work to characterize hot-wire and hot-film probes. Table 3-1 lists dimensions of the probes used in this work.



(a) Hot-wire probe



(b) Hot-film probe

Figure 3-3. Structure of hot-wire and hot-film probes

Table 3-1. Dimensions of hot-wire probes

| Probe Type                        | Hot-Wire  | Hot-Film | Hot-Film |
|-----------------------------------|-----------|----------|----------|
| Model                             | 1210-T1.5 | 1210-20  | 1210-60  |
| Sensing Diameter $d_s$            | 3.8um     | 50.8um   | 152.4um  |
| Sensing length, $L_s$             | 1.27mm    | 1.02mm   | 2.03mm   |
| Total Length, $L$                 | 1.52mm    | 1.65mm   | 3.05mm   |
| Diameter of Wire Support, $d_1$   | 40um      | --       | --       |
| Diameter of Supporting Rod, $d_2$ | 100um     | 200um    | 200um    |
| $\alpha$                          | 5°        | 3°       | 3°       |

### 3.3 Heat transfer model

Operation of a hot-wire probe involves Joule heating in the sensing element, convective heat loss from the probe to surrounding fluid, and conductive heat loss from the sensing element to sensor supports. Compared to convection, radiation heat loss by the wire is negligible.

The energy equation for a hot-wire probe is

$$\rho A(x) C_p \frac{\partial T}{\partial t} = \frac{\partial}{\partial x} \left( A(x) K(x) \frac{\partial T}{\partial x} \right) + P(x) h(x) (T_0 - T(x)) + I^2 \rho_w(x) \quad (3.1)$$



where  $\rho$ ,  $C_p$  and  $K$  are the density, heat capacity and thermal conductivity of the wire respectively,  $A$  is the cross sectional area,  $P$  is the wire perimeter,  $T_0$  is the ambient temperature,  $I$  is the current, and  $\rho_w$  is the electrical resistance per unit length. Equation 3.1 is a general equation applicable to both hot-wire and hot-film probes. A hot-film probe has a uniform cross sectional area (Figure 3-4). On the other hand, a hot-wire probe has a much smaller diameter in the sensing zone (region 2 in Fig. 3-4). The electrical resistance in regions 1 and 3 is much smaller than that in region 2.

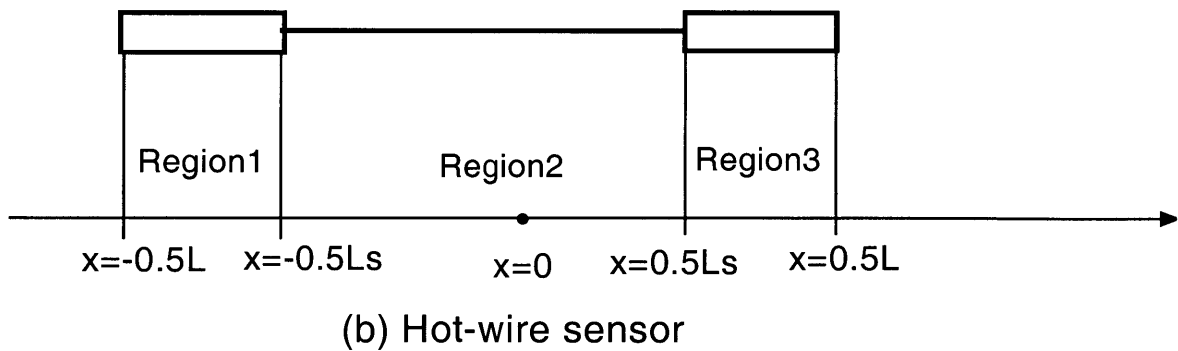
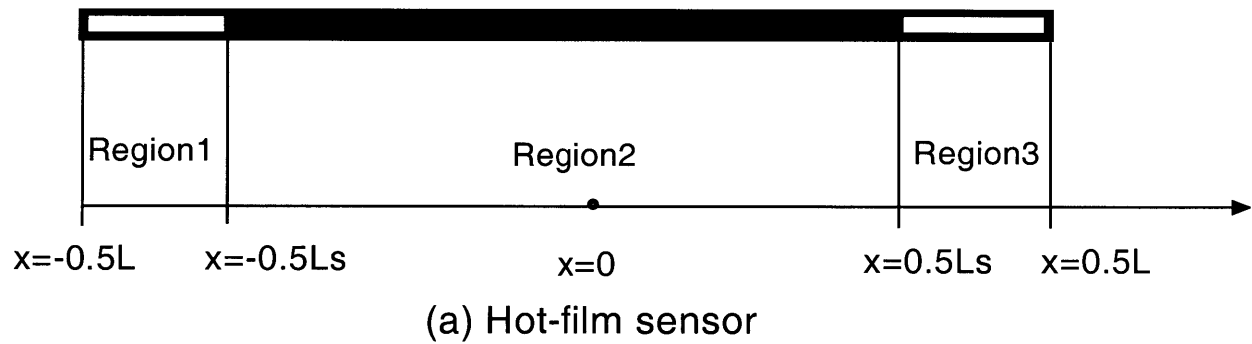


Figure 3-4. Schematic model of hot-wire and hot-film probes

The convective heat transfer coefficient,  $h$ , can be calculated from the Nusselt number,  $Nu$ ,

$$h(x) = \frac{Nu(x)Ka}{d_w(x)} \quad (3.2)$$

where  $Ka$  is the thermal conductivity of air, and  $d_w$  is the wire diameter.

For natural convection, the Nusselt number is correlated to the Rayleigh number (Incropera and Dewitt, 1996),

$$Nu_N = (0.6 + 0.321Ra^{1/6})^2 \quad (3.3)$$

$$Ra = \frac{g(T - T_0)d_w^3 \beta}{\alpha \gamma} \quad (3.4)$$

where  $\alpha$  is the thermal diffusivity of air, and  $\beta = \frac{1}{T_0}$  is the expansion coefficient.

For forced convection, the Nusselt number is correlated to the Reynolds number (Incropera and Dewitt, 1996),

$$Nu_F = 0.3 + 0.48\sqrt{Re_w} \quad (3.5)$$

$$Re_w = \frac{Vd_w}{L} \quad (3.6)$$

where  $V$  is the velocity component normal to the wire. Contribution to convective heat transfer by flow component parallel to the wire is neglected here.

For mixed convection, the effective Nusselt number is

$$Nu_e = (Nu_F^3 + Nu_N^3)^{1/3} \quad (3.7)$$

From equation 3.1, the thermal time constant of the sensing element is

$$\tau = \frac{\rho C_p A}{Ph} \quad (3.8)$$

As steady state, equation 3.1 becomes

$$\frac{d}{dx}(A(x)K(x)\frac{dT}{dx}) + P(x)h(x)(T_0 - T(x)) + I^2 \rho_w(x) = 0 \quad (3.9)$$

The boundary conditions for the sensing wire are

$$x = 0, \quad \frac{dT}{dx} = 0 \quad (3.10)$$

$$x = \pm \frac{L}{2}, T = T_b, \quad -KA \frac{dT}{dx} = Q_b \quad (3.11)$$

The supporting rods for the sensing wire are modeled as infinitely long fins of uniform cross sectional area (Figure 3-5). The rods conduct heat away from the sensing wire. Since the rods are outside micro-jet flow, they lose heat mainly through natural convection,

$$Q_b = \frac{1}{2} \pi d_2 \sqrt{Nu_e K_a K_r} (T_b - T_0) \quad (3.12)$$

where  $d_2$  is the rod diameter,  $K_r$  is the thermal conductivity of the rods. The Nusselt number is assumed to be 0.6 here.

Combining equations 3.11 and 3.12 yields the boundary condition at  $x = \pm \frac{L}{2}$ ,

$$x = \pm \frac{L}{2}, -KA \frac{dT}{dx} = \frac{1}{2} \pi d_2 \sqrt{Nu_e K_a K_r} (T - T_0) \quad (3.13)$$

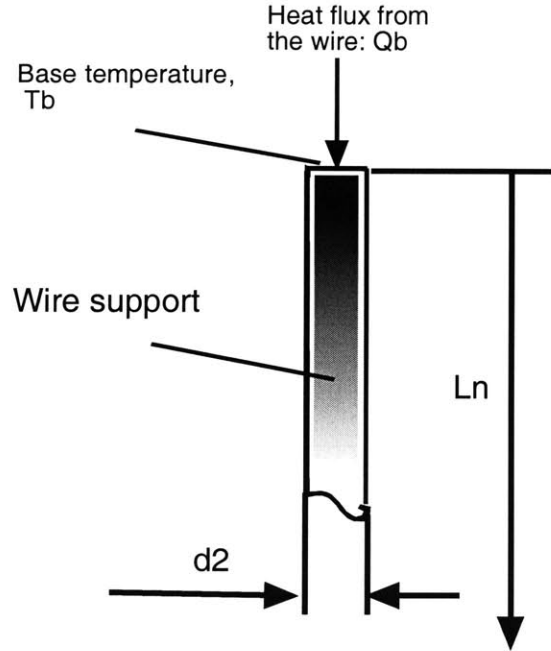


Figure 3-5. The heat transfer model for wire support

The electrical resistivity of sensing wire is

$$\rho_w = \frac{\rho_0(1 + \alpha_0(T - T_0))}{A} \quad (3.14)$$

where  $\rho_0$  is the electrical resistivity at  $0^\circ\text{C}$ , and  $\alpha_0$  is the temperature coefficient of resistivity. The total sensor resistance is

$$R = \int_{-L/2}^{L/2} \rho_w(x) dx = \int_{-L/2}^{L/2} \frac{\rho_0(1 + \alpha_0(T - T_0))}{A} dx \quad (3.15)$$

where the electrical resistance outside the sensing region is neglected.

The steady-state energy equation is solved numerically using the finite different method. The sensing wire is divided into 100 small elements. Table 3-2 lists properties used in the simulations. The fluid properties are evaluated at a film temperature of 110 °C.

Table 3-2. Physical properties used in simulations

|  |   |
|--|---|
| □ Thermal conductivity of air, $K_a$   | 0.034W/m-K                                |
| Thermal diffusivity of air, $\alpha$   | $.83 \cdot 10^{-5} \text{ m}^2/\text{s}$  |
| Viscosity of air, $\nu$                | $2.64 \cdot 10^{-5} \text{ m}^2/\text{s}$ |
| Thermal conductivity of tungsten, $K$  | 159W/m-K                                  |
| Thermal conductivity of quartz, $K$    | 7.6W/m-K                                  |
| Heat capacity of tungsten, $\rho C_p$  | $2.6 \cdot 10^6 \text{ J/m}^3\text{-K}$   |
| Heat capacity of tungsten, $\rho C_p$  | $2.3 \cdot 10^6 \text{ J/m}^3\text{-K}$   |
| Thermal conductivity of support, $K_r$ | 16W/m-K                                   |

The total heating power is

$$Q_{in} = I^2 R \quad (3.16)$$

Heat loss by convection is

$$Q_{conv} = \int_{-L/2}^{L/2} h(x)P(x)(T - T_0)dx \quad (3.17)$$

Heat loss by conduction to wire supports is

$$Q_{cond} = 2Q_b \quad (3.18)$$

The numerical solutions are found to satisfy the energy balance within 0.01%,

$$\frac{Q_{in} - Q_{cond} - Q_{conv}}{Q_{in}} \leq 0.01\% \quad (3.19)$$

### 3.4 Results and discussion

#### 3.4.1 Hot-wire sensing in still air

Experiments were conducted to validate the heat transfer model for hot-wire probes. A TSI1210-60 hot-film probe was heated by a constant current in still air. Figure3-6 shows the simulated temperature distribution along the probe at a constant current of 100mA. Heat is generated mainly within the 2mm long sensing region at the center. Conductive heat loss through the wire supports is significant, leading to a highly non-uniform temperature distribution. The total electrical resistance of the probe can be calculated through equation 3.15. Figure3-7 compares the predicted probe resistance with experimental results. Model prediction agrees with the experimental results.

Figure3-7 compares the average probe temperature. The probe temperature is deduced from measured probe resistance,

$$\bar{T} = \frac{R - R_0}{R_0 \alpha_0} \quad (3.20)$$

where  $R_0$  is the probe resistance at  $0^\circ\text{C}$ . The predicted average sensing temperature is the average wire temperature in the sensing zone,

$$\bar{T} = \frac{1}{Ls} \int_{-L/2}^{L/2} T(x) dx \quad (3.21)$$

The results show that the center wire temperature can be  $40^\circ\text{C}$  higher than the average wire temperature at 100mA.

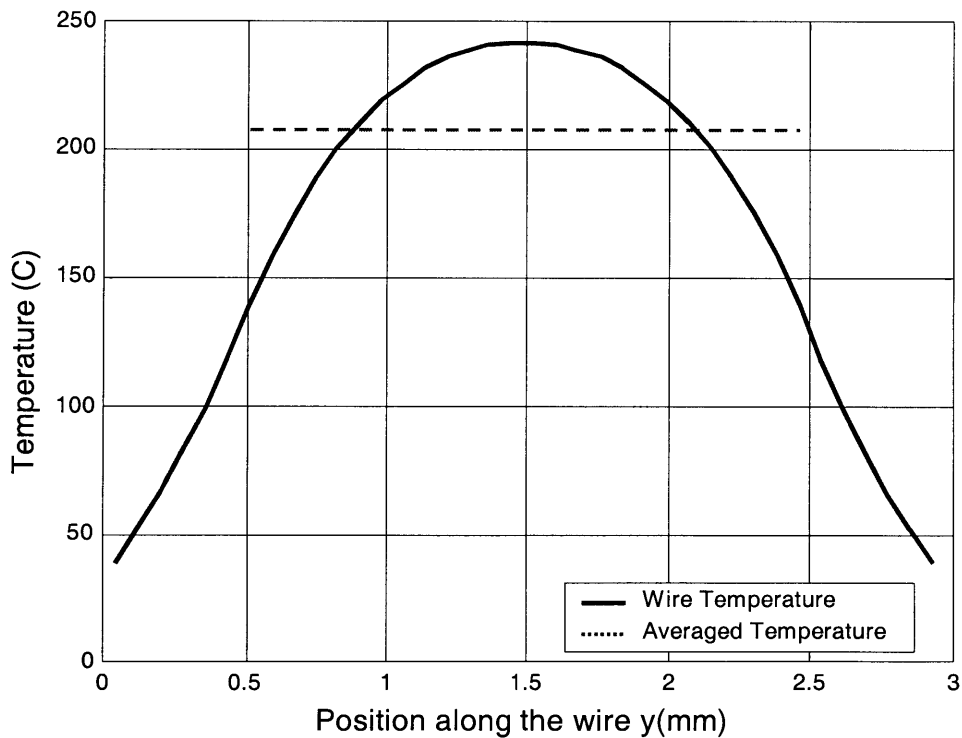


Figure 3-6. The temperature distribution along the wire (TSI1210-60, CC, I=100 mA)

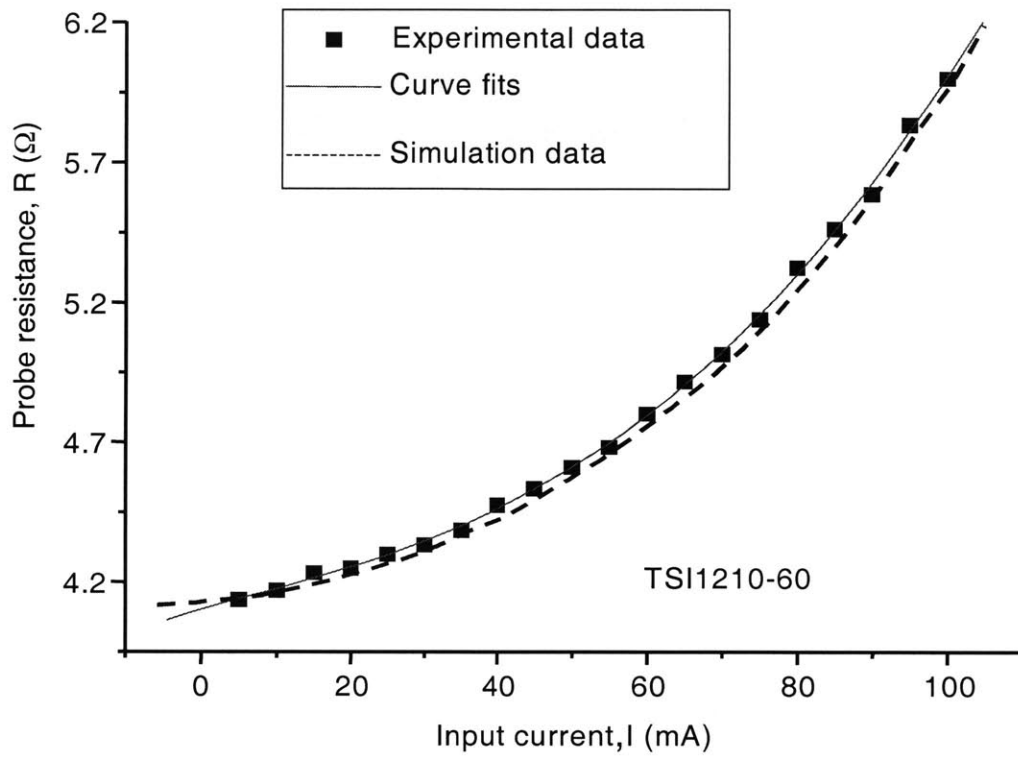


Figure 3-7. Electrical resistance of hot-film probe in still air



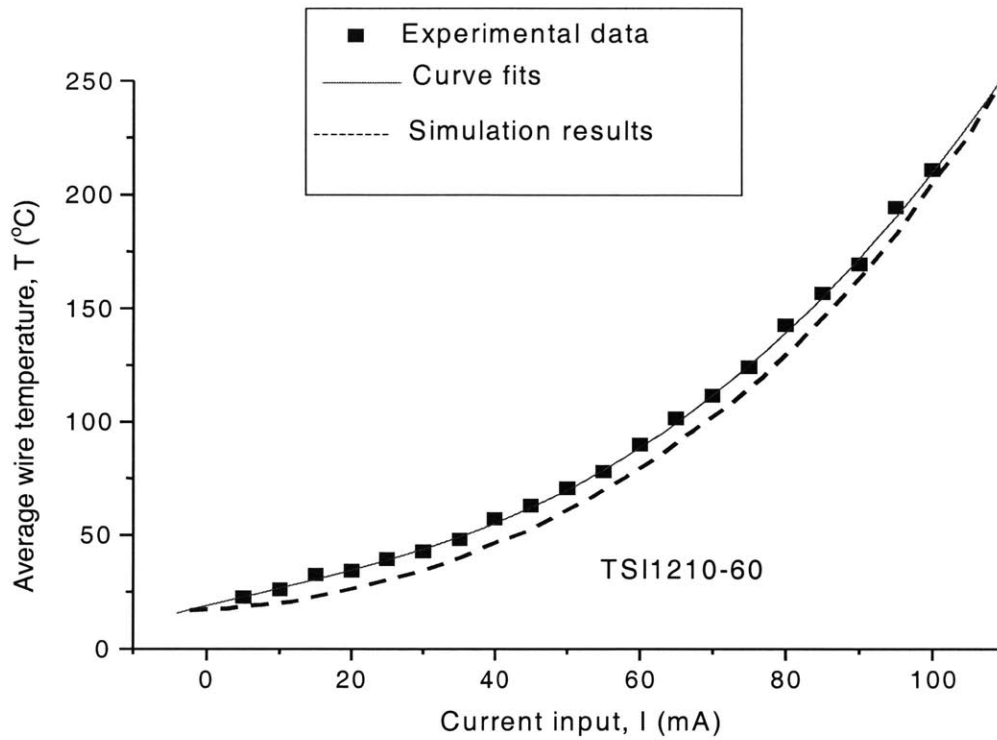


Figure 3-8. Average wire temperature in still air

### 3.4.2 Hot-wire sensing in uniform flow

Figure3-9 compares the predicted average probe temperature with that deduced from measured probe resistance in a uniform flow. The flow velocity was determined using a pitot tube. The TSI1210-60 probe was operated at a constant current of 100mA. By neglecting conductive heat loss by probe supports, Joule heating of the sensing wire is balanced by convective heat loss,

$$I^2 R = \pi d_s L_s h (T - T_0) \quad (3.22)$$

The convective heat transfer coefficient can be expressed as

$$h = C + D\sqrt{V} \quad (3.23)$$

where C and D are probe constant (Bruun, 1995). The probe resistance is related to the probe resistance is related to the probe temperature,

$$R = R_0 (1 + \alpha T) \quad (3.24)$$

$$R_a = R_0 (1 + \alpha T_0) \quad (3.25)$$

where  $R_a$  is the probe resistance at the ambient temperature,  $T_0$ . Combing the above equations lead to

$$\frac{R}{R - R_a} = \frac{\pi d_s L_s (C + D\sqrt{V})}{R_0 \alpha_0 I^2} = A + B\sqrt{V} \text{ at constant sensing current.} \quad (3.26)$$

A and B are constants. Figure3-10 presents the ratio,  $R/(R-R_a)$ , as a function of flow velocity. Above 5m/s, the experimental data follow a straight line, which agrees with the theory prediction. The results suggest that the experimental data are valid. At low velocities, conductive heat loss to the probe supports becomes more and more important. As a result, the experimental data fall below the straight line.

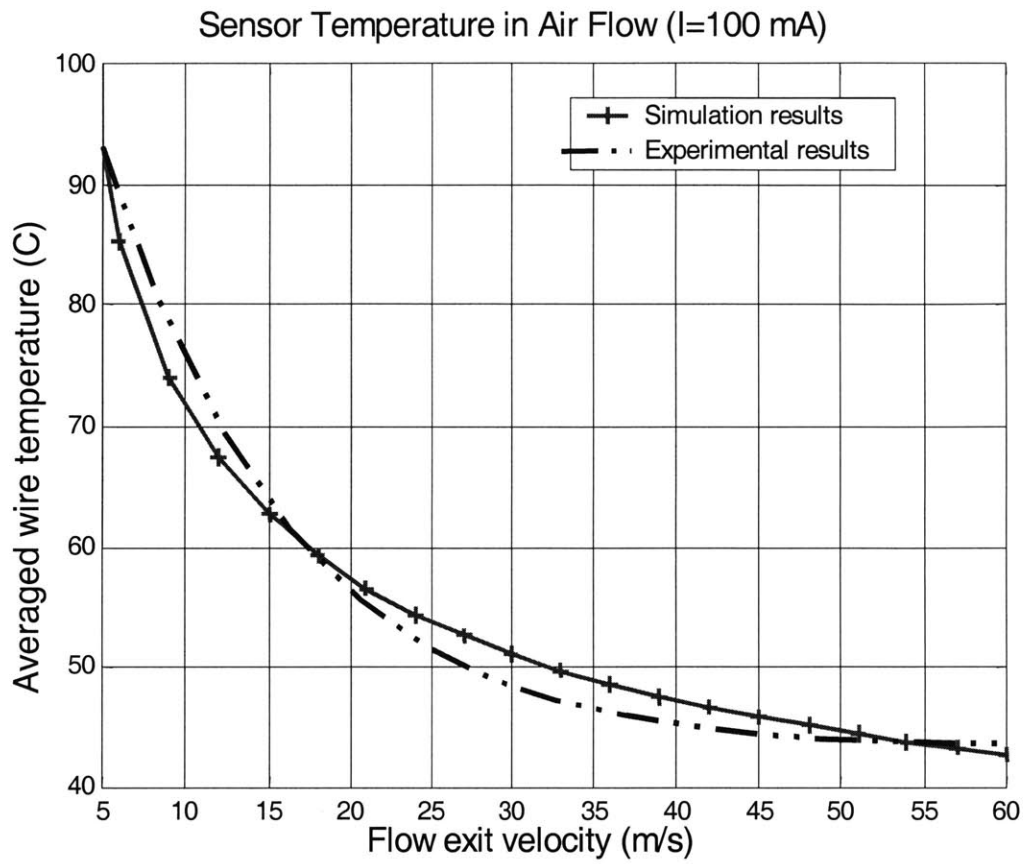


Figure 3-9. Effect of convection on wire temperature (I=100mA)

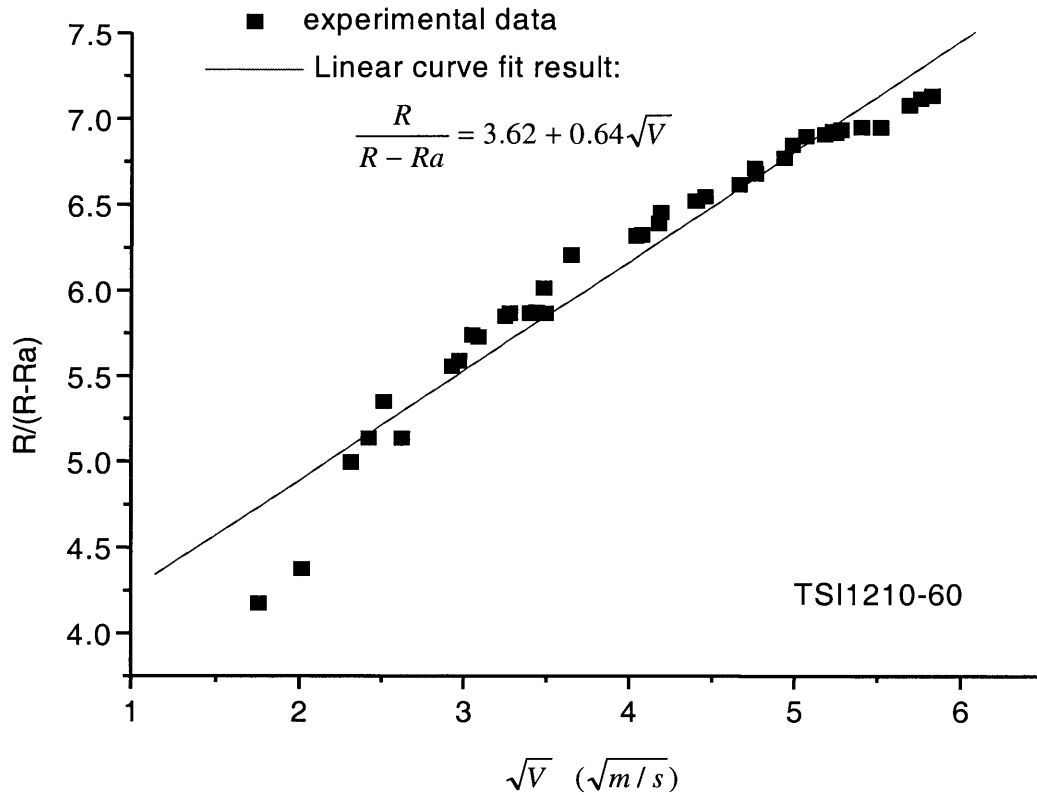


Figure 3-10. Correlation of probe resistance (I=100mA)

### 3.4.3 Hot-wire sensing profiles for micro-jet flow

By combined the heat transfer model of hot-wire probes with jet velocity fields presented in chapter 2, local wire temperature can be determined. Figure3-11 presents a schematic distribution of the wire temperature. The typical width of micro-jets is smaller than the length of a sensing wire. A micro-jet produces intense cooling in a small region of the wire.

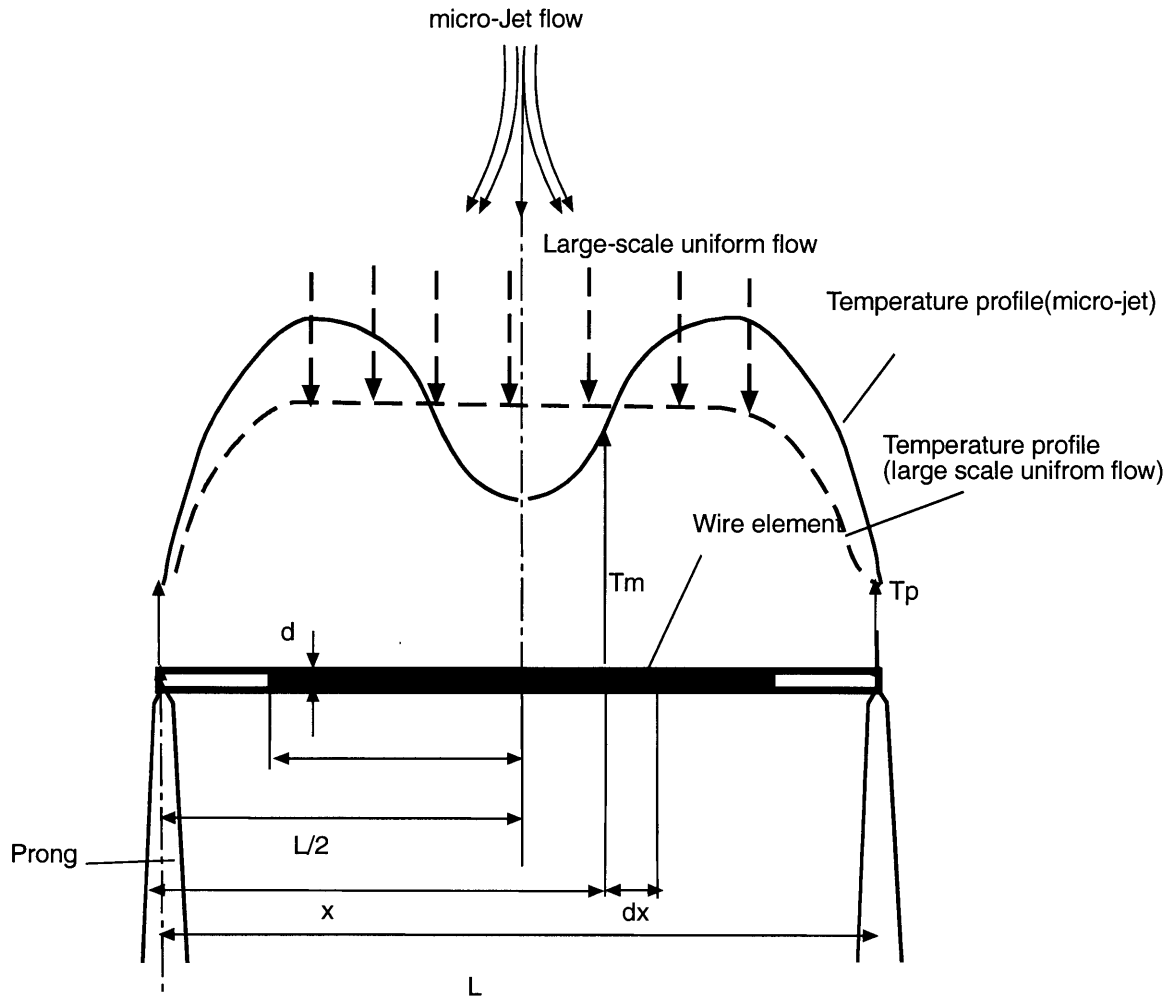


Figure 3-11. Horizontal wire in mixed convection and conduction

Figure 3-12 shows the predicted temperature distribution profile along a TSI 1210-60 probe when the probe is at the center of a jet. The probe is operated at a constant current of 100mA and is located at an axial position of  $z=1\text{mm}$ .

When the probe is placed across the center of the jet, convective cooling by the jet is the strongest, resulting in the lowest average wire temperature. If the probe is located near the edge of the jet, the sensing wire is only slightly cooled, leading to a higher average wire temperature. Figure 3-13 simulates the average probe temperature as the probe scans across the jet.

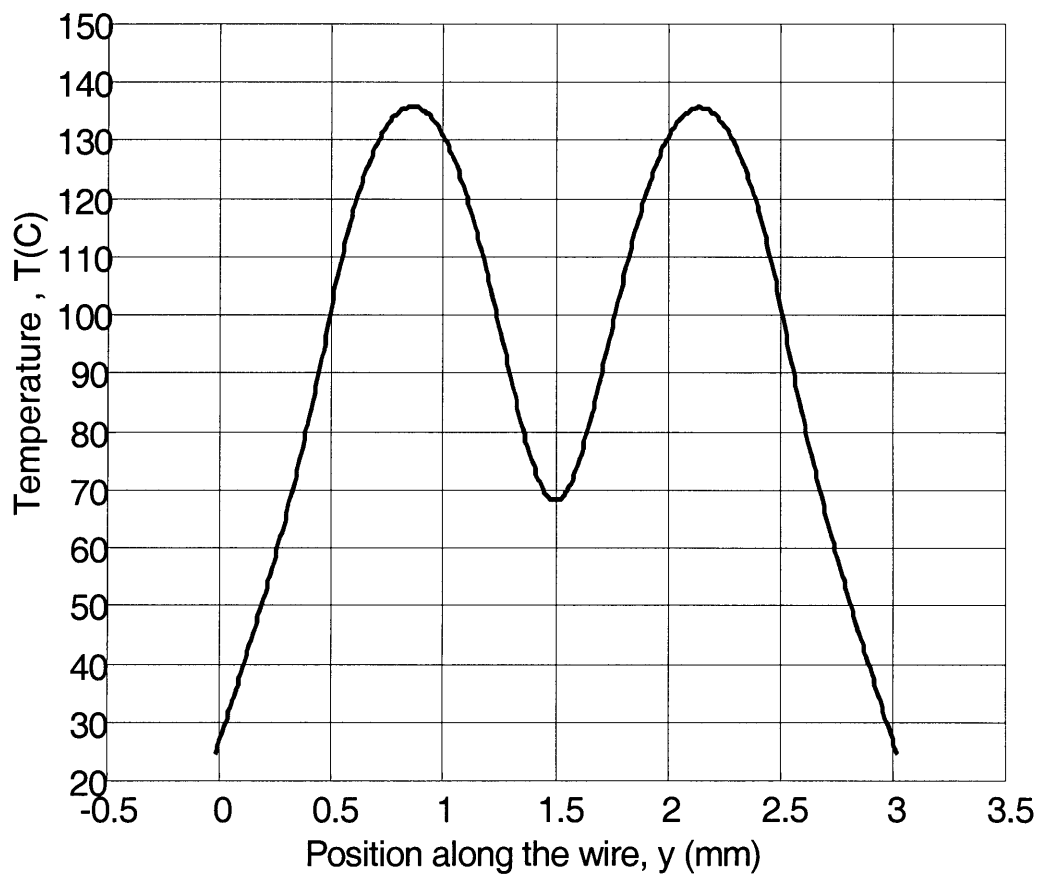


Figure 3-12. Temperature distribution along the wire when HFA sits at the jet's center

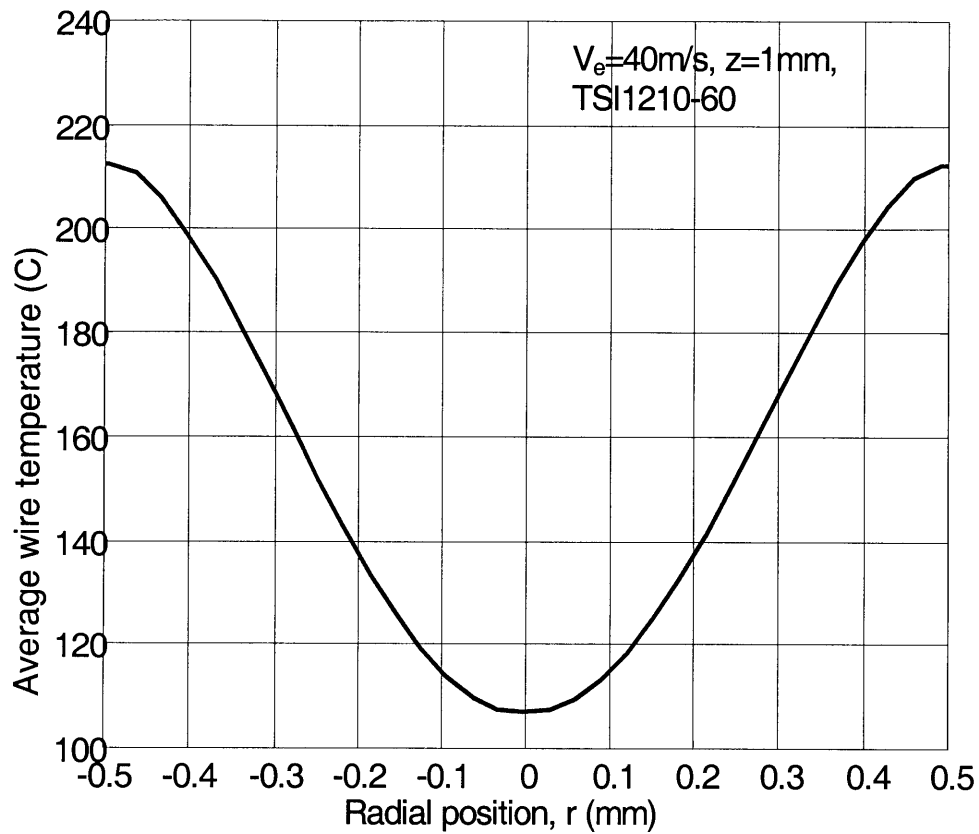


Figure 3-13. Probe temperature during scanning ( $I=100\text{mA}$ )

When the exit jet velocity increases, whatever the jet is laminar or turbulent, the cooling effect becomes stronger and the average probe temperature decreases (Figure 3-14).

According to the simulation results in chapter 2, when the axis position increases, the jet expands, and the centerline jet velocity decreases. Figure 3-15 shows that average probe wire temperature decreases with the axial position and the scanning.

STI1210-60 HFA, axis position z=1mm

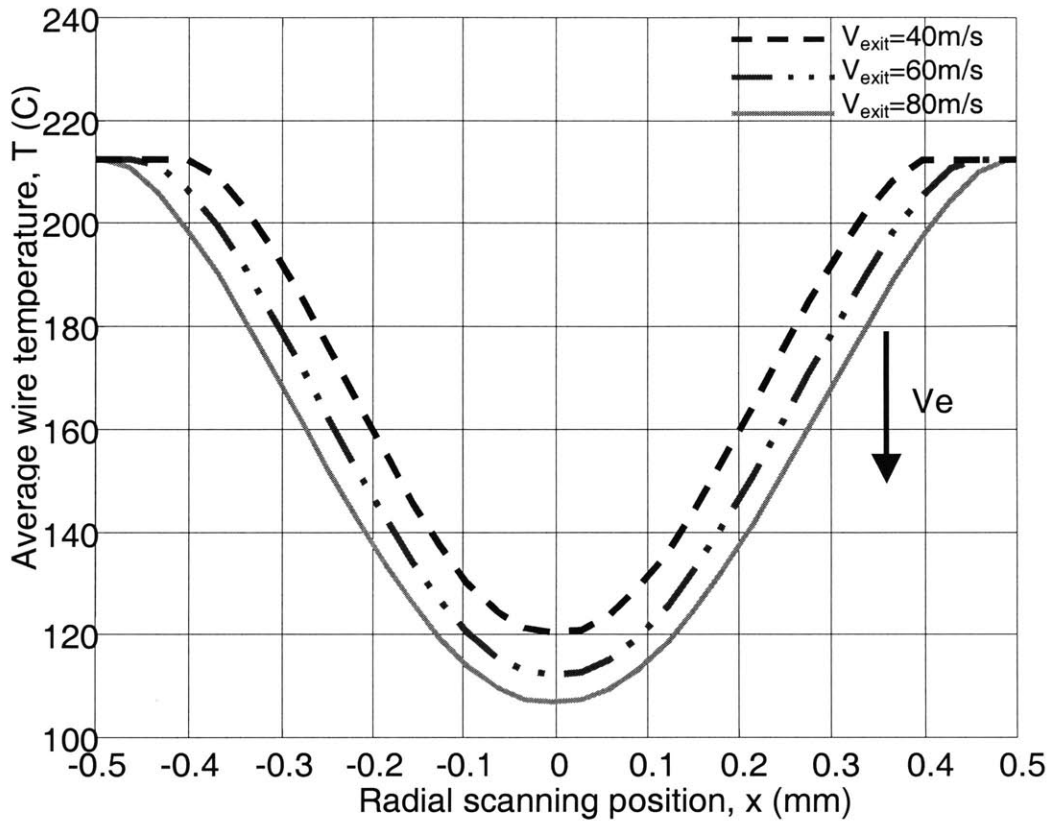


Figure 3-14. Effect of jet velocity on scanning profiles



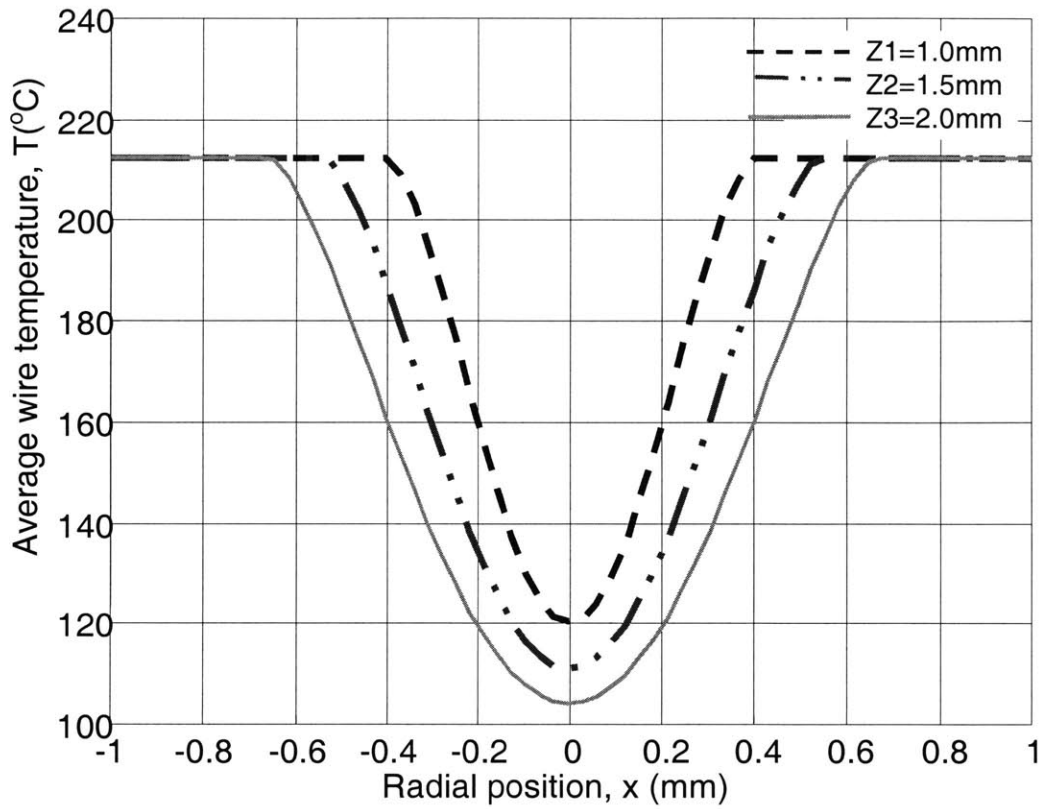


Figure 3-15. Effect of axial position on scanning profiles

# Chapter 4 EXPERIMENTAL SETUP

An experimental system was established to characterize micro-jet flow with hot-wire probes. It consists of supply of regulated compress air, hot-wire probe and signal conditioning circuits, probe scanning system and data acquisition system.

## 4.1 Air supply

Figure 4-1 shows a schematic diagram of the air supply system. A dry diaphragm air compressor is used to avoid oil contamination of the metering tube. A large gas filter is used to remove particles larger than 1  $\mu\text{m}$ . The gas flow rate is monitored by a rotary flow meter. A pressure transducer monitors the transient line pressure. A digital pressure gauge with  $\pm 1\%$  accuracy in serial is used to calibrate the pressure transducer. The pressure transducer has a linear response,

$$P=25.0V(V)-26.2 \text{ (kPa)} \tag{4.1}$$

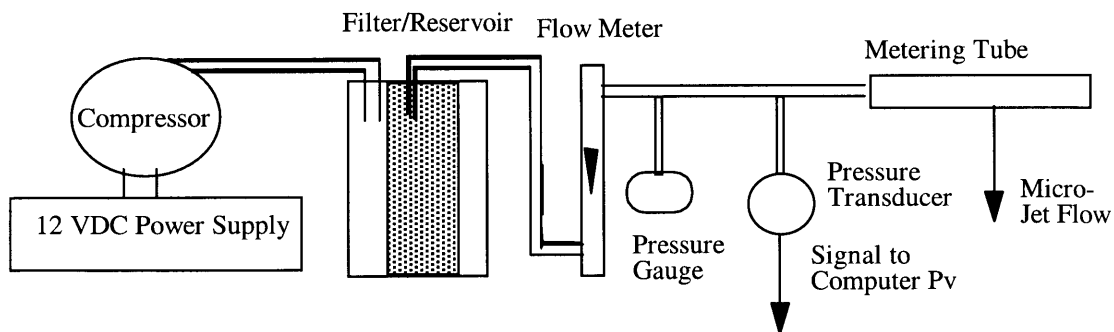


Figure 4-1. Schematic diagram of air supply system

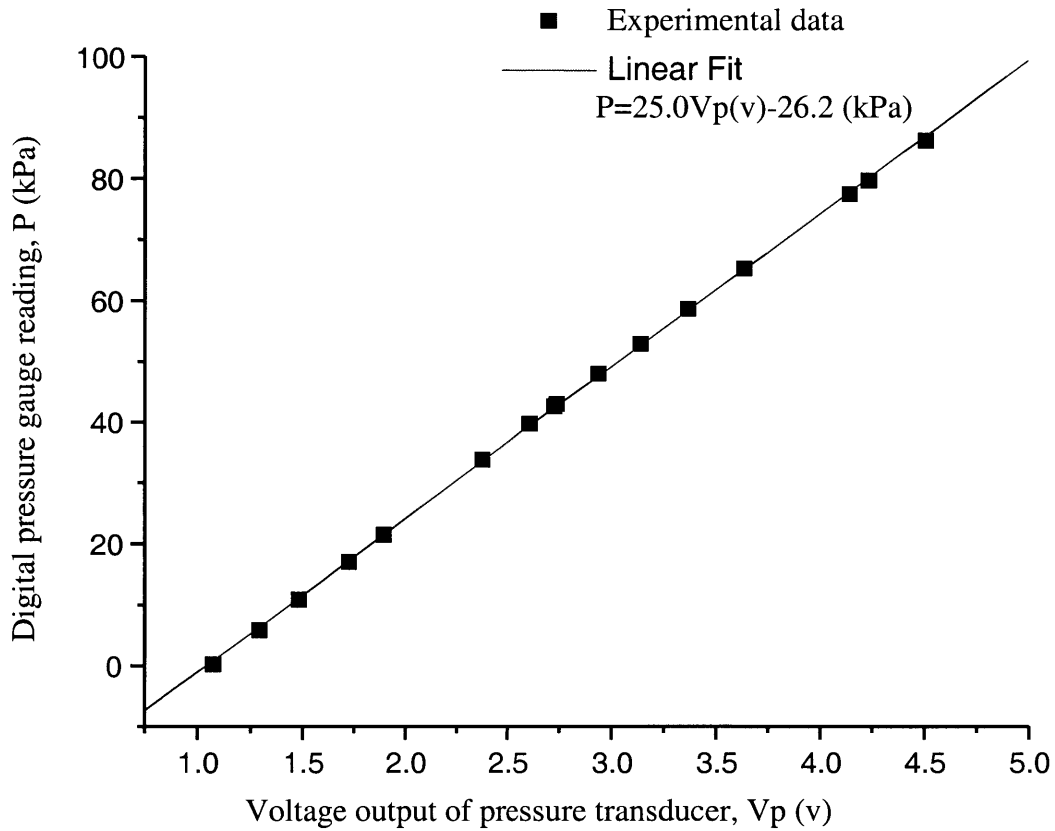


Figure 4-2. Calibration of pressure transducer

#### 4-2 Hot-wire probes and signal conditioning

Commercially available TSI hot-wire probes are used for micro-jet sensing. Figure 4-3 illustrates typical dimensions of the probes. Table 4-1 lists electrical characteristics of the probes. The probes were operated at a nominal temperature of 200<sup>0</sup>C in this work.

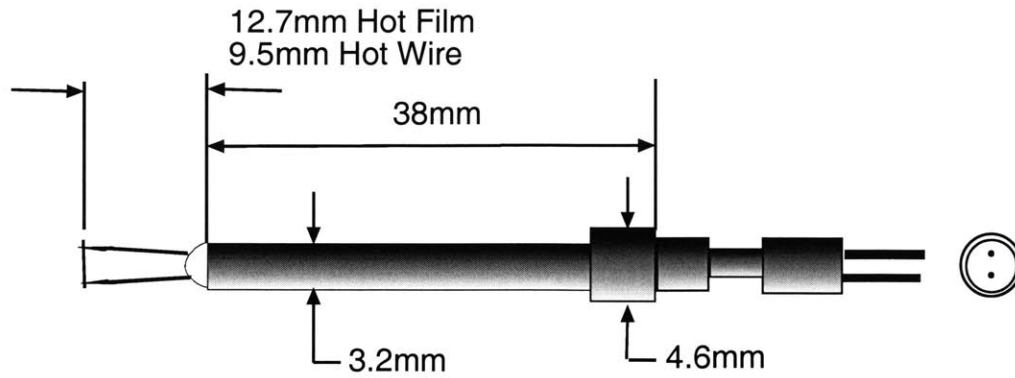


Figure 4-3. Schematic diagram of TSI1210 general purpose probe (-T1.5, -20, -60)

Table 4-1. Characteristics of TSI hot-wire probes

| Probe type                                    | Hot-Wire    | Hot-Film    | Hot-Film    |
|---|-------------|-------------|-------------|
| Model   | 1210-T1.5   | 1210-20     | 1210-60     |
| Serial number                                 | 225479      | #27         | 996002      |
| Working Temperature                           | 200°C       | 200°C       | 200°C       |
| Total probe resistance at 0°C, R <sub>0</sub> | 5.90Ω       | 5.94 Ω      | 4.21 Ω      |
| Total probe resistance at 200 °C              | 6.74Ω       | 6.42Ω       | 4.69Ω       |
| Lead resistance                               | 0.19Ω       | 0.65Ω       | 0.20Ω       |
| Working current                               | 34mA        | 65mA        | 100mA       |
| Temperature coefficient                       | 0.0042 / °C | 0.0024 / °C | 0.0024 / °C |

The probes can be operated either under the constant-current mode or constant-temperature mode. Figure 4-4 shows the circuit used for the constant-current mode.

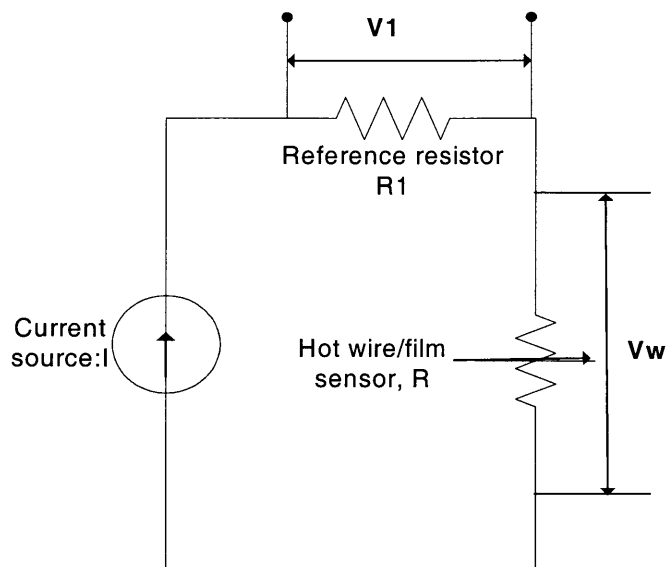


Figure 4-4. Constant-current circuit

For constant-temperature operations, a commercially available control module from TSI is used. It contains a Wheatstone bridge circuit with the sensor as one arm of the bridge. A differential feedback amplifier senses the bridge unbalance and adds current to hold the sensor temperature constant. Before the probe is placed in operation, the control resistor is set to a value so that the bridge will be balanced at the working temperature of the probe. An increase in fluid velocity cools the sensor and unbalances the bridge. This causes the feedback amplifier to increase the sensor heating current and to bring the bridge back into balance. Since the feedback loop responds rapidly, the sensor temperature remains constant. The voltage drop across the probe is related to the fluid velocity. Figure 4-5 shows a typical constant-temperature circuit.

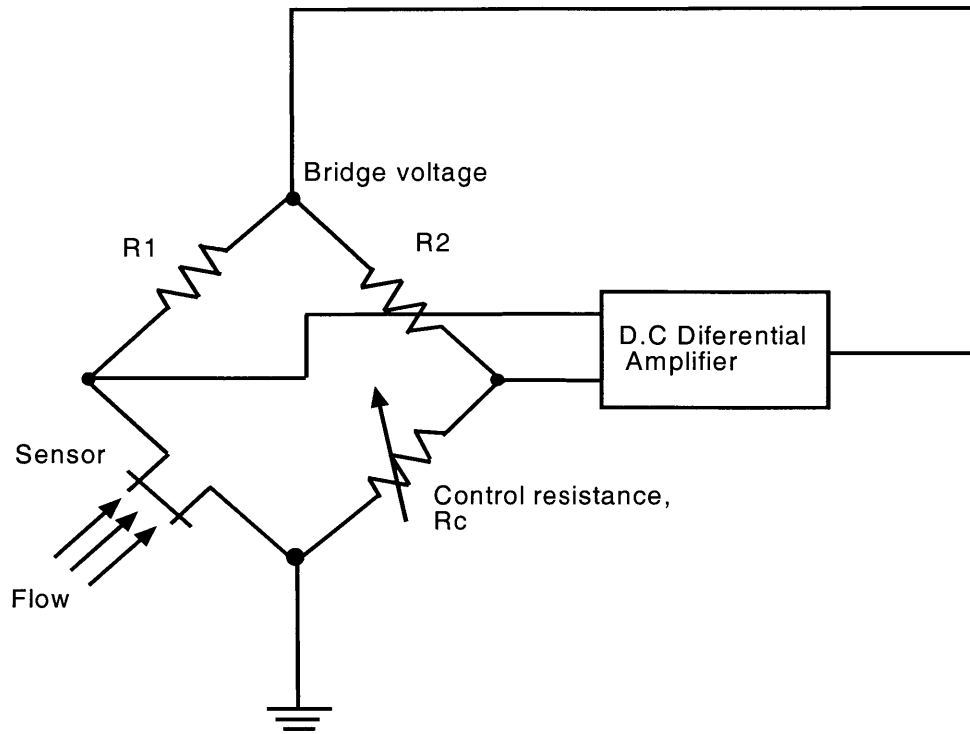


Figure 4-5. Constant-temperature circuit

### 4.3 Probe scanning system

Figure 4-6 shows a schematic diagram of the probe scanning system. A hot-wire probe is mounted on a three-dimensional translational stage. The probe position in the y and z directions is adjusted manually with micrometers. During measurements, the stage is driven along the x direction at a constant speed by a DC motor. An encoder provides the stage position with  $\pm 1 \mu\text{m}$  accuracy.

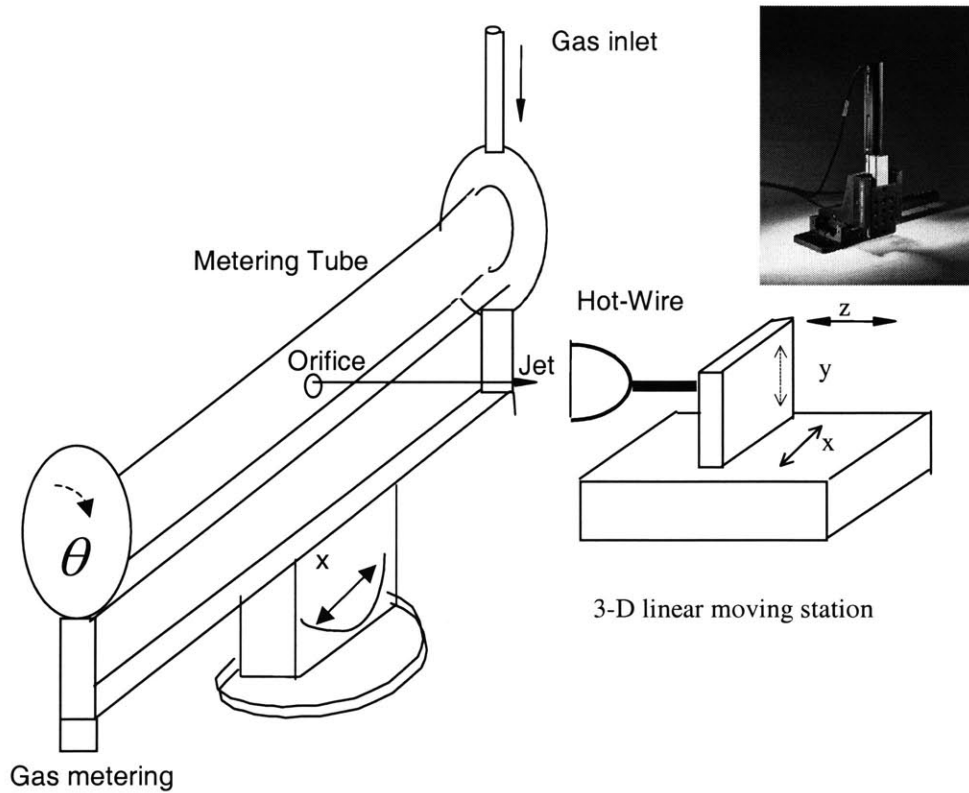


Figure 4-6. Experimental setup

A typical experiment involves (1) determination of probe position, (2) probe alignment, (3) alignment of the scanning stage, and (4) probe scanning. A dummy probe is used to determine the probe position. It has the same structure and size as the working probes except there is no wire attached between wire supports. As the probe is moved slowly along the  $z$  direction approaching the metering tube, the electrical resistance between them is monitored. When the probe contacts the tube, the resistance drops sharply and the probe position in the  $z$  direction is set to  $z=0$ . The probe is then moved into a jet and adjusted along the  $y$  direction until it is centered. To align the scanning stage parallel to the tube, the distance between the probe and metering tube is determined at the two travel

extremes of the stage along the x direction using the above electrical resistance method. Over a travel range of 25mm, the stage is aligned parallel to the metering tube within 20um. During measurements, the probe is driven at a constant speed of 60um/s when the probe is near or within a jet and at about 200um/s when the probe is traveling between jets.



## Chapter 5 HOT-WIRE SCANNING OF MICRO-JETS

This chapter investigates effects of different operation modes and different probes on micro-jet sensing sensitivity, orifice-to-orifice flow uniformity, and relationship between jet flow and orifice defects.

### **5.1 Effect of sensor types sensing results**

Hot-film probes have a much larger diameter and thermal time constant than hot-wire probes. Figure 5-1 and 5-2 present typical results from a TSI 1210-T1.5 hot-wire probe and TSI1210-20 hot-film probe under the constant-current condition. The results show that the two probes provide similar sensitivity and signal-to-noise ratio. Since hot-wire probes are significantly shorter than hot-film probes, they are difficult to align to the center of orifices. They are also very fragile. Hot-film probes are used in this work.

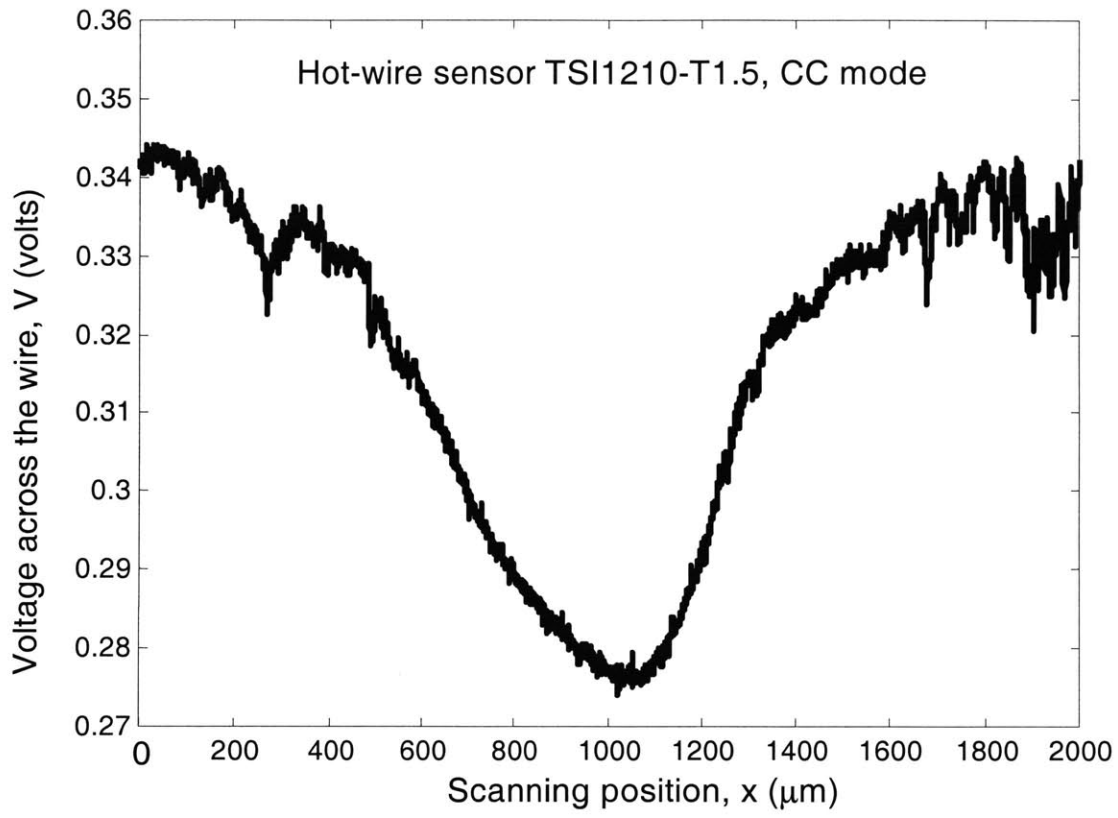


Figure 5-1. Hot-wire probe sensing of micro-jet flow

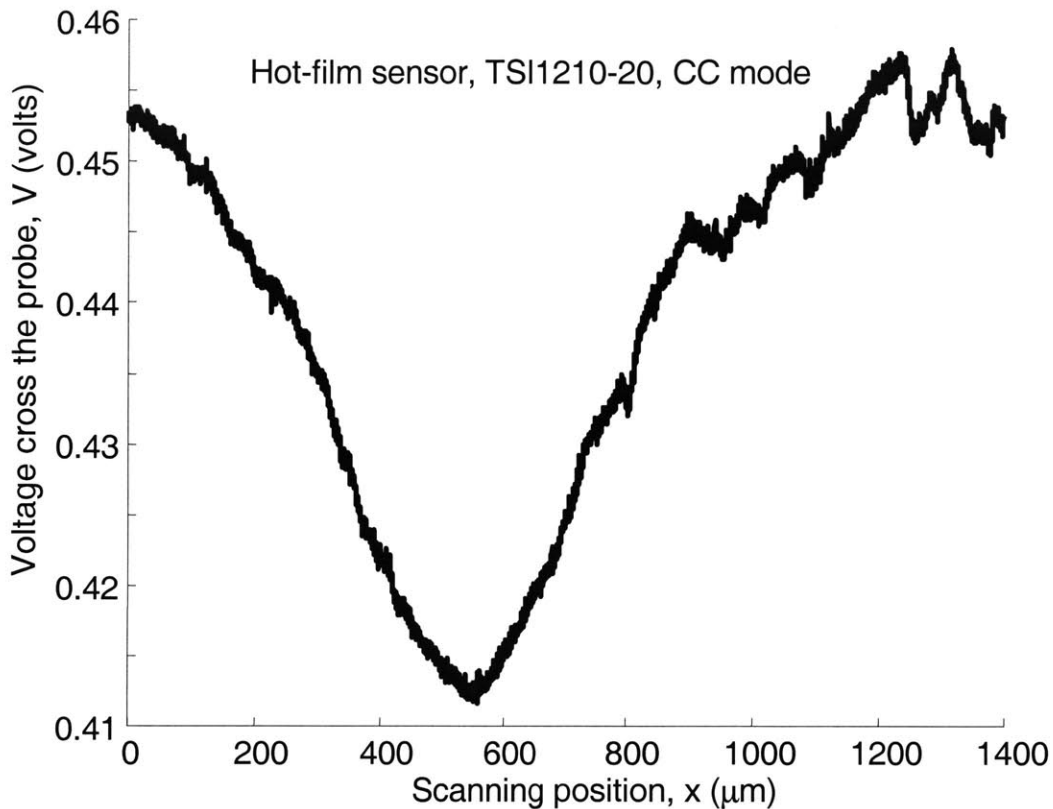


Figure 5-2. Hot-film probe sensing of micro-jet flow

## 5.2 Sensitivity to axial position

The cooling effect to a hot-wire probe is the strongest when probe is at the centerline of the jet. Figure 5-3 shows the average probe temperature versus probe axial position at a constant-current of 100mA. The nominal wire temperature in still air at this current is 200°C. As the probe moves away from an orifice, the flow velocity decreases. The overall convective cooling of the probe decreases, leading to an increase of the averaged probe temperature. Also, as fluid particles move away from the orifice, turbulent eddies develop bigger and bigger, resulting a larger fluctuation of the wire temperature. The probe temperature decreases with the increase of the exit jet velocity. The probe sensing

noise decreases with the jet velocity, suggesting that hot-film sensing technology has good sensitivity for micro-jet flow when the probe is close to the orifice.

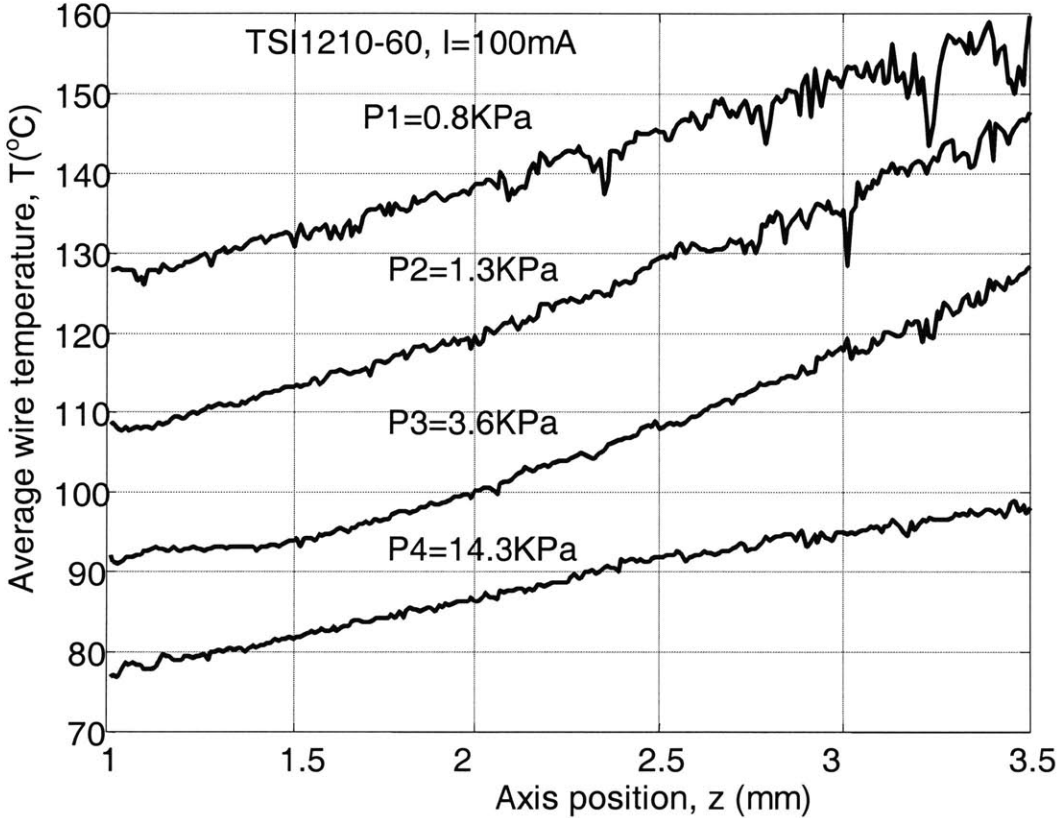


Figure 5-3. Scanning along jet centerline

When a probe is very close to the orifice, the probe response is not sensitive to the probe position (figure 5-4), indicating that the probe is within the potential core of the jet.

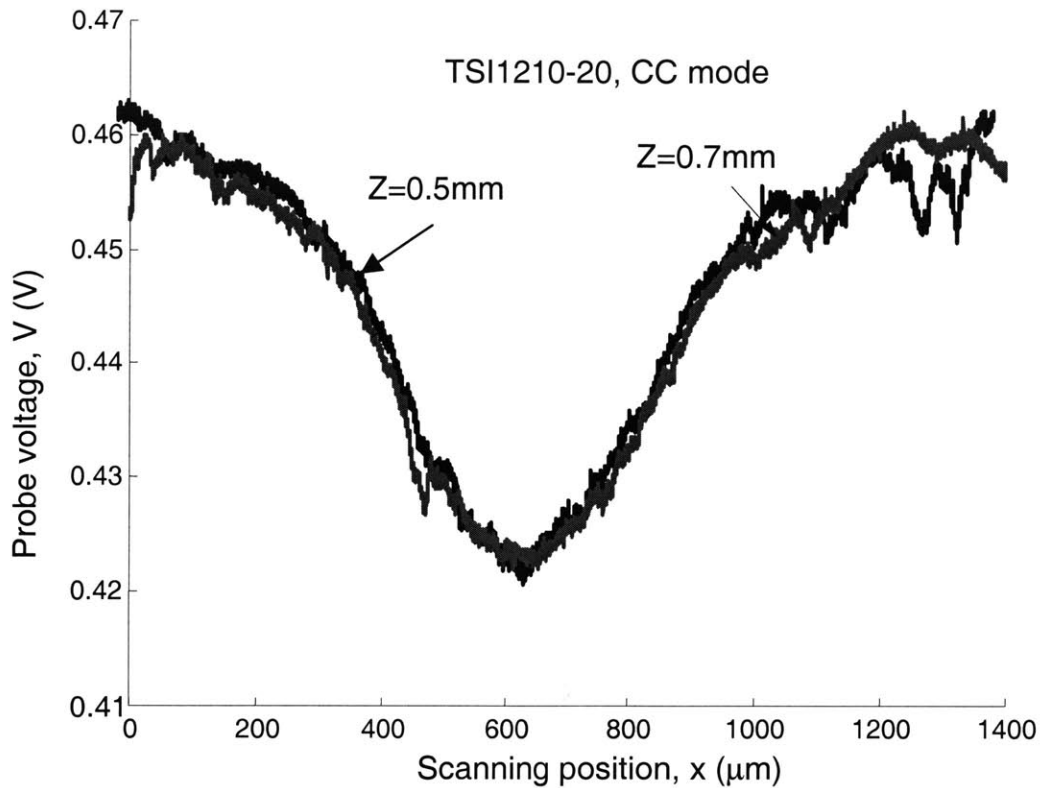


Figure 5-4. Hot-film sensing of micro-jet flow near orifice

### 5.3 Sensitivity to backpressure

Figures 5-5 and 5-6 show the scanning profiles at different pressures for two neighboring orifices, #23 and #24. The orifices are indexed from the tube inlet. At the nominal gauge pressure of 7.5kPa, the exit jet velocity is estimated between 50m/s and 70m/s. Although the drop of the backpressure is only 0.7%, the hot-wire probe can clearly distinguish this slight variation.

The variation of the exit jet velocity is related to the backpressure as

$$\Delta V = 0.5 \frac{\Delta P}{P_n} V_n \quad (5.1)$$

Using the nominal pressure of  $P_n = 7.5\text{kPa}$  and nominal velocity of  $V_n = 70\text{m/s}$ , the hot-film sensing system can detect jet velocity changes as small as  $0.3\text{m/s}$ .

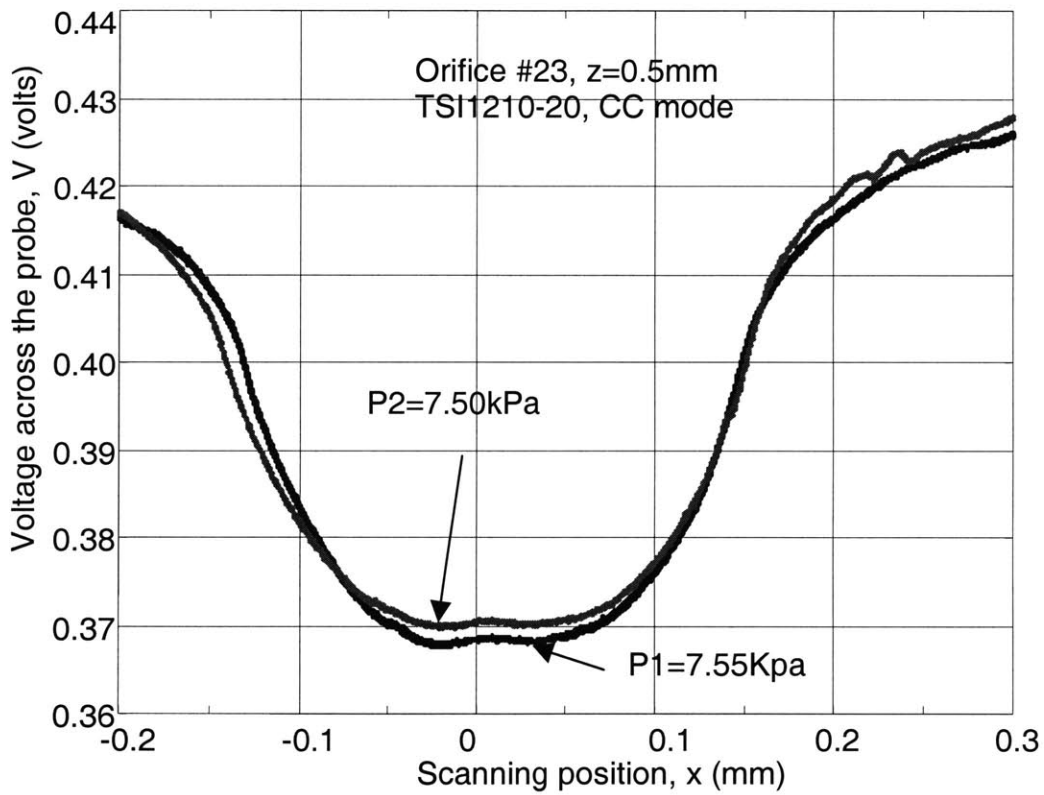


Figure 5-5. Hot-film scanning of orifice #23

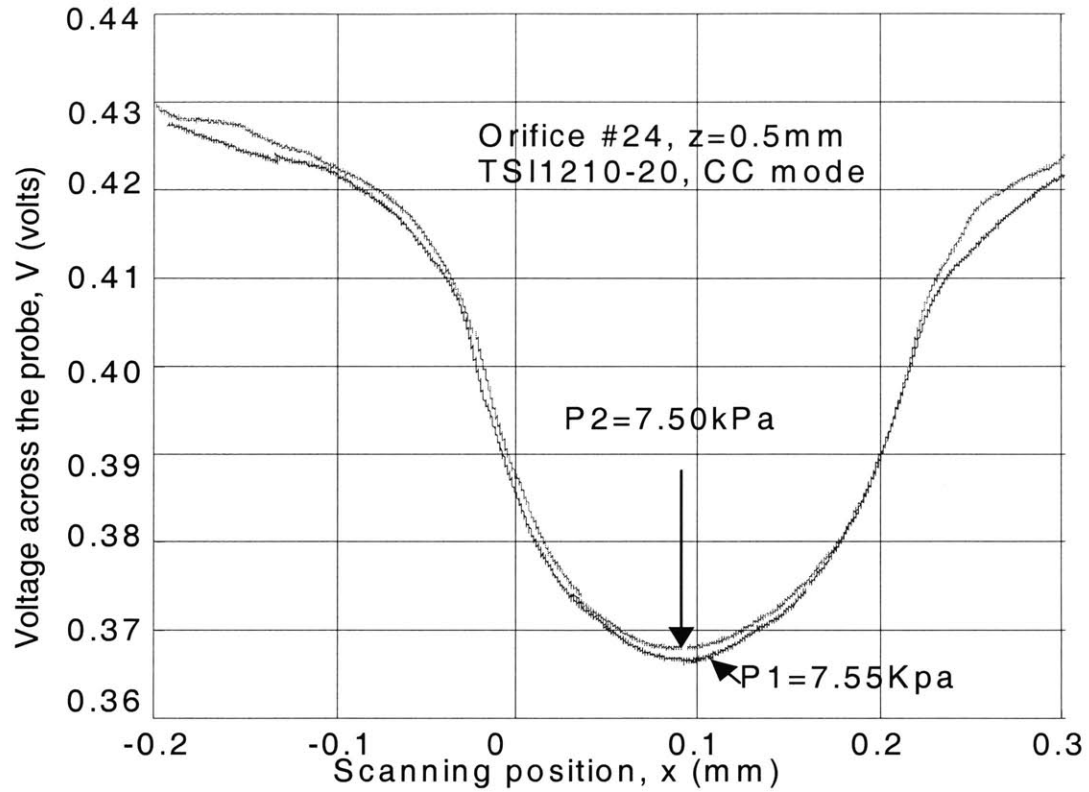


Figure 5-6. Hot-film scanning of orifice #24

#### 5.4 Reliability of hot-wire sensing for micro-jet flow

Figure 5-7 shows an optical image of a typical orifice, #35. From the image, small irregular defects can be observed in the left part of the orifice. Multiple scans of the jet show identical profiles (Figure 5-8). The scanning profiles overlap perfectly in the smooth parts (i.e.,  $x=800\sim 1200\mu\text{m}$ ). In the left side of the jet, i.e.,  $x=500\sim 800\mu\text{m}$ , the profiles are slightly not identical and include irregular features, indicating the impact of orifice defects on the jet flow. The results show that hot-wire sensing is reliable.



Figure 5-7. Optical image of orifice #35

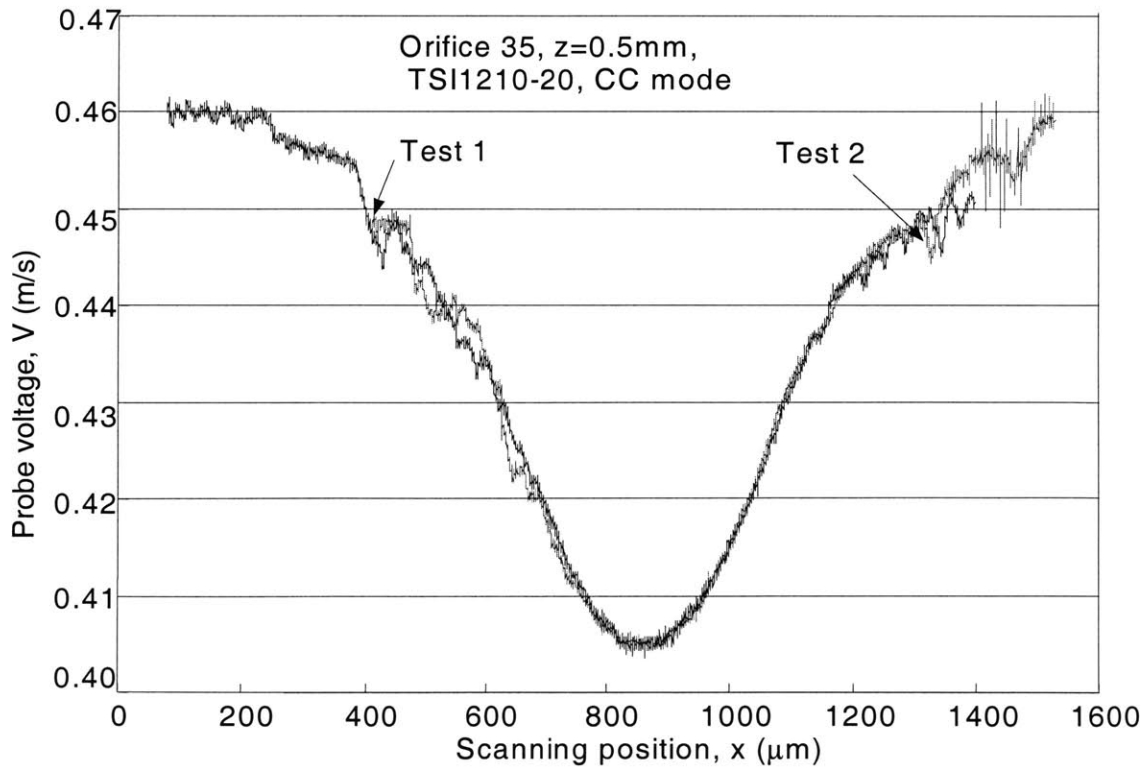


Figure 5-8. Repeatability of hot-wire scanning



## 5.5 Jet direction

When the sensing probe is scanned perpendicular to the jet, the ideal scanning profiles should be symmetric. The asymmetric profiles indicate that the orifice is non-circular and contains defects. Furthermore, the direction of jet flow can be deduced by tracing the center point of the symmetric scanning profiles at different axial positions.

Assuming that the jet center points are O1 ( $x_1, z_1$ ) and O2 ( $x_2, z_2$ ), the angle between the jet and the z axis,  $\theta$ , is

$$\theta = \tan^{-1}\left(\frac{x_2 - x_1}{z_2 - z_1}\right) \quad (5.2)$$

Figure 5-9 presents scanning profiles for a typical orifice under the constant-temperature mode. The axial position of the probe is 1 mm, 1.5mm and 2mm, respectively, and the backpressure is about 1kPa. At a relatively high jet velocity, the scanning profiles become asymmetric (figure5-10), and the jet center cannot be determined accurately. Similar results for hot-film probe working in the constant-current mode are found (figure 5-11).

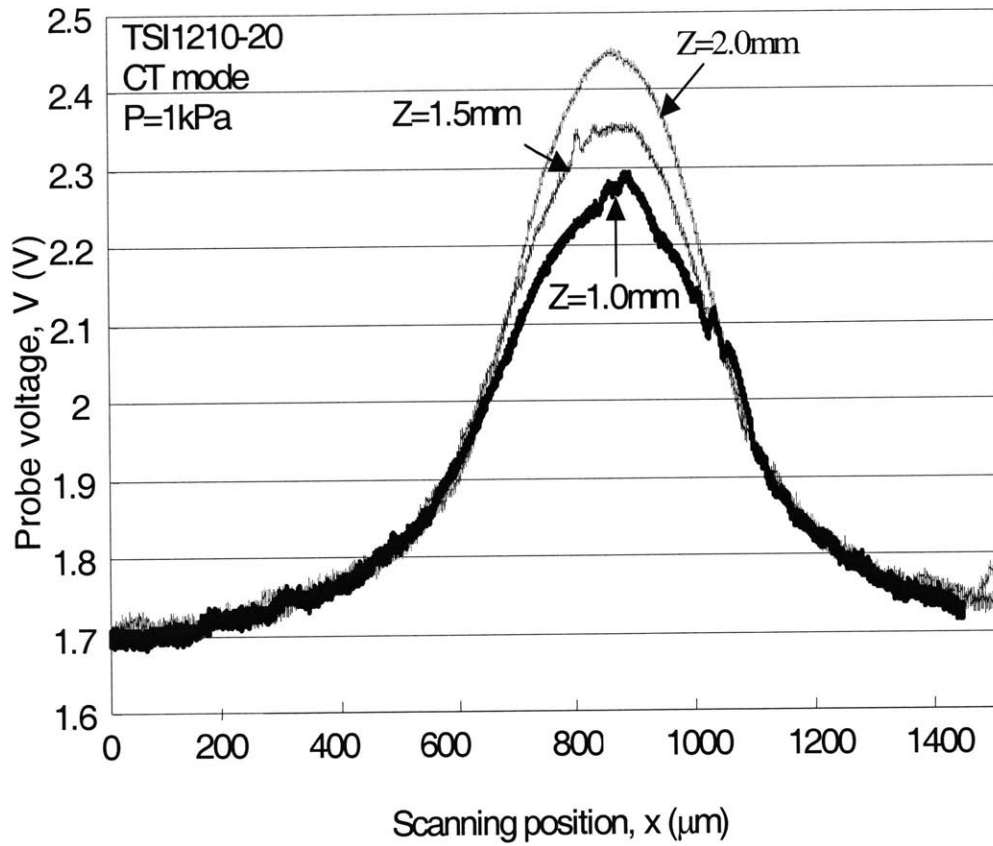


Figure 5-9. Hot-film profiling of jet at relatively low velocity

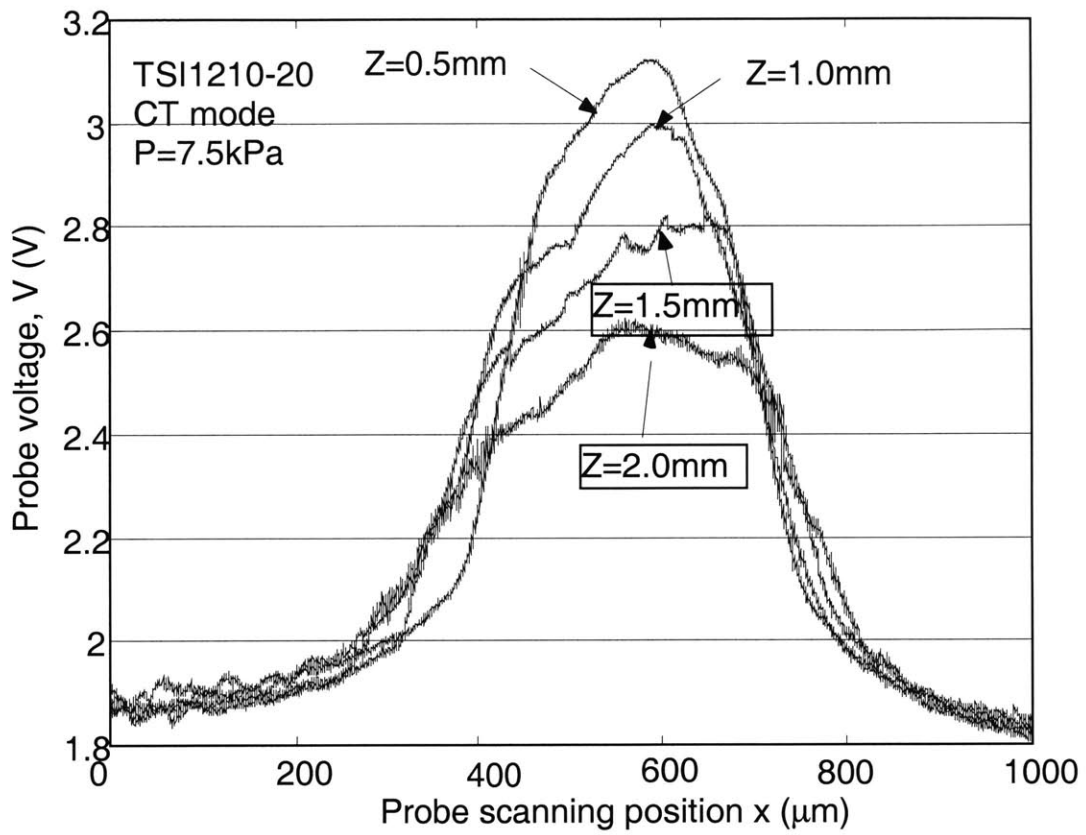


Figure 5-10. Hot-film profiling of jet at relatively high velocity

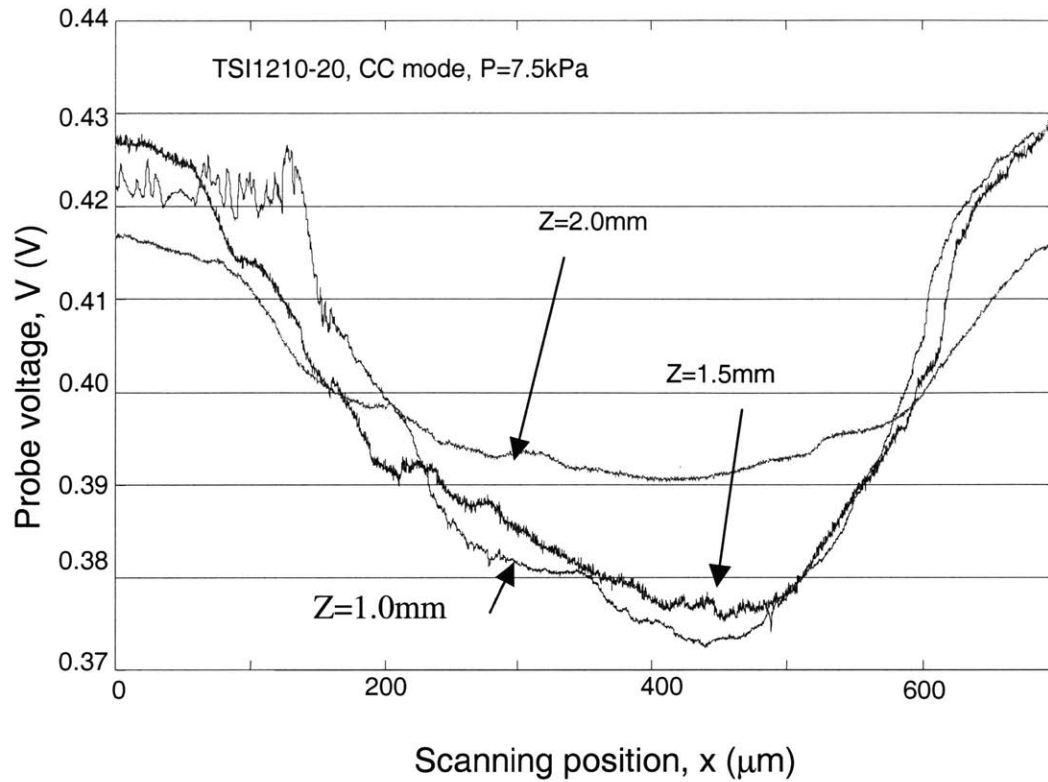


Figure 5-11. Hot-film profiling of jet at relatively high velocity (CC mode)

### 5.6 Sensing profiles at different backpressures

This section investigates the effect of backpressure on hot-wire scanning profiles. Figure 5-12 shows the pressure variation during typical hot-wire scanning. The three inlet pressures used in testing are  $P_1=0.70\text{kPa}$ ,  $P_2=2.05\text{kPa}$  and  $P_3=7.30\text{kPa}$ . The pressures are stable. Only four orifices were open in this experiment, and the rest were blocked.

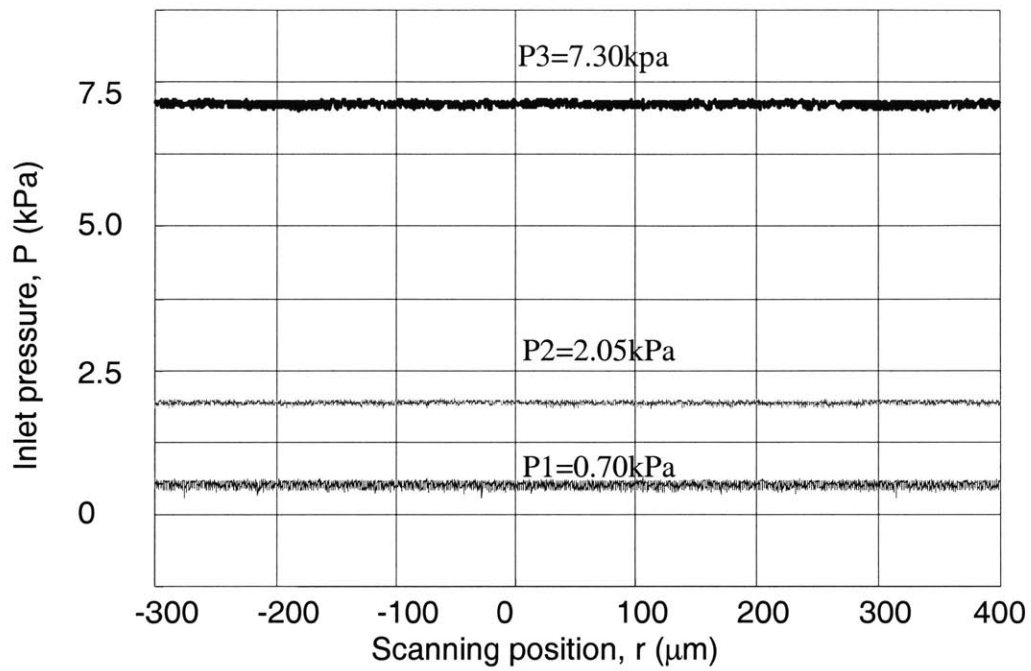


Figure 5-12. Three working backpressures when four orifices open

Figures 5-13 to 5-16 show the scanning profiles of jets #22-25 using a TSI 1210-20 probe under constant-current mode.

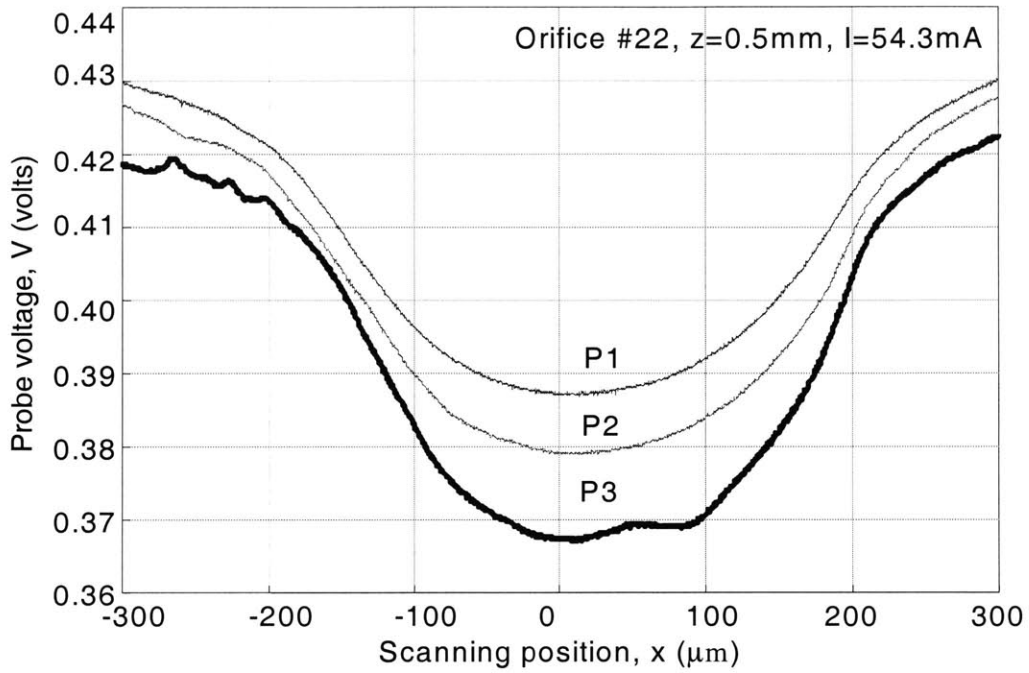


Figure 5-13. Scanning profiles of jet #22 (CC mode)

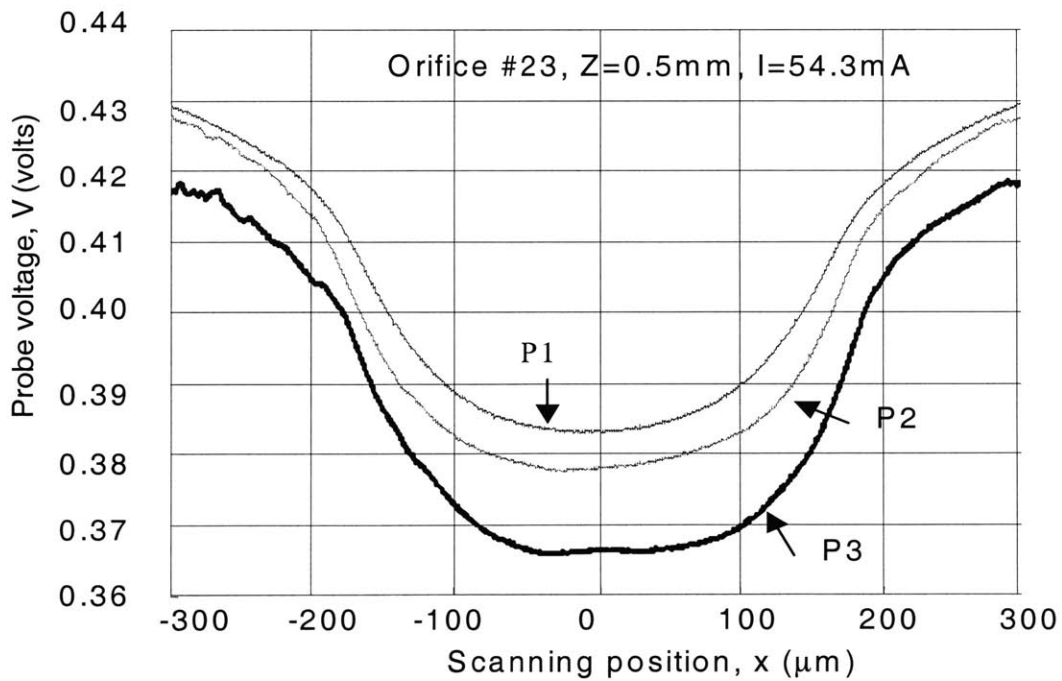


Figure 5-14. Scanning profiles of jet #23 (CC mode)

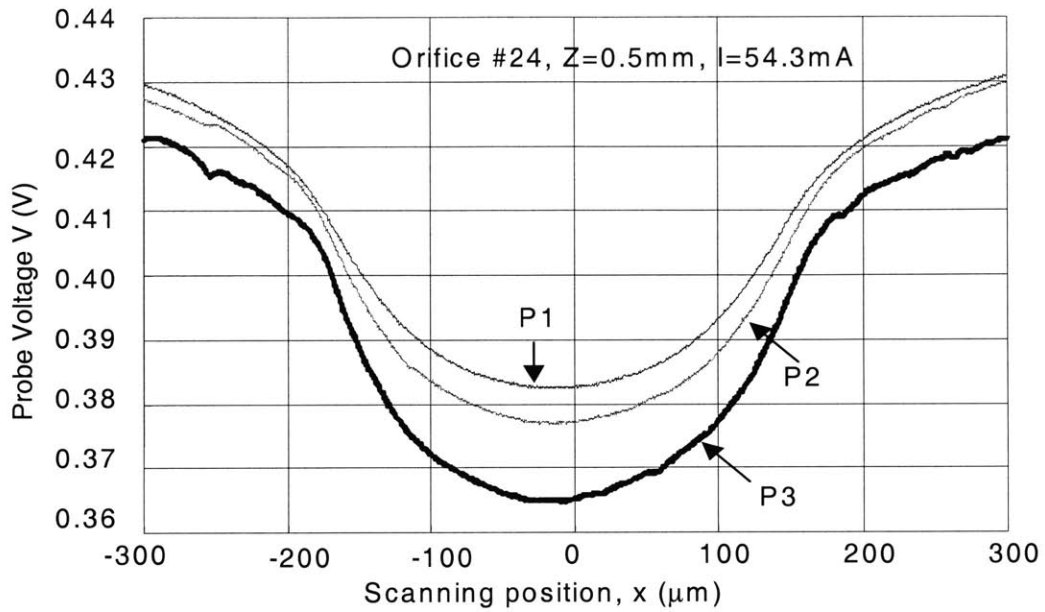


Figure 5-15. Scanning profiles of jet #24 (CC mode)

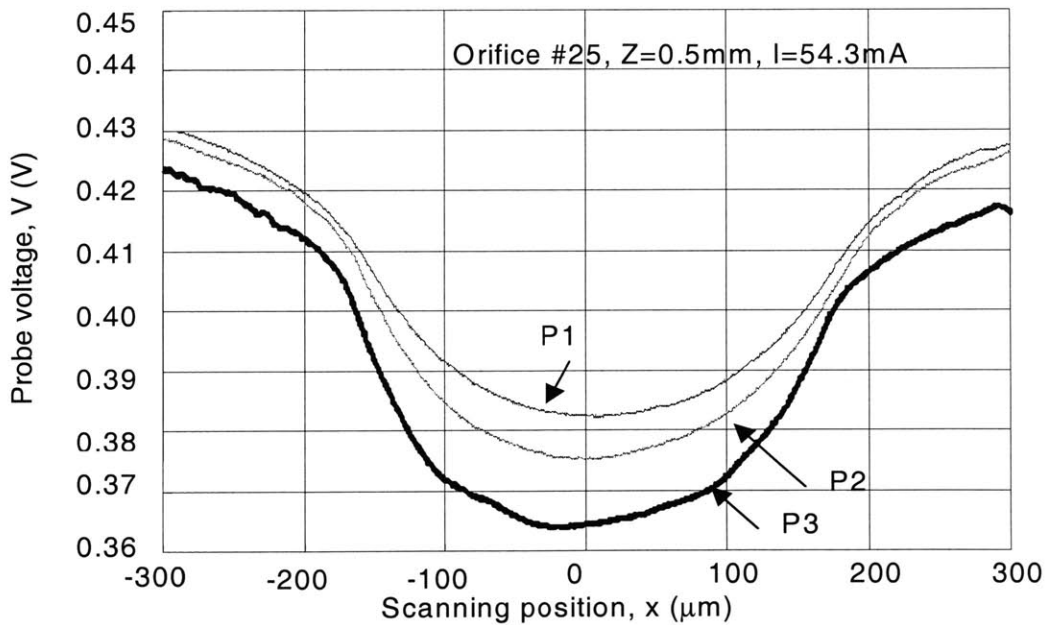


Figure 5-16. Scanning profiles of jet #25 (CC mode)

The scanning profiles are symmetric and smooth. When the inlet pressure increases, CC mode curves are symmetric and smooth. When the pressure as well as jet exit velocity increases, the average wire temperature decreases. Since the scanning plane is only 2.5-orifice diameter away from the orifices, the probe is within the potential core of the jets. In this region, the jet velocity increases with the backpressure. The jet width, however, is not strongly affected by the pressure.

Figures 5-17 to 5-20 show scanning profiles under the constant-temperature mode. The results are similar to those under the constant-current mode.

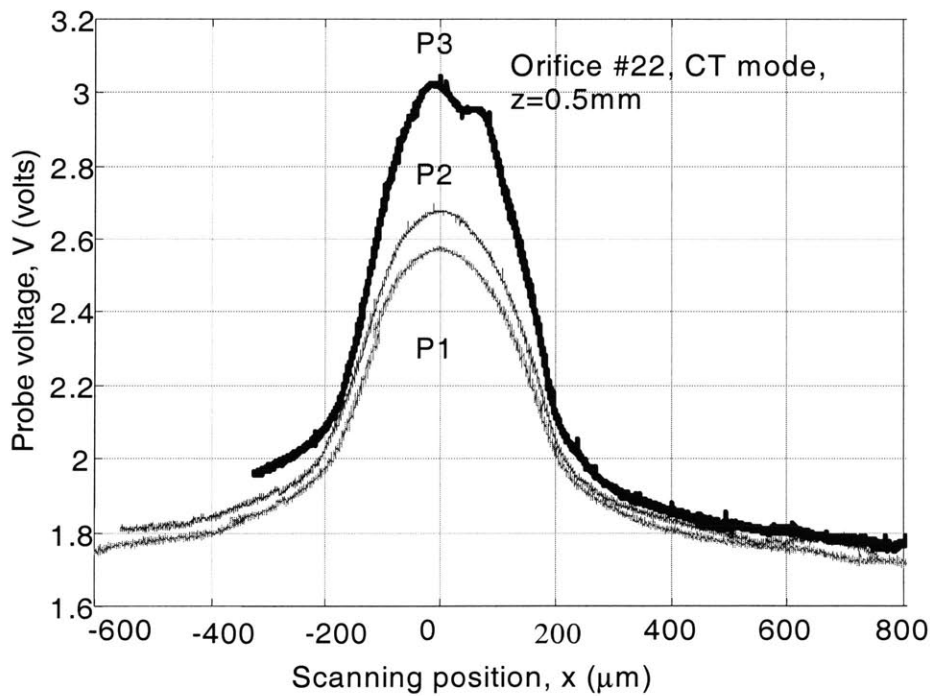


Figure 5-17. Scanning profiles of jet #22 (CT mode)



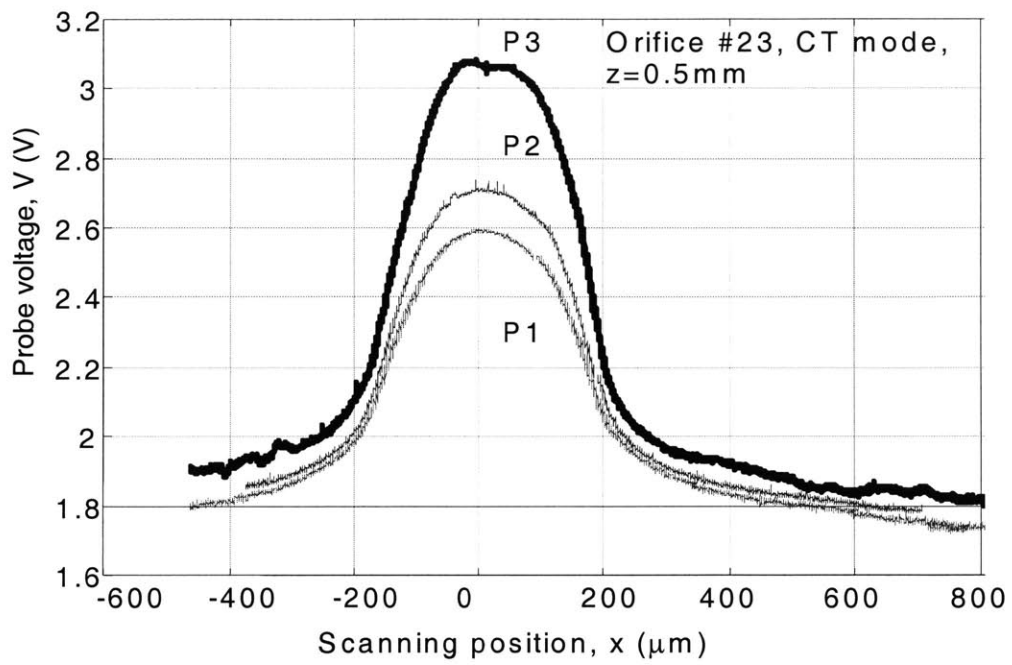


Figure 5-18. Scanning profiles of jet #23 (CT mode)

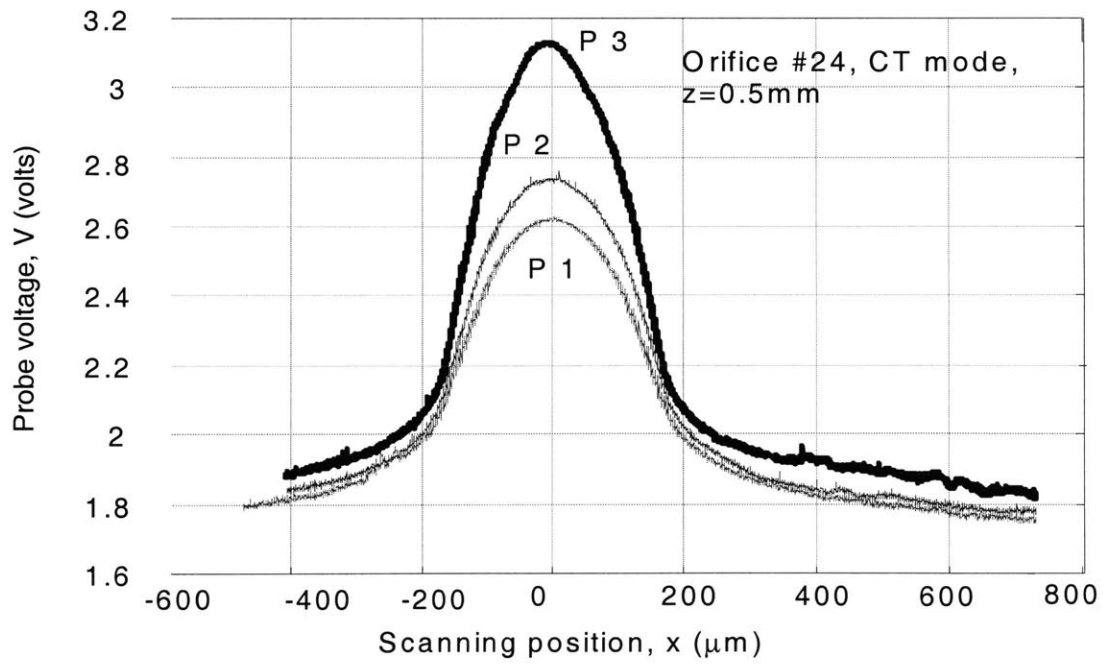


Figure 5-19. Scanning profiles of jet #24 (CT mode)

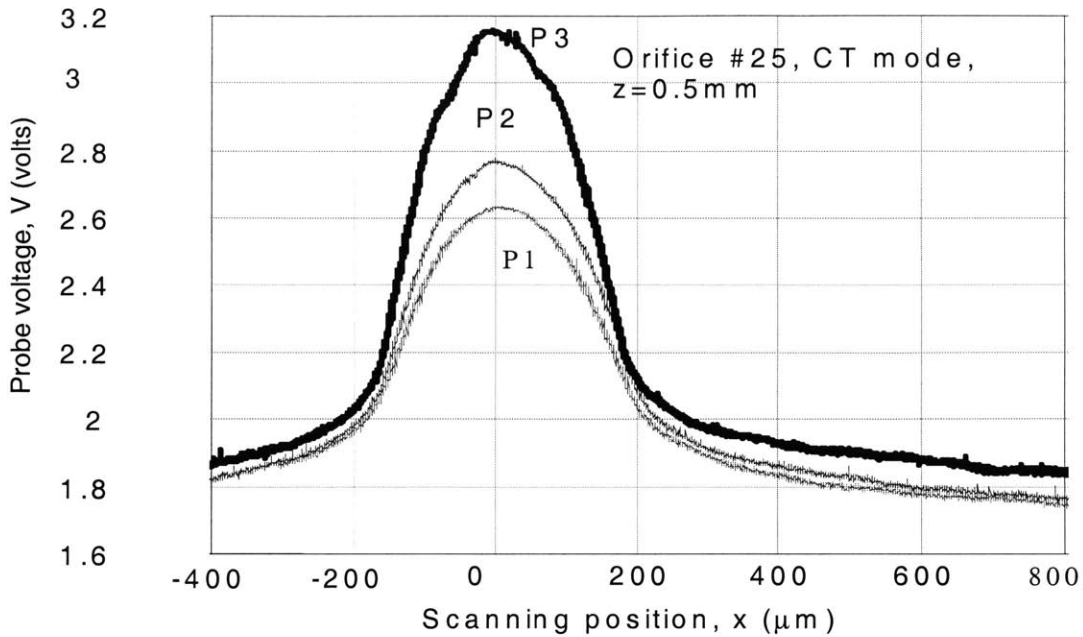


Figure 5-20. Scanning profiles of jet #25 (CT mode)

### 5.7 Uniformity of micro-jets

Figure 5-21 presents hot-wire scanning profiles when only four orifices, #22 - #25, are open. The sensing probe, TSI1210-20, was operated under constant-current mode. The axial position of the probe is 0.46mm, and the inlet pressure is 7.3kPa. The spacing between jets #22, #23, #24 and #25 are found to be 5.1mm, 4.7mm and 4.5mm, respectively. Jet #25 has the highest velocity.

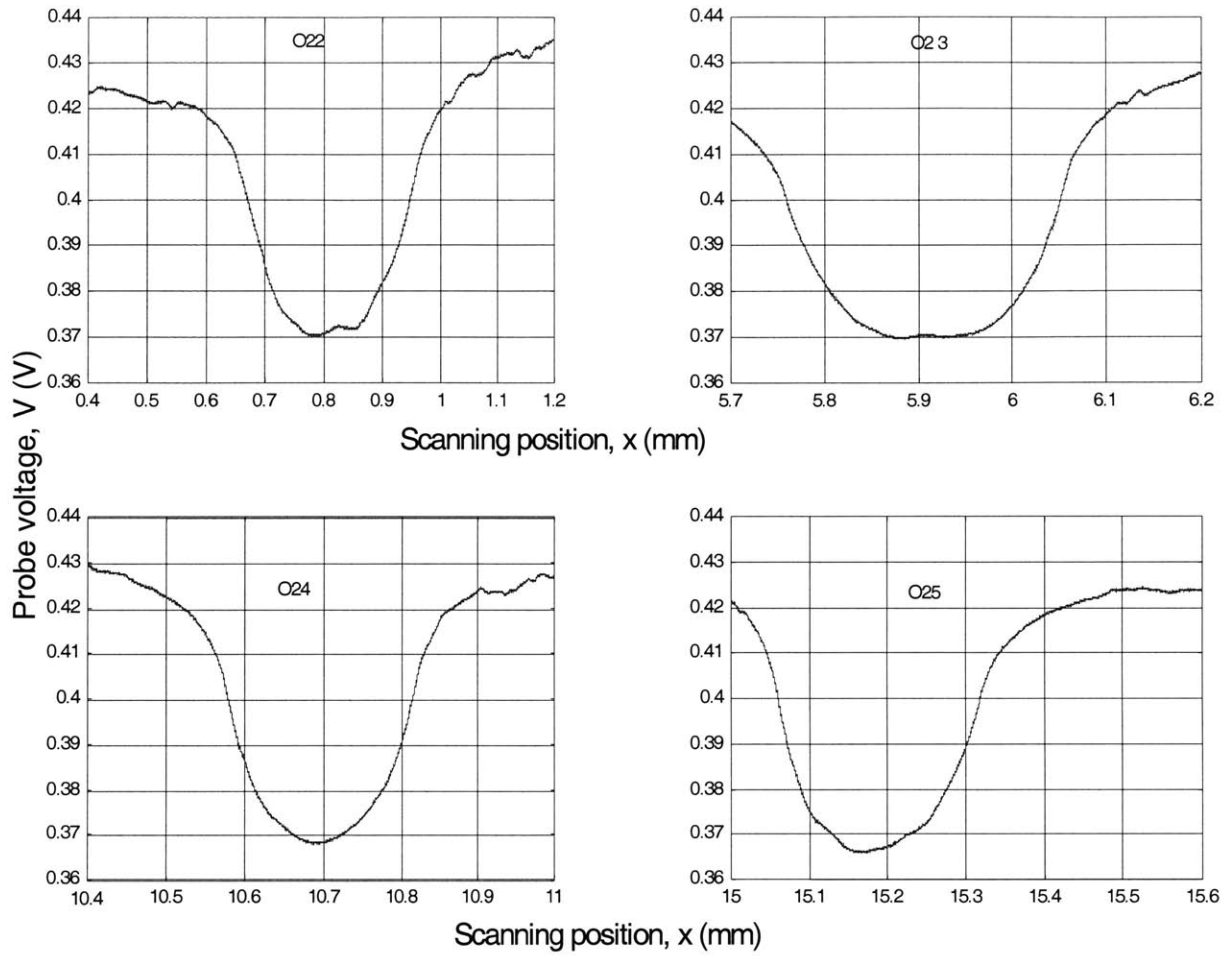
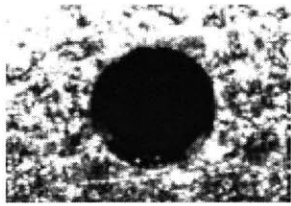
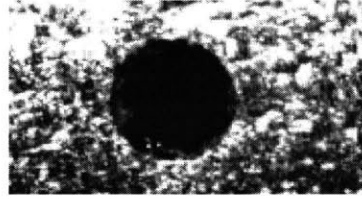


Figure 5-21. Scanning profiles of four orifices

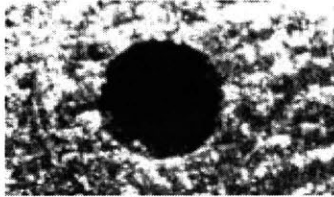
Figure 5-22 shows optical images of the solid debris can be seen on the inner edges of orifices #23 and #25. Orifice #25 is also not circular.



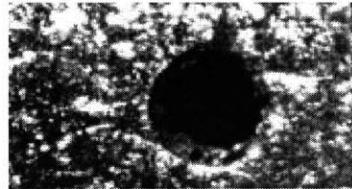
Orifice#22



Orifice#23



Orifice#24



Orifice#25

Figure 5-22. Optical images for four neighboring orifices

Figures 5-23 to 5-30 compare the sensing profiles of the four jets under different operation modes, and at different exit velocities. The axial position of the probe is 0.5mm. The results show that the jet velocity increases consistently from jet #22 to jet #25. Scanning profiles are smooth and symmetric at inlet pressures less than 2kPa. At the inlet pressure of 7kPa, irregular features are present near the center of the scanning profiles. The constant-current mode provides better velocity resolution than the constant-temperature mode.

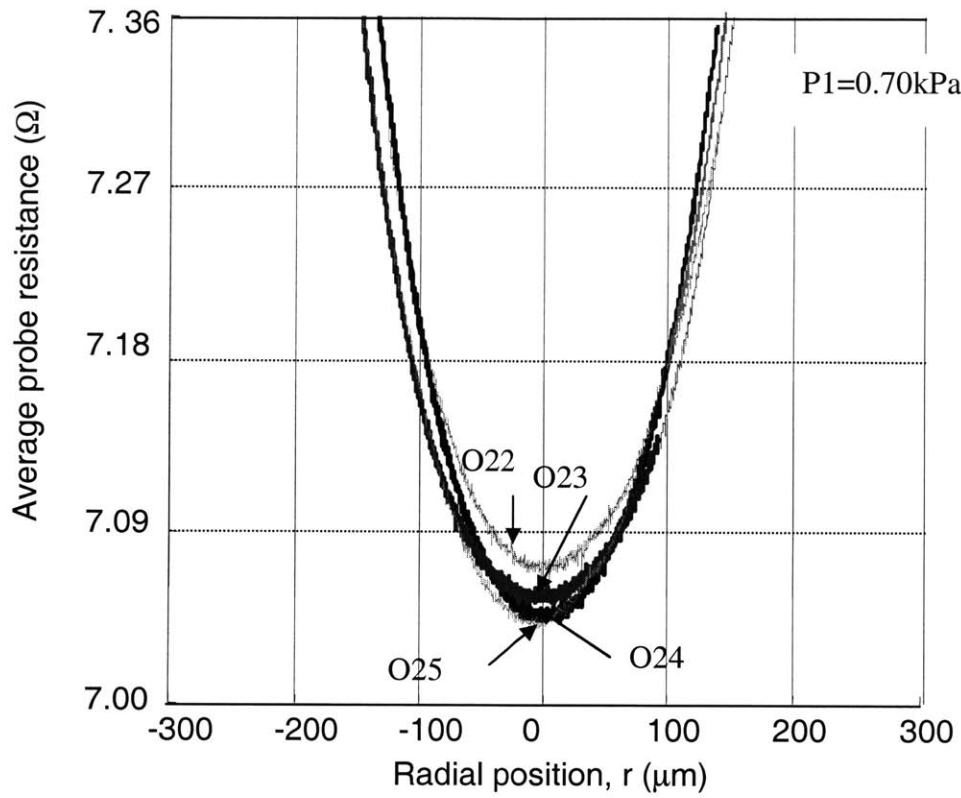


Figure 5-23. Scanning profiles at low backpressure (CC mode)

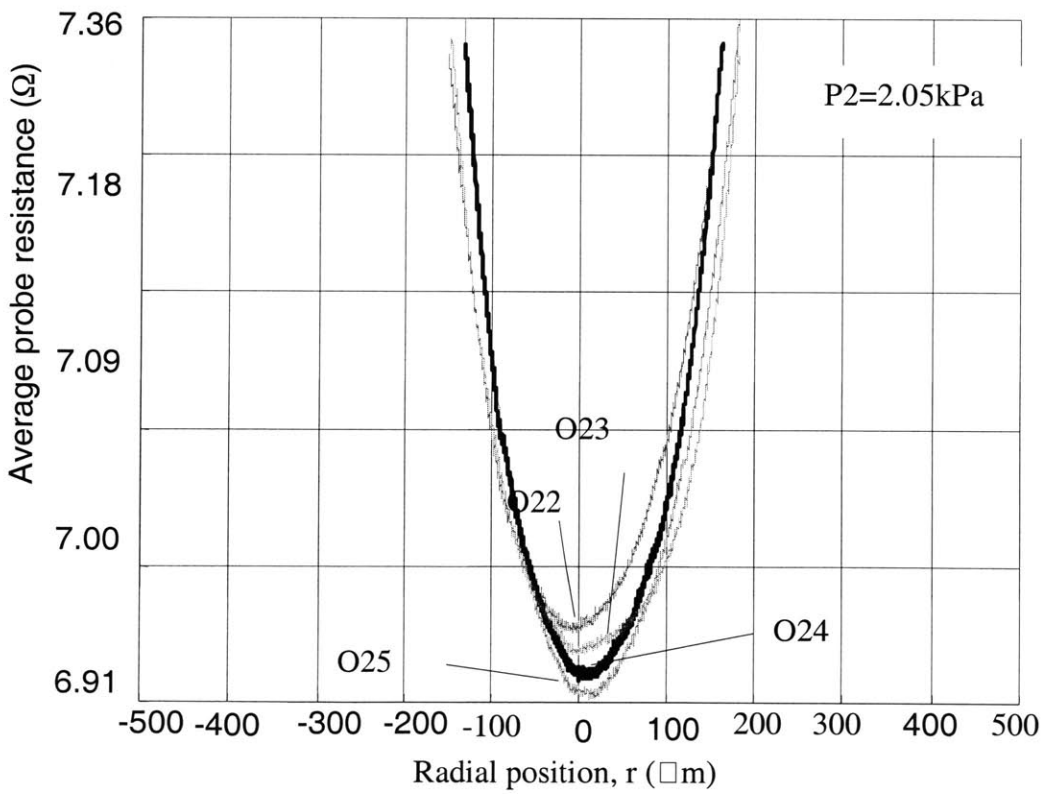


Figure 5-24. Scanning profiles at medium backpressure (CC mode)

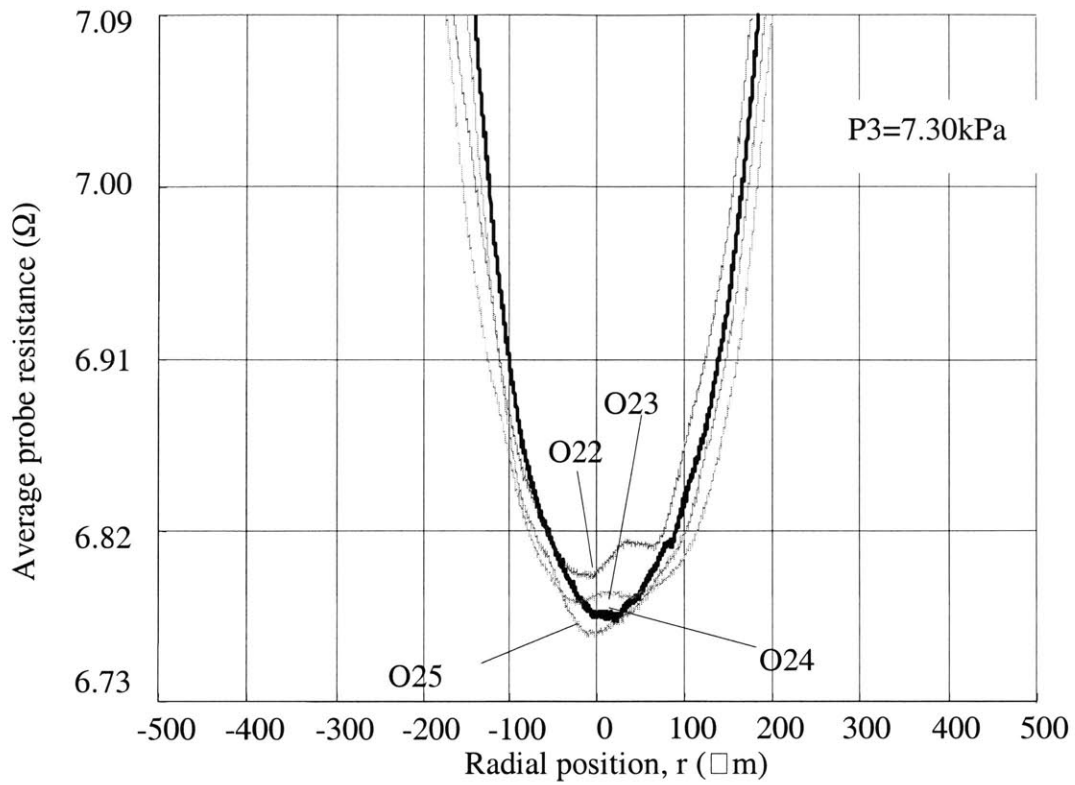


Figure 5-25. Scanning profiles at high backpressure (CC mode)

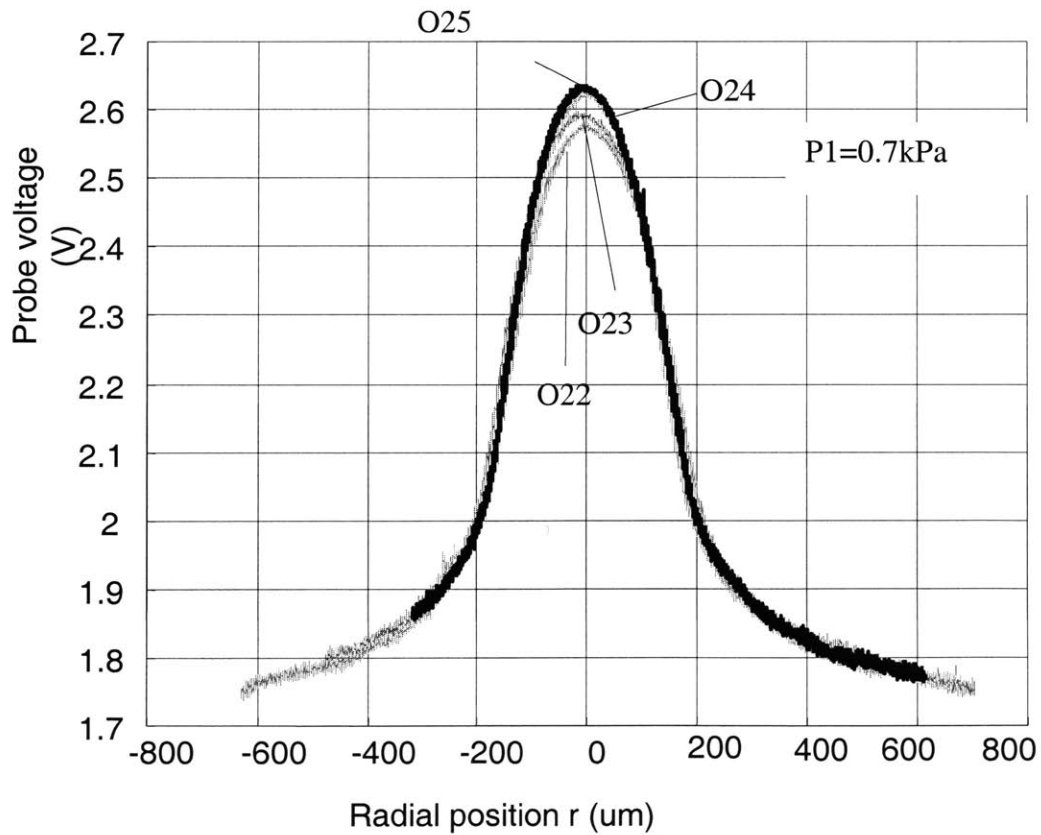


Figure 5-26. Scanning profiles at low backpressure (CT mode)

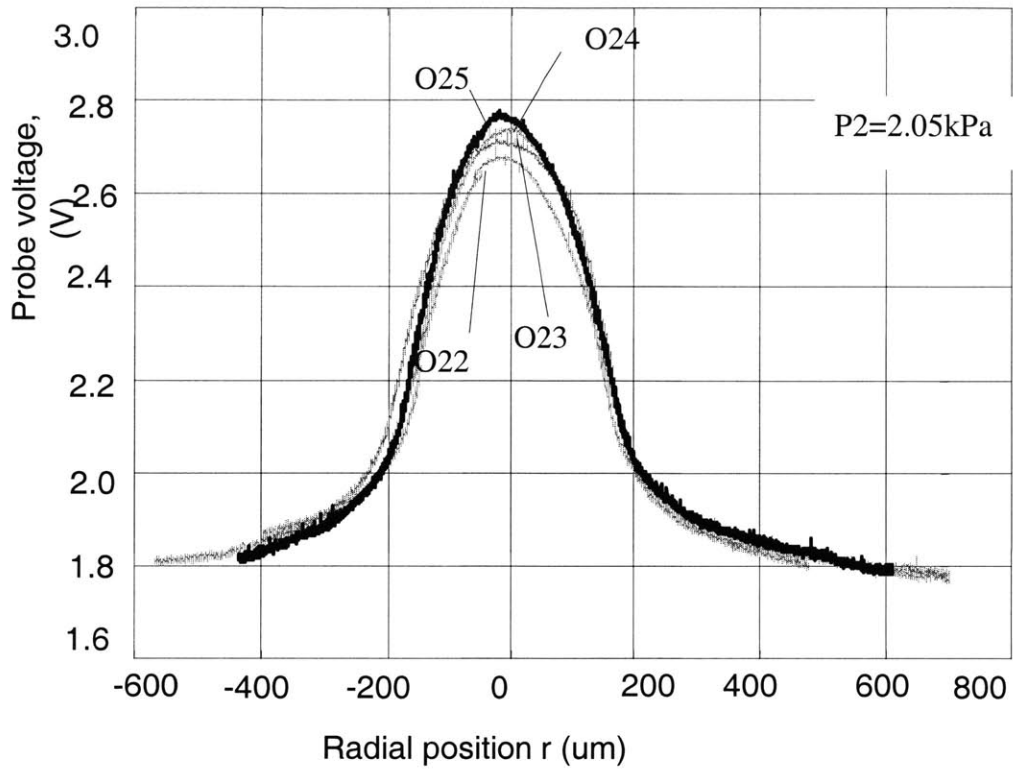


Figure 5-27. Scanning profiles at medium backpressure (CT mode)

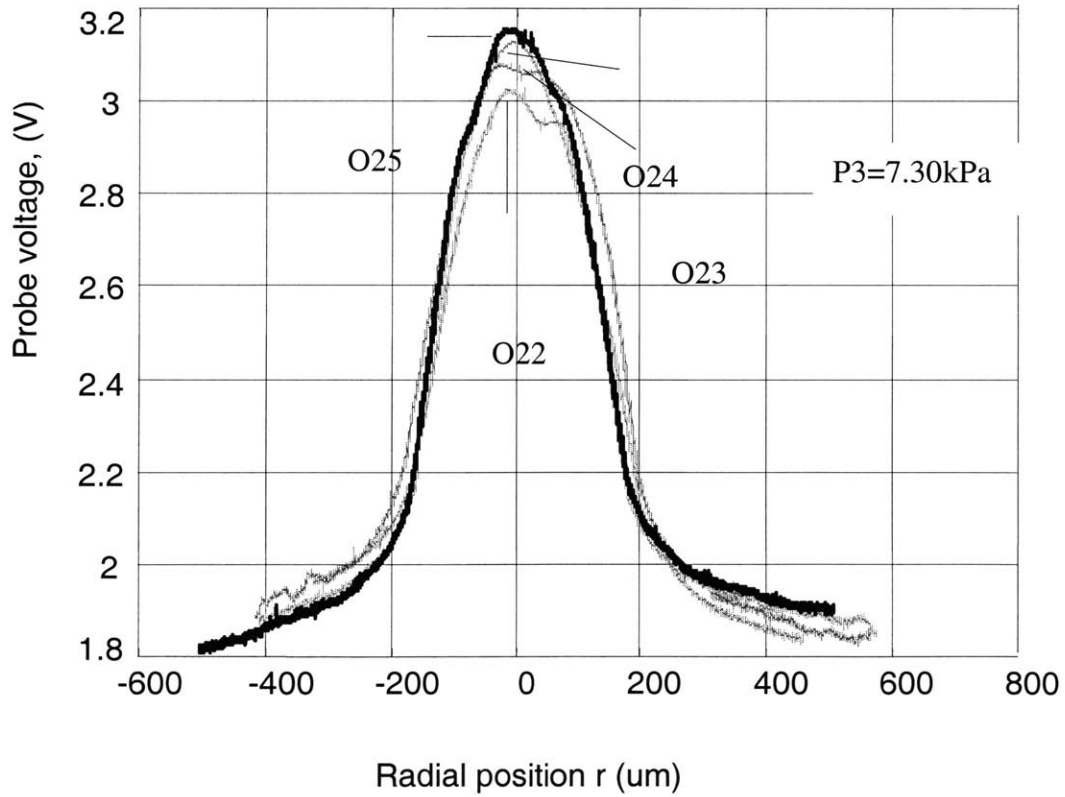


Figure 5-28. Scanning profiles at high backpressure (CT mode)

Figures 5-29 to 5-32 present scanning profiles of jets #22 to #25 when all the 49 orifices in the center region were open. The TSI1210-20 probe was operated under the constant-current mode and at an axial position of 1mm. The results show a continuous increase of the jet velocity for jets #22 and #24. The jet velocity drops slightly for jet #25 compared to jet #24.

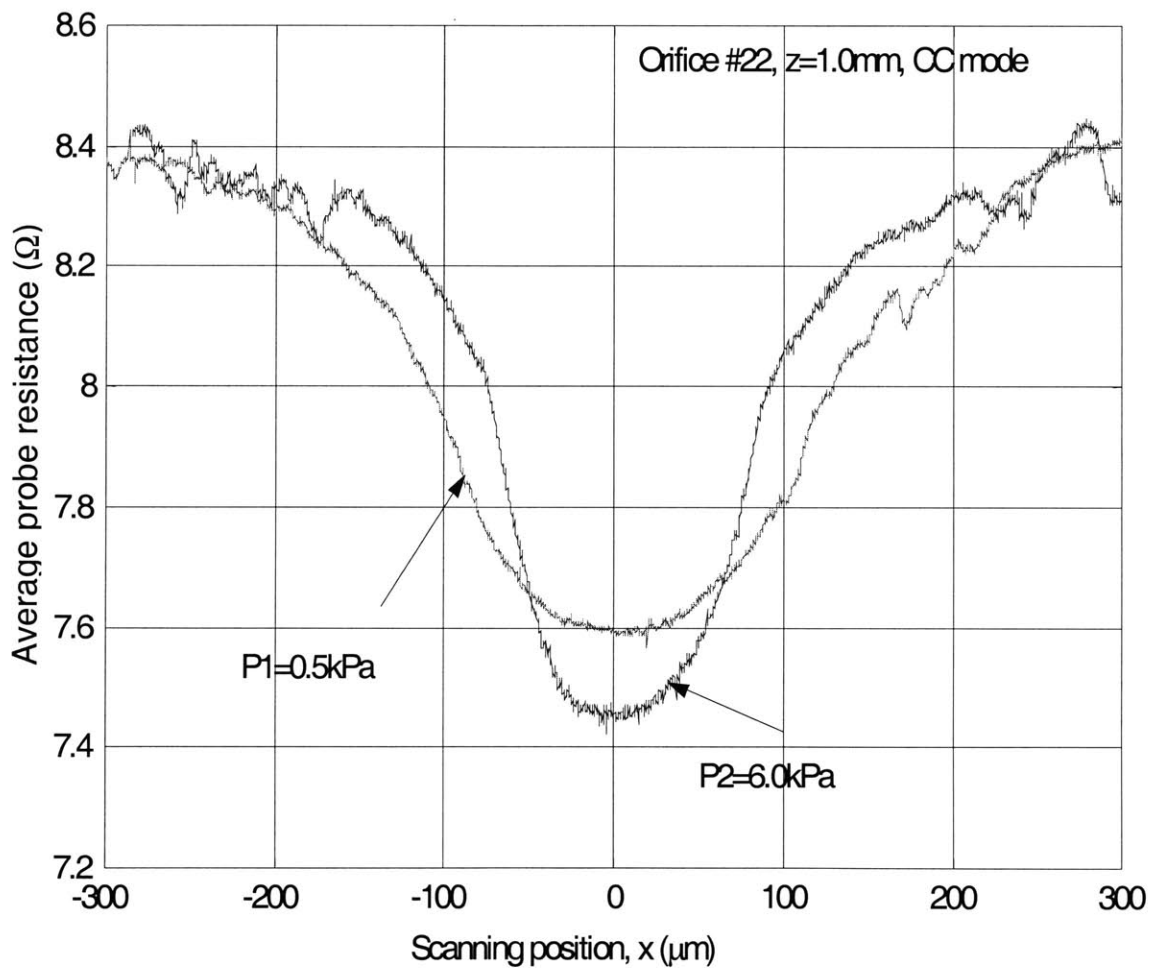


Figure 5-29. Scanning profiles of jet #22



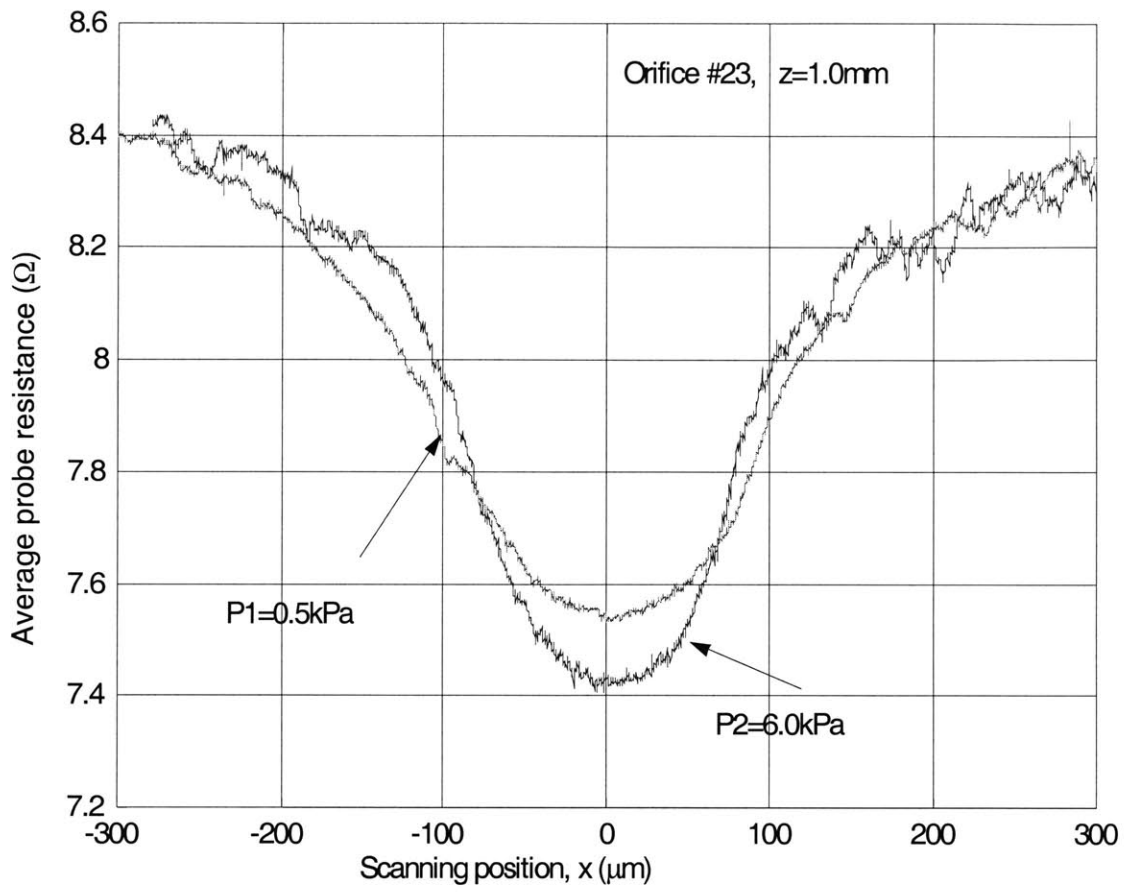


Figure 5-30. Scanning profiles of jet #23

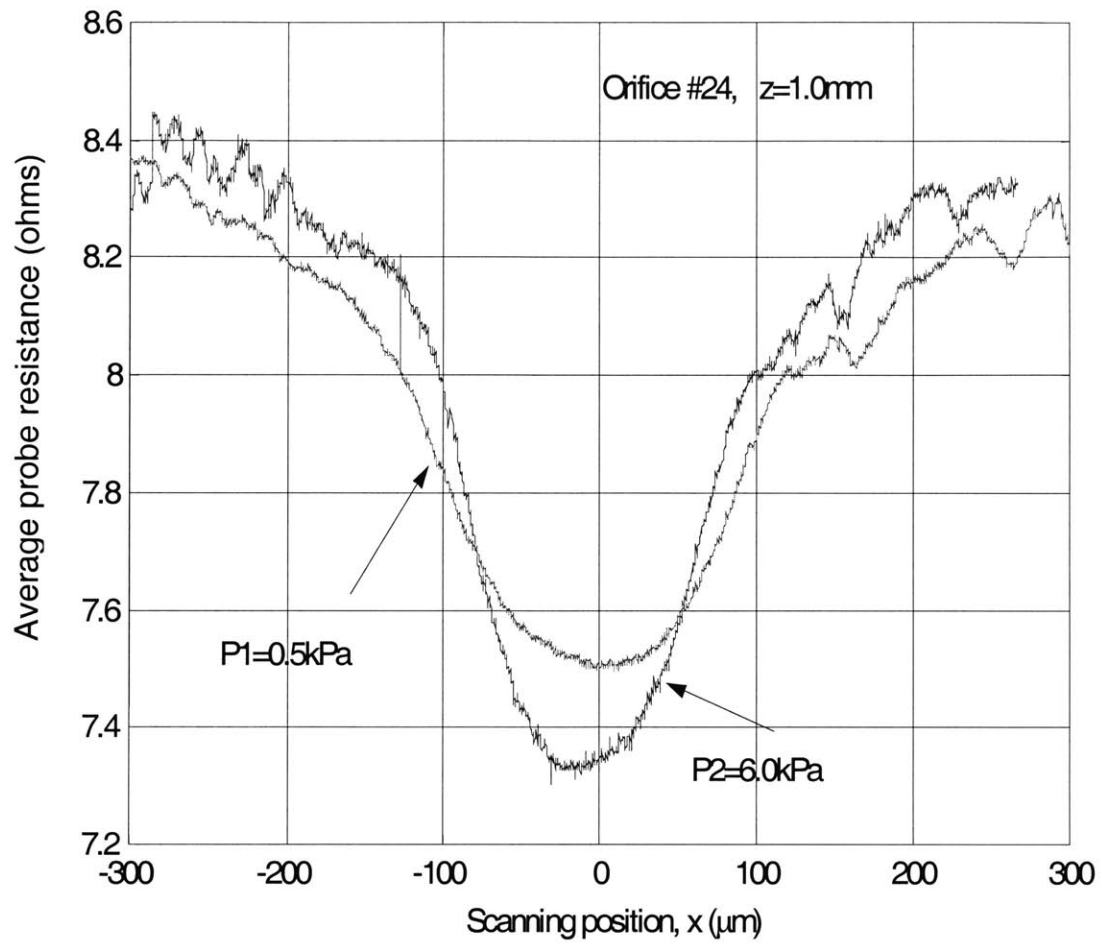


Figure 5-31. Scanning profiles of jet #24

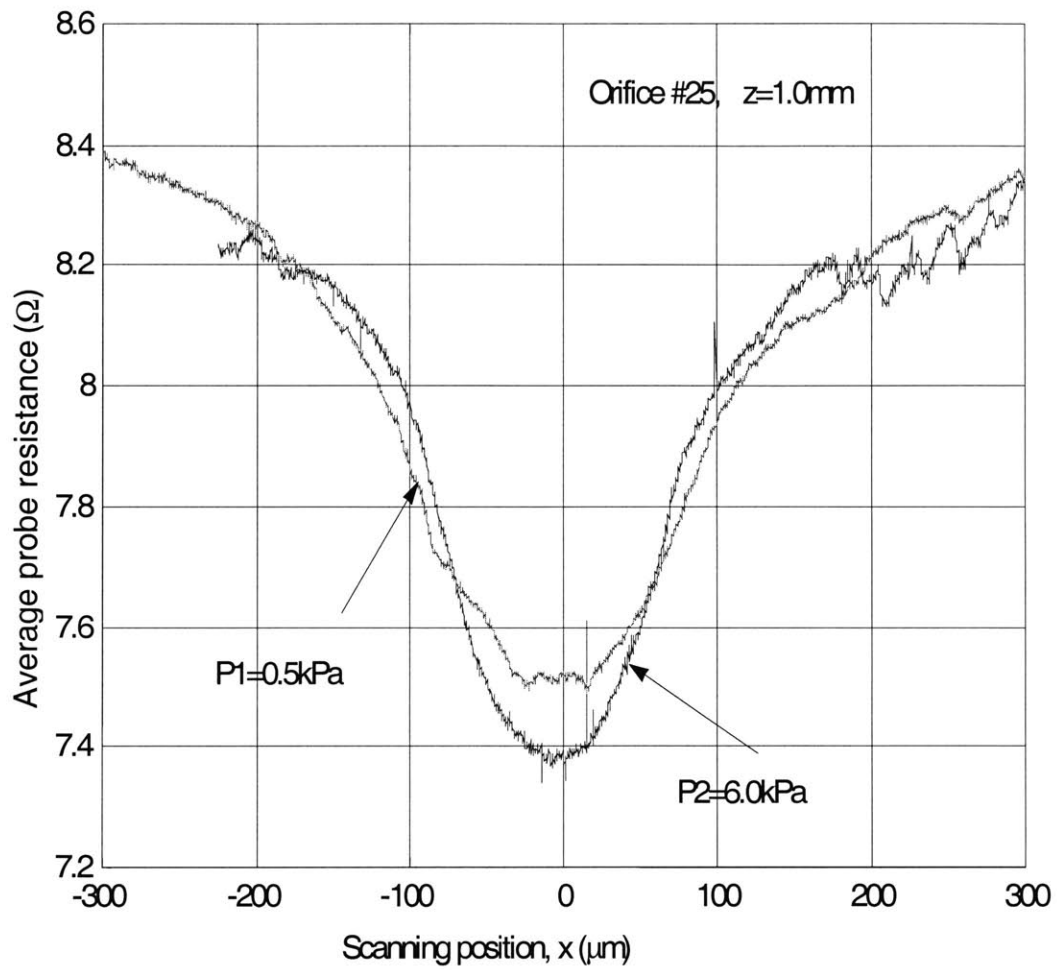


Figure 5-32. Scanning profiles of jet #25

Figure5-33 shows scanning profiles of every eight orifices along the metering tube. The center positions of the jets are arbitrarily shifted to make the results more distinguishable. The jet velocity has a relatively uniform distribution in the center region. At both ends of the tube, jet velocity is highly non-uniform (figure5-34 and figure 5-35). Optical images show significant defects at the inner surface of orifice #3 (figure5-36). The axial position of the TSI1210-20 probe is  $0.5\text{mm} \pm 0.1\text{mm}$  along the entire tube. As this sensing position, the scanning profiles are not sensitive to a small change of the axial position. The inlet pressure is 1.0kPa.

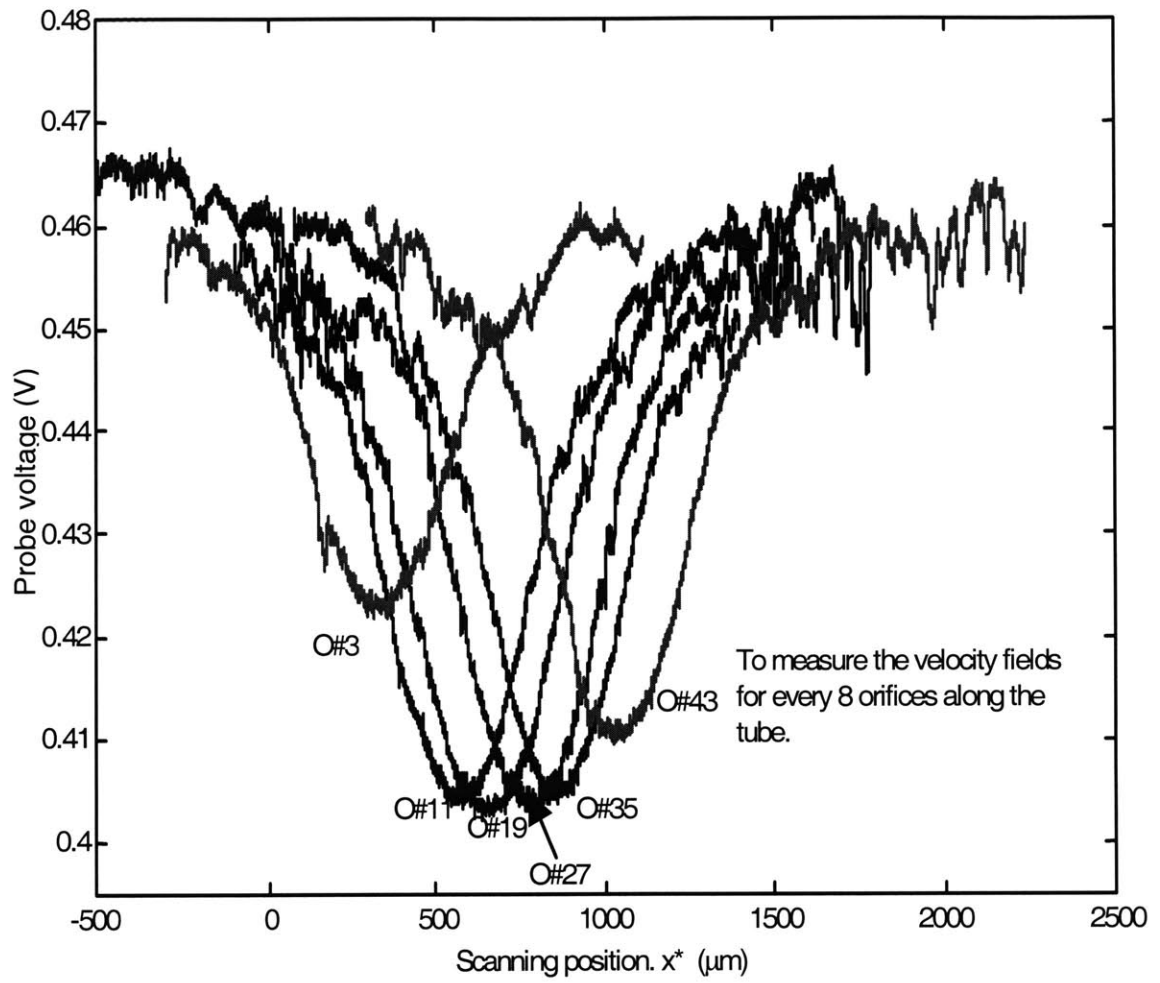


Figure5-33. Scanning profiles along the metering tube

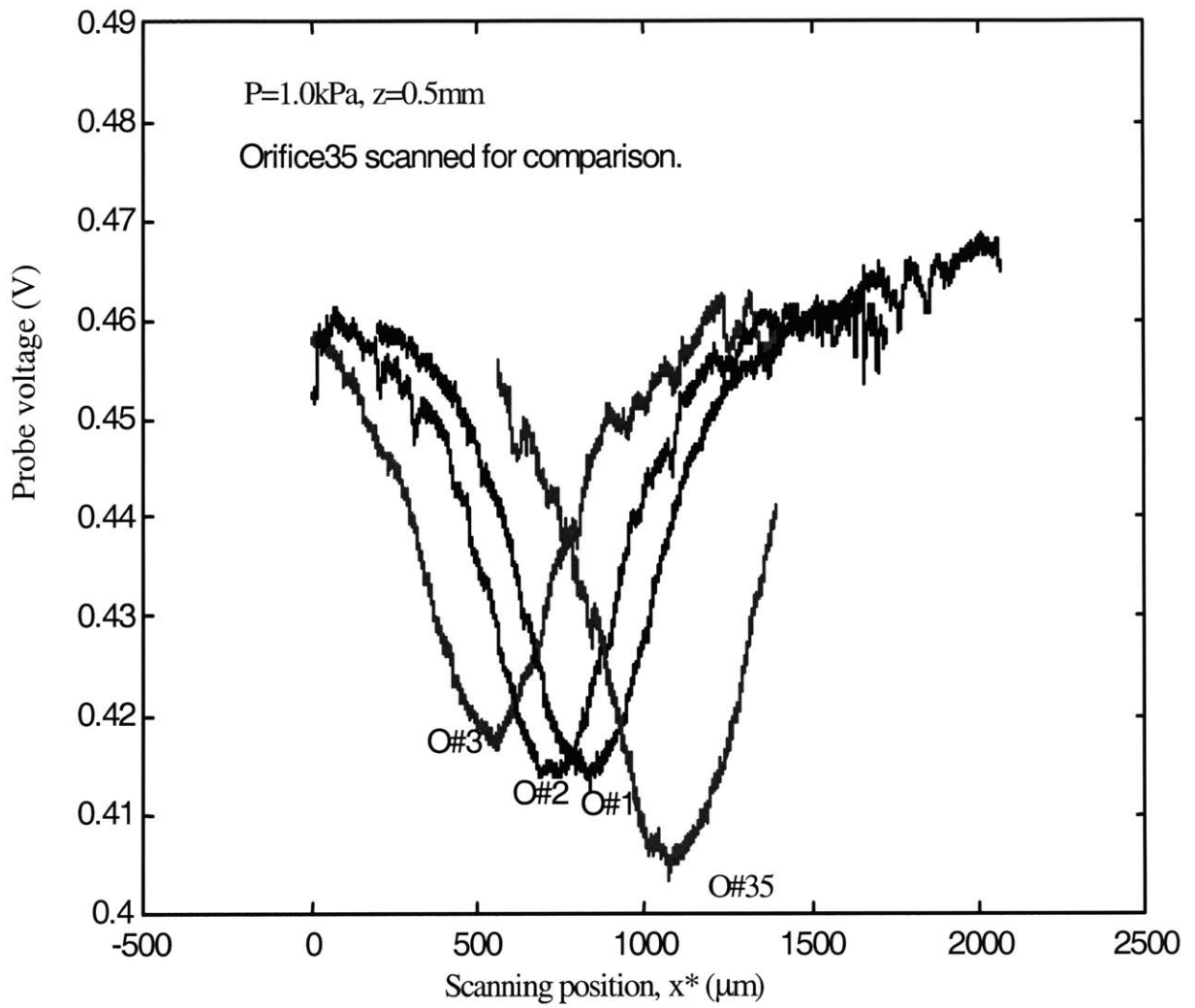


Figure5-34. Scanning profiles of jets near metering tube inlet

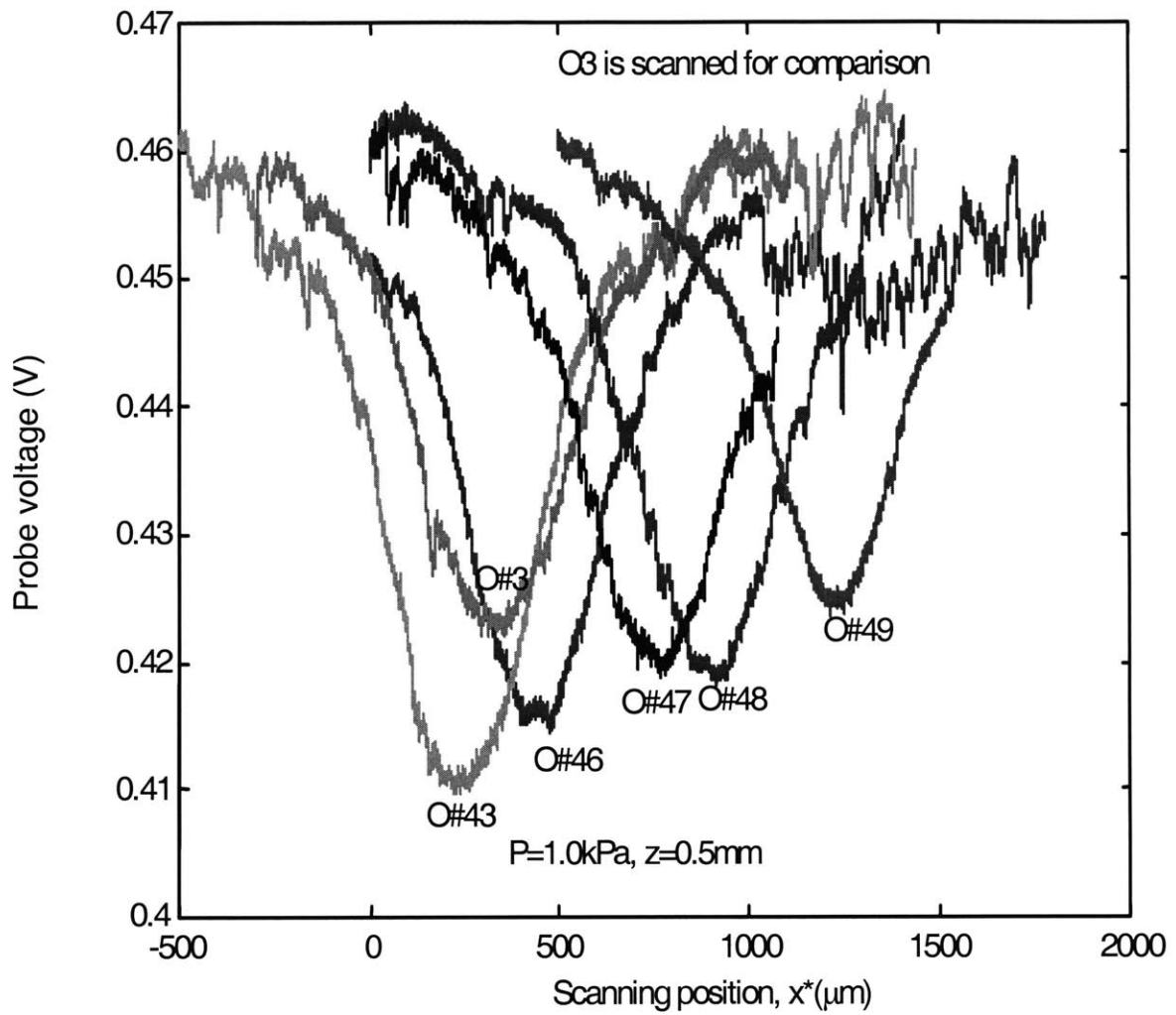


Figure5-35. Scanning profiles of jets near the dead end of metering tube

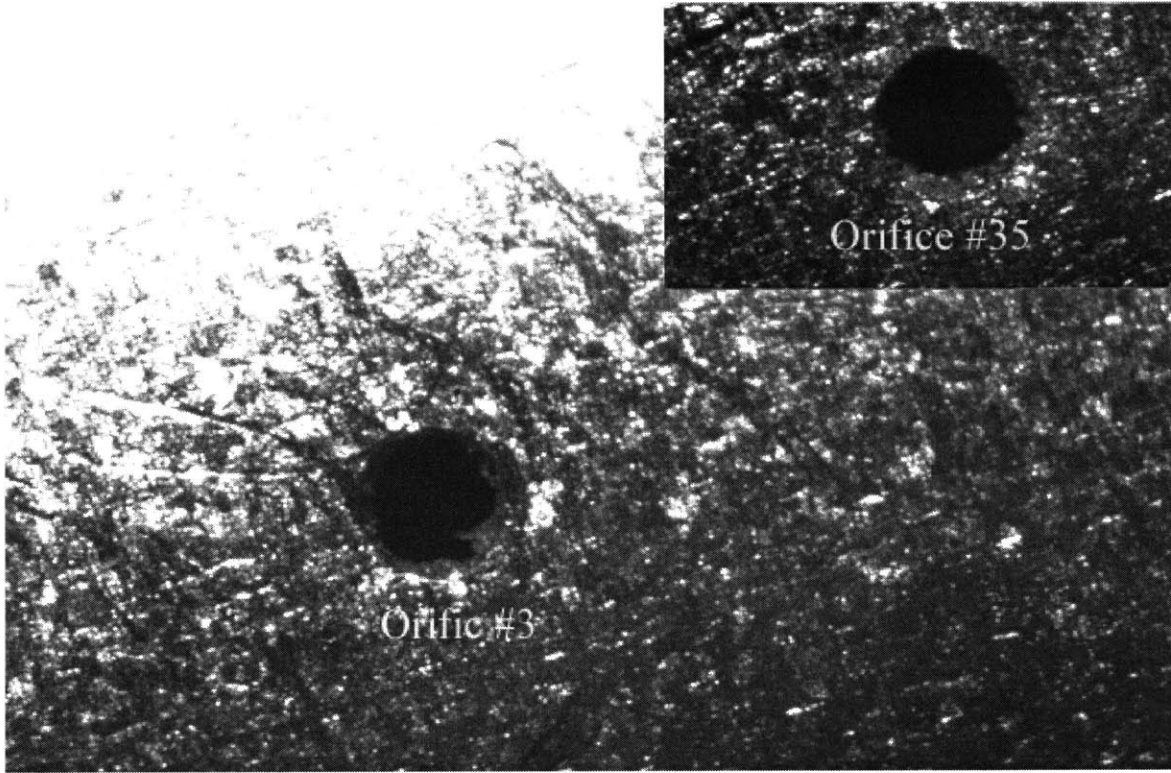


Figure5-36. Optical images of orifice #3 and #35



## Chapter 6 CONCLUSION AND FURTHER WORK

This work investigated applications of hot-wire probes for flow characterization of micro-jets, both theoretically and experimentally. A general heat transfer model was developed to describe the probe response to highly non-uniform jet flows. The experimental study established general features of hot-wire scanning of micro-jets.

First, the sensitivity of hot-film probes are similar to hot-wire probes. Since hot-film probes are more reliable and easier to align, they are recommended. Second, both the constant-temperature and constant-current models can be used to detect jet direction and velocity. The constant-current mode provides a slightly better resolution for resolving jet velocity, while the constant-temperature mode provides a slightly better delectability of the jet center. Third, within five-orifice diameters, the scanning profiles of a jet are not sensitive to the axial position of the probe. The profiles are smooth and symmetric at relatively low backpressures, e.g., 2kPa. At relatively high pressures, e.g., 7kPa, irregular features develop in the profiles. Fourth, the output signal from a hot-wire probe becomes increasing noisy as it moves away form an orifice. Fifth, large jet-to-jet velocity variations are found to be caused by orifice defects. In conclusion, this work demonstrated that a combination of hot-wire scanning and optical imaging techniques can be sued for rapid identification of manufacturing defects and qualification of gas delivery system of CVD machines.

In further studies, two or more wires can be integrated into one probe together. And then the jet flow can be scanned by wires from different directions simultaneously. Moreover, different work modes (CC/CT) can be applied to different wires for best sensing results. It will greatly reduce the sensing time and collect more information about the jet velocity filed together.

In addition to wires integrations, a high-resolution imitating system can also be integrated along with the sensor and capture the orifice sidewall defects simultaneously. The relationship between the distortion of the sensing curve and the orifice shape defects can be studied in details in the future.

## REFECENCES

- Borgos, J.A, "A review of electrical testing of hot-wire and hot-film anemometers," *TSI Quart.*, VI, No.3, 3-9, 1980.
- Bruun, H.H., *Hot-wire Anemometry: Principles and Signal Analysis*, Oxford University press, Oxford, 1995.
- Dobkin D.M. Mokhtari S., Schmidt M., Anil P. and Robinson L., "Mechanisms of Deposition of SiO<sub>2</sub> from TEOS and related organosilicon compounds and Ozone," *J. Electrochem. Soc.*, Vol. 142, No. 7, 2332-2339, 1995
- Fingerson L.M. and Freymuch, P., "Thermal anemometers', in *Fluid Mechanics Measurements*," (ed. R.J. Goldstein), pp. 99-154, Hemisphere, Washington, 1983.
- Freymuch P. and Fingerson L.M., "Electronic testing of frequency response for thermal anemometers", *TSI Quart.*, 3, No.4,5-12, 1977a.
- Freymuch, P. "A comparative study of the signal-to-noise for hot0film and hot-wire anemometers," *J. Phys. E.: Sci. Instru.*, 10, 705-710, 1978
- Freymuth, P. "Frequency response and electronic testing for constant temperature hot-wire anemometers," *J. Phys. E.Sci. Instruments*, 10, 705-710, 1977b.
- Incropera F.P. and DeWitt D.P., *Fundamentals of Heat and Mass Transfer*, fourth edition, John Wiley & Sons, Inc., 1996
- Lomas, C.G., *Fundamentals of Hot Wire Anemometry*, Cambridge University Press, Cambridge, 1986
- Mayer B., "Small signal analysis of source vapor control requirements for APCVD," *IEEE Transactions on semiconductor manufacturing*, Vol. 9, No.3, 344-365, 1996

- Mokhtari S., Kudriavtsev V.V., and Danna M., "Flow uniformity and pressure variation in multi-outlet flow distribution pipes," *ASME, PVP.Vol. 355, Advances in Analytical, Experimental and Computational Technologies in Fluids, Structures, Transients and Natural Hazards*, 103-122, 1997
- Oh H.J., Rhee S.W, Kang I.S., "Simulation of CVD Process by Boundary Integral Technique," *J. Electrochem. Soc.*, Vol. 139, No. 6, 1714-1720, 1992
- Perry, A.E., and Morrison, G.L., "A study of the constant-temperature hot-wire anemometer," *J. Fluid Mech.*, 47, 577-599, 1971
- Perry, A.E., *Hot-wire Anemometry*, Clarendon Press, Oxford, 1982
- Schlichting, H., *Boundary-Layer Theory*, McGRAW-HILL BOOK COMPANY, 1979
- Turns. S.R., *An Introduction to Combustion: Concepts and Application*, second edition, McGRAW-HILL, INC., 2000
- White, F.M., *Fluid mechanics*, third edition, McGRAW-HILL, INC., 1994.